UNIVERSIDAD DE ALCALÁ

ESCUELA POLITÉCNICA SUPERIOR

DEPARTAMENTO DE ELECTRÓNICA

TESIS DOCTORAL
Electrónica: Sistemas Electrónicos Avanzados. Sistemas Inteligentes

"Novel photonic systems and devices exploiting the Raman effect in optical fiber"

Autor
Javier Nuño del Campo
Ingeniero de telecomunicación, Universidad de Valladolid

Directores
Juan Diego Ania Castañón
Doctor en Física

Sonia Martín López
Doctor en Física

2013

Abstract

The Raman effect is an important nonlinear effect with applications mainly in the fields of spectroscopy and fiber optics. Since the end of the twentieth century and thanks to the output power improvement and price reduction of pump lasers, its application to optical amplification in optical fiber communications has become widespread. In this thesis, two particular types of Raman amplifiers are studied: ultralong Raman fiber lasers (URFLs) and Raman polarizers.

The advantages of distributed amplification based on URFLs have been demonstrated over the last decade in several optical communications systems, in which the efficient distribution of the gain over long distances offered by these amplifiers allows for a nearly optimal balance between noise and nonlinear effects, which leads to improved performance. Nevertheless, one of the main sources of errors in this type of amplifiers is the RIN transfer between the pumps and the signal.

The first chapter of results in this thesis is committed to study this impairment, focusing on the numerical analysis of a specific case of URFLs, the random distributed feedback fiber lasers (RDFLs) in which the feedback is distributedly provided by Rayleigh scattering, instead of relying on a classical cavity delimited by reflectors. A second batch of results explores three applications of URFL amplification (to distributed sensing based on

Brillouin optical time-domain reflectometry, to gyroscopic measurements using Sagnac interferometers and to long haul, high-speed, coherent communications) from a theoretical and, in the case of long-haul communications, experimental perspective. In all cases we demonstrate that the use of URFL-based amplification can lead to performance improvements.

Raman polarizers are an special kind of Raman amplifiers which not only amplify but also produce a polarized output thanks to the polarization dependence of Raman gain. In this thesis, the first complete and general analysis of the evolution of the state of polarization of a signal in Raman amplification system, in the presence of other nonlinear effects, is presented. As a result a system of differential equations which can be solved numerically in order to describe the main characteristics of Raman polarizers is presented. This system is valid for all cases of interest and requires less computational time than previous approaches. An analytical approximation applicable to most situations of interest is also presented. Finally, a method for the suppression of RIN in Raman polarizers based upon the fast scrambling of the input signals is presented.

Resumen

El efecto Raman es un importante efecto no lineal con aplicaciones principalmente en el campo de la espectroscopía y de la fibra óptica. Desde finales del siglo XX y gracias al abaratamiento y la mejora de las fuentes de bombeo, se ha extendido su uso para la amplificación de señales en comunicaciones ópticas. En esta tesis se estudian dos tipos particulares de amplificadores Raman: los láseres ultralargos (URFLs) y los polarizadores Raman.

A lo largo de la última década se ha demostrado en diversos sistemas de comunicación que la eficiente distribución de ganancia en largas distancias ofrecida por los URFLs permite, en diversas aplicaciones, lograr un equilibrio casi óptimo entre el ruido y los efectos no lineales, lo cual repercute en mejoras en el rendimiento del sistema. No obstante, una de las principales fuentes de error en este tipo de amplificadores es la transferencia de ruido de intensidad relativa (RIN) entre las fuentes de bombeo y la señal.

El primer capítulo de resultados incide en la problemática del RIN, centrándose en su análisis numérico para un caso específico de URFL, los láseres aleatorios de fibra, cuya particularidad radica en carecer de cavidad delimitada, dependiendo en su lugar del *scattering* Rayleigh para proveer al sistema de retroalimentación distribuida. A continuación se estudian tres aplicaciones de los URFLs (al análisis óptico de dominio temporal basado en efecto Brillouin para la determinación distribuida de temperatura y tensión,

a la mejora de los interferómetros de Sagnac para medidas giroscópicas y a las comunicaciones a larga distancia con modulación de fase) de forma tanto numérica como, en el caso de las comunicaciones coherentes, experimental, en las que el uso de este tipo de amplificación permite una mejora del rendimiento.

Los polarizadores Raman son un tipo especial de amplificador Raman en el cual no sólo se amplifica la señal, sino que se la polariza haciendo uso de la dependencia de la ganancia Raman con el estado de polarización relativo. En esta tesis se presenta el primer análisis teórico general de la evolución del estado de la polarización de la señal en sistemas con amplificación Raman, incluyendo el resto de efectos no lineales. Este análisis concluye con la obtención de un sistema de ecuaciones diferenciales que puede resolverse de manera numérica para describir las principales características de los polarizadores Raman. Como ventaja, este sistema es válido en todas las situaciones de interés y requiere un tiempo de cálculo inferior a otros sistemas similares. Se expone también una aproximación analítica de aplicación a un gran número de casos. Finalmente, se presenta un método para la reducción de la inestabilidad de amplitud en este tipo de dispositivos basada en la depolarización rápida de las señales de entrada.

Agradecimientos

Hace 7 años me concedieron una beca Erasmus en Birmingham para desarrollar el PFC en temas de fotónica. Por aquel entonces, no tenía claro a qué quería dedicarme y ni siquiera tenía claro que me gustara la fotónica. En aquel momento, apareció el responsable de mi estancia, Juan Diego Ania, siempre disponible y optimista, dispuesto a ayudarnos en todo lo necesario tanto en el plano personal como en el plano ciéntifico. Años más tarde sería él, de nuevo, el que me ayudará a conseguir una beca de doctorado y se convirtierá en mi director de tesis. Para él va mi más sincero agradecimiento.

No puedo olvidarme, en segundo lugar, de Sonia Martín que aceptó ser codirectora de mi tesis aportando su granito de arena para que esta tesis saliera a tiempo.

Aparte de ellos, esta tesis ha sido posible gracias al trabajo de mucha gente. Me gustaría mencionar también a todas personas que me han ayudado cuando he estado de estancia. En Birmingham, agradezco a Paul Harper y a Pawel Rosa su comprensión cuando los instrumentos del laboratorio no funcionaban como debían. En Brescia, agradezco a Stephan Wabnitz y a Victor V. Kozlov por su paciencia al intentar aclararme todos los conceptos teóricos que debía. Es en Victor en el que me gustaría detenerme para hacer más sonora mi gratitud. Con él colaboré en varios artículos de esta tesis y gracias a él ha salido adelante el capítulo de polarizadores. Con tu

fallecimiento se ha perdido un gran ciéntifo.

Añado un fuerte agradecimiento a Pedro Corredera por colaborar con todo lo que le hemos pedido para el laboratorio e intentar que los trabajos experimentales pudieran ampliarse.

No quiero olvidarme de nadie del grupo de "Dinámica no lineal y fibras ópitcas", por lo que empiezo este párrafo haciendo partícipes de esta tesis a todos los miembros del grupo. En especial, le agradezco a Ranjeet todo lo que me ha enseñado estos años. No conseguimos que hablaras una palabra de castellano pero pocos guiris conocen mejor Madrid que tú. A mis otros compañeros de despacho: Mercedes y Juan Luis con los que pase largas y agradables horas. A Xabi, que me dejó "meter mano" en sus experimentos y a Francisco que intentó colaborar en los míos. Y finalmente, a José María Soto, siempre dispuesto a escuchar los resultados de esta tesis.

Hago extensible mi agradecimiento al resto de miembros del instituto de óptica y de estructura de la materia con los que compartí comidas en la cantina y alguna que otra caña por la tarde.

Asimismo deseo agradecer el estímulo, el apoyo y el sostén que me ha ofrecido durante todos estos años mi familia. A mis padres, que me han facilitado en todo lo posible que pueda alcanzar mis objetivos. A mi mujer Inés, que es la que ha sufrido los malos momentos de esta tesis. A mis abuelos y a mi hermana por ser modelos en los que inspirarme.

Por último, agradecer también a toda la gente de secretaría, tanto del CSIC como de la Universidad de Álcala por facilitarme los trámites burocráticos.

Esta tesis ha sido financiada por el programa FPI 2009 del MICINN con referencia BES-2009-019601 y asociada al proyecto TEC2008-05791. La colaboración con la Universidad de Brescia ha sido posible gracias a la acción integradra Italia-España HI2008-0075.

Contents

Chapter 1

Introduction

This thesis focuses on two different approaches to the exploitation of Raman scattering in optical fiber, represented by two particular families of nonlinear devices: ultra-long Raman lasers (URFLs) and Raman polarizers. In the case of URFLs, whether based on a traditional configuration (cavity-based) or a mirrorless one (known as a random distributed feedback fiber laser or RDFL), our study explores their main sources of impairment and their potential application to the fields of sensing and phase-keyed optical communications, including both theoretical and experimental results. Raman polarizers, on the other hand, are studied exclusively from a theoretical point of view, presenting for the first time a full mathematical model for their study, and using it to explore different potential applications.

1.1 Motivation

Over the past couple of decades, advances in telecommunications have changed the world. Nowadays, huge amounts of information can travel hundreds of kilometers in the blink of an eye, and new applications (tele-medicine, video on demand...) cause a demand for a constant increase in network capac-

ity. Regarding this matter, optical networks remain a key technology that shows important advantages [1] when compared to any other long-haul form of communication. The most important ones are its extremely high bandwidth and the lower signal deration that allow long-haul transmission without excessive bit errors. Moreover, the alternative for very long distances is satellite communication, in which the transmission is subject to time delays and can be seriously affected by adverse weather conditions. Optical fiber is basically unaffected by external conditions or electromagnetic interferences and it presents a low latence. Finally, communication over fibers are more secure as we can early detect any manipulation of the fiber cable.

However, among the challenges of using optical networks, there are issues such as the creation of ultra-long unrepeated transmission systems for intermediate distances of the order of a few hundreds of kms, or the development of all-fiber devices to avoid the bitrate cap and additional losses introduced by the use of electronic devices. Here, Raman scattering plays an important role and the new devices proposed and studied in this thesis can contribute to solve these problems.

The advantages of distributed Raman amplification versus other alternatives for optical amplification are also well known [2]. When compared to traditional lumped amplification with Erbium-doped fiber amplifiers (EDFAs), Raman amplification can provide a flatter gain over a broader bandwidth, while allowing for a selection of the desired spectral window of amplification by means of the choice of the pump wavelength. Furthermore, Raman scattering is an intrinsic effect of fiber optics and, consequently, it is not necessary to use any kind of doped and the amplification can be distributed, reducing the build-up of amplified spontaneous emission (ASE) noise. On the other hand, distributed Raman amplification has its own unique impair-

ments that have to be kept under control in order to obtain the full benefit of its comparative advantages. The most relevant of these impairments are the increased effect of double Rayleigh backscattering noise (DRBS) and the risk of increased relative intensity noise (RIN) due to transfer of amplitude fluctuations from the pump source to the amplified signal.

1.2 Historical Perspective

Although the first 'optical telegraph' was put in service in 1794 [3], optical signals were soon replaced by electrical signals and their use was not generalized again until the second half of the twentieth century. There were two main obstacles to the use of optical networks: the available optical sources were not coherent enough and there was not a transmission medium with low enough losses. The first problem was solved by the invention of the laser and its demonstration in 1960 [4]. As for the second problem, optical fiber was suggested to be an excellent medium for the propagation of optical signals in 1966 thanks to its capability for guiding the light, in a simile to how electrons are guided through copper wires. However, fibers available at the time had high losses, and it was not until Kao and Hockam demonstrated that these losses were mainly due to impurities of the fiber [5] and could be reduced that fiber optics became a viable option. The actual breakthrough happened in 1970 thanks to the work of Corning researchers (Kapron, Keck, and Maurer) who obtained a fiber which losses were below 20 dB/km for wavelengths in the proximity of 1 μm [6]. Simultaneously, GaAs semiconductor lasers, capable of continuous operation at such wavelengths at room temperature, were demonstrated [7]. After those discoveries, fiber-based lightwave systems became worthwhile.

Since the 1970s there has been a fast evolution of optical communica-

tions, leading to an increase in transmission capacity and distance. This improvement was made possible because of, among others, the development of optical amplification schemes. Initially, opto-electronic regenerators that periodically received the optical signal, converted it to the electrical domain, amplified it, applied noise filtering and then converted it back to the optical domain for it to be transmitted again, were used. However, these devices had important limitations, such as a small bandwidth and the inherent slowness of electronics, which introduced a cap in the bit-rate of the system. To avoid these problems, purely optical amplifiers based on rare earth doped fibers began to be studied and developed. Within this group, the EDFA (Erbium doped fiber amplifier), created in 1987 by Emmanuel Desurvire [8], was the most interesting device thanks to the emission wavelength of Erbium being close to 1550 nm (the losses in silica-based optical fibers reach a minimum at this wavelength). Finally, over the past 15 years Raman amplifiers and parametric amplifiers have gradually become more and more relevant, as they offer the possibility of distributed amplification along the transmission fiber without the need for special dopings, as well as they are able to operate over a broad bandwidth [2]. In this thesis our interest is on the application of Raman amplification which, as we have mentioned above and will see in more detail later on, offers some unique advantages.

In parallel to the development of optical communications, progress in the field of fiber optic sensors has also been considerable. The first optical sensor was patented in 1967 [9] and was based on bifurcated fiber bundles. Half the bundle was used to illuminate a surface whereas the other half of the bundle received the reflection from this surface and, measuring the delay, this device was able to provide information of the position of this surface. In the following decade, fiber optic interferometers began to be

used as sensors [10], exploiting the phase delay dependence on temperature, strain or pressure [11]. A particular case of interferometer is the fiber optic gyroscope based on the Sagnac effect, that measures the phase difference between two counterpropagating signals in a fiber coil attached to a rotating structure [12], this difference being proportional to the angular velocity. Some time afterwards, the idea of distributed sensors arose [13], in which any point along the length of the fiber can be simultaneously exploited as a sensor. Distributed sensors are, for example, not only able to detect atmospheric variations but also the particular position in which the change is taking place. Amongst others, sensors that exploit Brillouin scattering are particularly exploitable in optical fiber, thanks to the dependence of the Brillouin frequency shift on both local temperature and strain.

What we now know as the Raman effect was first predicted theoretically by the Austrian physicist Adolf Smekal in 1923 [14] and experimentally discovered in 1928 simultaneously by the team of Raman and Krishnan in India [15] and that of Mandelshtam and Landsberg [16] in the Soviet Union. It consists of a nonlinear inelastic dispersion of the light in which the energy transfer from the photon to the medium corresponds with an optical phonon. Its use in telecommunications was first proposed in 1980 [17] but it was deemed non-viable at the time because of the high pump powers required. Inexpensive lasers capable of providing high pump powers were made available at the end of the twentieth century, and since then, multiple configurations have been designed in order to reduce signal power variations along the transmission fiber through distributed fiber amplification [18, 19]. In 2004, J. D. Ania-Castañón proposed the ultra-long Raman laser configuration, that allowed quasi-lossless transmission in standard optical fiber by use of a second order Raman scheme and two fiber Bragg gratings to create

a resonant cavity [20, 21]. The potential advantages offered by this configuration in terms of design simplicity and reduced ASE noise build-up were later experimentally confirmed, and the device applied to both communications [22, 23, 24] and sensing [25]. An evolution of this configuration is the random distributed feedback fiber laser based on a mirrorless scheme and depicted in 2009 [26], whose practical application to sensing has also been recently demonstrated [27].

1.3 Objectives of this work

The main objectives of this thesis are:

- To study the impact of relative intensity noise (RIN) transfer on the performance of URFL and RDFL configurations, and find under which conditions this impairment can be reduced for the application of these devices to communication schemes and distributed optical fiber sensing applications.

- To study the advantages of URFLs in phase-coded communication systems, in which the optimal balance between noise and nonlinear impairment differs from that in amplitude coding schemes.

- To demostrate how the use of Raman amplification can be applied to improve the sensitivity and the measurement range of distributed optical fiber sensors and Sagnac-effect based interferometric sensors.

- To develop a tractable and computer friendly mathematical model for polarization-dependent Raman gain, and use it to adequately design and predict the behavior of a new kind of device, the Raman polarizer.

1.4 Structure of the thesis

This first chapter has set up the historical context of this work, including the motivation behind it.

Chapter 2 provides an introduction to the fundamental concepts of fiber optic communications and fiber non-linear effects. It includes the basic definition of fiber optics, a description of the wave propagation using the most usual mathematical model and an enumeration and description of the main nonlinear effects. The last part of the chapter is dedicated to Raman scattering and its application to amplification. The concepts of ultra-long Raman fiber lasers (URFL) and random distributed feedback Raman fiber lasers (RDFL) are also introduced here.

The following three chapters are devoted to presenting the bulk of the work and main results obtained during the thesis.

In chapter 3, a numerical analysis of RIN transfer in Raman amplification schemes is described. RIN is one of the most important impairments in Raman amplification systems and needs to be fully characterized in order to measure its impact on the output signal. Our analysis pays special attention to the study of RIN transfer in RDFL, which had never been studied before, but also to the comparative performance between cavity based URFLs and RDFLs.

Chapter 4 is entirely dedicated to a variety of novel applications of Raman amplification systems (first order, URFL and RDFL). Firstly, the use of URFL is compared with the use of traditional lumped amplification based upon Erbium doped fiber amplifiers (EDFAs) in telecommunication systems with phase modulation. Secondly, the improvement obtained in Raman assisted sensors is studied. Two cases are considered here: a fiber optic gyroscope and a Brillouin optical time domain analyzer (BOTDA). In both

types of sensors a theoretical analysis of the performance with any Raman configuration is carried out.

Chapter 5 includes an analysis of the evolution of the state of polarization in transmission over standard optical fibers under the impact of nonlinear effects. Here, the effects of SPM, XPM and Raman scattering are considered, to present the first universal treatment of polarization in optical fibers. As a particular case, the performance of an ideal Raman is described.

Finally, the summary and conclusions of this thesis are presented in Chapter 6. Here, I also present some of the future lines of work that can be derived from my thesis.

1.5 Publications resulting from this thesis

1.5.1 Chapters of books

1. V. V. Kozlov, J. Nuño, J. D. Ania-Castañón, and S. Wabnitz, *Trapping Polarization of Light in Nonlinear Optical Fibers: An Ideal Raman Polarizer,* in *Spontaneous Symmetry Breaking, Self-Trapping, and Josephson Oscillations*, Springer Berlin Heidelberg pp. 227-246 (2012).

1.5.2 Journal articles

1. J. Nuño, and J. D. Ania-Castañón, *RIN transfer in second-order amplification with centrally-pumped random distributed feedback fiber lasers,* Submitted to International Journal of Modern Physics b.

2. J. Nuño, and J. D. Ania-Castañón, *Cavity and random ultralong fiber laser amplification in BOTDAs: a comparison,* Submitted to Optics Express.

3. J. Nuño, and J. D. Ania-Castañón, *Fiber Sagnac interferometers with ultralong and random distributed feedback Raman laser amplification,* Optics and Lasers in Engineering **54** (1), pp. 21–26 (2014).

4. V. V. Kozlov, J. Nuño, J. D. Ania-Castañón, and S. Wabnitz, *Analytic theory of fiber-optic Raman polarizers,* Optics Express **20** (24), pp. 27242–27247 (2012).

5. J. Nuño, M. Alcon-Camas, and J. D. Ania-Castañón, *RIN transfer in random distributed feedback fiber lasers,* Optics Express **20** (24), pp. 27376–27381 (2012).

6. V. V. Kozlov, J. Nuño, J. D. Ania-Castañón, and S. Wabnitz, *Multi-Channel Raman polarizer with suppressed relative intensity noise for WDM transmission lines,* Optics Letters **37**, (21), pp. 2073–2075 (2012).

7. X. Angulo-Vinuesa, S. Martín-López, J. Nuño, P. Corredera, J. D. Ania-Castañón, L. Thévenaz, and M. González-Herráez, *Raman-assisted Brillouin distributed temperature sensor over 100 km featuring 2 meter resolution and 1.2 °C uncertainty,* Journal of Lightwave Technology **30** (8), pp. 1060–1065 (2012).

8. V. V. Kozlov, J. Nuño, J. D. Ania-Castañón, and S. Wabnitz, *Theoretical study of optical fiber Raman polarizers with counterpropagating beams,* Journal of Lightwave Technology **29** (3), pp. 341–347 (2011).

9. V. V. Kozlov, J. Nuño, and S. Wabnitz, *Theory of lossless polarization attraction in telecommunication fibers,* Journal of the Optical Society of America B **28** (1), pp. 100–108 (2011).

10. V. V. Kozlov, J. Nuño, J. D. Ania-Castañón, and S. Wabnitz, *Theory of fiber optic Raman polarizers,* Optics Letters **35** (23), pp. 3970–3972 (2010).

1.5.3 Contributions to international congresses

1. V. V. Kozlov, J. Nuño, J. D. Ania-Castañón, and S. Wabnitz, *Analytic theory of fiber-optic Raman polarizers,* in *Nonlinear photonics 2012*, Colarado Springs (USA), 2012.

2. J. Nuño, M. Alcon-Camas, and J. D. Ania-Castañón, *RIN transfer in random distributed feedback fiber lasers,* in *Nonlinear photonics 2012*, Colarado Springs (USA), 2012.

3. S. Wabnitz, V. V. Kozlov, J. Nuño, and J. D. Ania-Castañón, *Theory of Fiber Optic Co- and Counter-pumped Raman Polarizers,* in *2011 Conference on Lasers and Electro-Optics Europe and 12th European Quantum Electronics Conference*, Munich (Germany), 2011.

4. S. Wabnitz, V. V. Kozlov, and J. Nuño, *Theory of Fiber Optic Lossless Polarizers,* in *2011 Conference on Lasers and Electro-Optics Europe and 12th European Quantum Electronics Conference*, Munich (Germany), 2011.

5. X. Angulo-Vinuesa, S. Martín-López, J. Nuño, P. Corredera, J. D. Ania-Castañón, L. Thévenaz, and M. González-Herráez, *Hot spot detection over 100km with 2 meter resolution in a Raman-assisted Brillouin distributed sensor,* in *International Conference on Optical Fiber Sensors 2011*, Ottawa (Canada), 2011.

6. J. Nuño, and J. D. Ania-Castañón, *Fiber Optic Gyroscope Assisted by*

Raman Amplification, in *International Conference on Applications of Optics and Photonics*, Braga (Portugal), 2011.

1.5.4 Contributions to national congresses

1. J. Nuño, and J. D. Ania-Castañón, *SPM and RIN transfer impairments in BOTDA sensors using random distributed feedback and ultralong Raman cavity fiber laser amplification ,* in *VIII Reunión Española de Optoelectrónica, OPTOEL 13*, Alcalá de Henares, 2013.

2. J. Nuño, V. V. Kozlov, J. D. Ania-Castañón, and S. Wabnitz *Theoretical analysis of fiber optic Raman polarizers,* in *VII Reunión Española de Optoelectrónica, OPTOEL 11*, Santander, 2011.

3. X. Angulo-Vinuesa, S. Martín-López, J. Nuño, P. Corredera, J. D. Ania-Castañón, and M. González-Herréaez, *Sensor de temperatura BOTDA asistido por Raman, de 2 metros de resolución sobre 100 km de distancia,* in *VII Reunión Española de Optoelectrónica, OPTOEL 11*, Santander, 2011.

4. J. Nuño, and J. D. Ania-Castañón, *Interferómetros de fibra asistidos por amplificación Raman,* in *I Reunión del comité de óptica cuántica y no lineal, QUONLOP 11*, Valladolid, 2011.

5. X. Angulo-Vinuesa, S. Martín-López, J. Nuño, P. Corredera, J. D. Ania-Castañón, and M. González-Herréaez, *Raman-assisted BOTDA Temperature Sensor Featuring 100 km Dynamic Range with 2 meter Resolution,* in *I Reunión del comité de óptica cuántica y no lineal, QUONLOP 11*, Valladolid, 2011.

Chapter 2

Preliminary concepts

2.1 Optical fibers

An optical waveguide is a structure that guides electromagnetic waves in the optical region of the electromagnetic spectrum (ranging from 50 nm to 100 mm) from one point to another. The most extensively used optical waveguide is the optical fiber, made of glass (silica) or plastic, due to its flexibility, versatility and small losses. In this, the light is guided thank to the phenomenon of total internal reflection, which has been demonstrated in many different media as water [28, 29] or an human hair [30].

To explain the phenomenon of total internal reflection, we consider the simplest type of optical fiber, known as step index fiber [1, 31, 32, 33]. Such kind of fibers consist on a cylindrical glass core surrounded by a cladding layer and, often, there is also a jacket layer to protect the fiber. The refractive index in the core is slightly higher than in the cladding and total internal reflection is possible inside the core when the light beam impinges upon the boundary between core and cladding with an angle larger than the

critical angle, defined as

$$\theta_c = arcsin(\frac{n_{cladding}}{n_{core}}) \tag{2.1}$$

where $n_{cladding}$ and n_{core} are the refractive indexes of the cladding and the core, respectively. In analogy with lenses, we can also define the numerical aperture (NA) of the fiber as NA= $n_{core}\sin(\theta_{max})$ where θ_{max} is the maximum angle at which the light entering the fiber will be confined in the core. Note that $\theta_{max} = \pi/2 - \theta_c$, so this expression can be simplified to

$$NA = n_{core}\cos\theta_c = \sqrt{n_{core}^2 - n_{cladding}^2} \tag{2.2}$$

Apart from step index fibers, other types of fibers are available. In a graded index fibre, the core index decreases gradually from the center with a parabolic profile. The objective of these fibers is to reduce the differences in transmission speed between two beams that follow different paths. More recently developed types of fibers include microstructured fibers, of which a particular subset is photonic crystal fibers (PCFs). PCFs have periodic optical nanostructures specially designed to facilitate different nonlinear effects for special applications [34].

Another possible classification of the fibers pays attention to the number of transverse fiber modes allowed for radiation propagating through the fiber. A fiber mode is each particular solution of the wave equation based on the Maxwell equations (to be detailed in the next section). The number of solutions is dependent on the core radius (r) and the wavelength (λ) of the used light. The parameter V has information of the number of modes supported by the fiber.

$$V = \frac{2\pi r}{\lambda}NA \tag{2.3}$$

The fiber will be single-mode if $V \leq 2.405$. According to the International Telecommunication Union (ITU) [35, 36], multimode fibers for telecommunication applications must have a core diameter of 50 μm and use 800 nm or 1300 nm wavelength lights whereas the core diameters of single mode fibers must be less than 10 μm and operate with light at 1300 nm or 1550 nm. In both cases, the cladding diameter is typically 125 μm.

The operation wavelength is determined by the effects of the attenuation and dispersion as well as the availability of light sources and detectors. The reason for using 800 nm wavelength in primitive fibers is found on their loss spectrum. Current fibers, on the other hand, present zero dispersion at 1300 nm and minimum attenuation at 1550 nm.

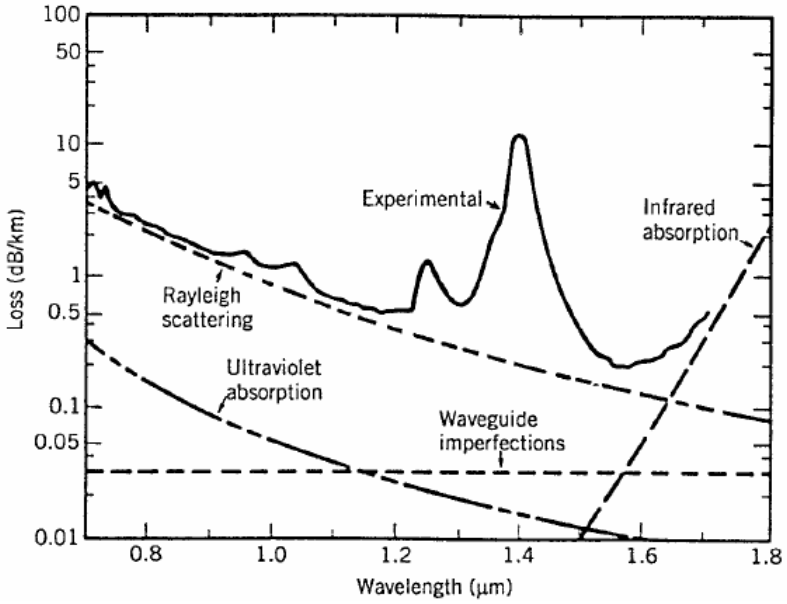

Figure 2.1: Loss spectrum of a single-mode fiber produced in 1979. Wavelength dependence of several fundamental loss mechanisms. After [1, 37].

The loss spectrum of a standard fiber and the main mechanisms that produce it are depicted in figure 2.1. The main causes for the combined fiber loss are absorption losses (intrinsic or extrinsic) and scattering losses.

Whilst intrinsic material absorbtion is negligible in the wavelength regions of interest to optical communication, extrinsic absorption losses, due to the presence of impurity ions, must be taken into account. The most important extrinsic absorption loss happens at 1.38 μW due to OH^- ions from water vapor, but the absorption band for OH^- ions is narrow enough not to affect a signal at 1550 nm. Regarding scattering losses, during a scattering process light is not absorbed, but instead interacts with the medium and is scattered at a random angle. Nonlinear scattering implies a change in the light wavelength (i.e. an energy exchange with the medium) whereas linear scattering (Rayleigh scattering) does not introduce changes on the signal wavelength. Rayleigh scattering is caused by small-scale inhomogeneities produced in the fiber fabrication process, that change the medium density or the refractive index. Attenuation occurs whenever the light is scattered at an angle that is not supported by the fiber. Rayleigh scattering also plays an important role when the light is doubly backscattered, leading to double Rayleigh backscattering noise (DRBS) and multi-path interference. In section 2.4, we will explain the use of optical amplifiers to compensate signal attenuation due to fiber losses.

2.2 Wave propagation in optical fibers

Like all electromagnetic phenomena, Maxwell's equations govern the propagation of the light in optical fibers [38]:

$$\nabla \times \mathbf{E} = -\frac{\partial \mathbf{B}}{\partial t} \tag{2.4}$$

$$\nabla \times \mathbf{H} = \mathbf{J} + \frac{\partial \mathbf{D}}{\partial t} \tag{2.5}$$

$$\nabla \cdot \mathbf{D} = \rho \tag{2.6}$$

$$\nabla \cdot \mathbf{B} = 0 \tag{2.7}$$

where $\mathbf{H}$ and $\mathbf{E}$ are the magnetic and the electric field vectors, respectively; $\mathbf{D}$ and $\mathbf{B}$ are the corresponding flux densities, $\mathbf{J}$ is the electric current density and ρ is the charge density. Since the optical fiber is a non conductive medium, there are not free charges and $\mathbf{J}$ and ρ are equal to 0. The relationships between the field vectors and the flux densities are:

$$\mathbf{D} = \epsilon_0 \mathbf{E} + \mathbf{P} \tag{2.8}$$

$$\mathbf{B} = \mu_0 \mathbf{H} + \mathbf{M} \tag{2.9}$$

where ϵ_0 is the vacuum permittivity and μ_0 is the vacuum permeability, $\mathbf{P}$ is the induced electric polarization and $\mathbf{M}$ is the magnetic one (zero for a nonmagnetic material). The combination of equations 2.4-2.9 produces:

$$\nabla \times \nabla \times \mathbf{E} + \frac{1}{c^2}\frac{\partial^2 \mathbf{E}}{\partial t^2} = -\mu_0 \frac{\partial^2 \mathbf{P}}{\partial t^2} \tag{2.10}$$

where the speed of the light (c) is obtained from $c = (\mu_0 \epsilon_0)^{-1/2}$. The last step consists in defining the polarization vector $\mathbf{P}$ as function of $\mathbf{E}$:

$$\begin{gathered}
\mathbf{P}(\mathbf{r},t) = \epsilon_0 \textstyle\int_{-\infty}^{+\infty} \chi^{(1)}(t-t') \cdot \mathbf{E}(\mathbf{r},t')\partial t' \\
+\epsilon_0 \textstyle\int\int_{-\infty}^{+\infty} \chi^{(2)}(t-t_1, t-t_2) : \mathbf{E}(\mathbf{r},t_1)\mathbf{E}(\mathbf{r},t_2)\partial t_1 \partial t_2 + \\
\epsilon_0 \textstyle\int\int\int_{-\infty}^{+\infty} \chi^{(3)}(t-t_1, t-t_2, t-t_3) \vdots \mathbf{E}(\mathbf{r},t_1)\mathbf{E}(\mathbf{r},t_2)\mathbf{E}(\mathbf{r},t_2)\partial t_1 \partial t_2 \partial t_3 \\
+ ...
\end{gathered} \tag{2.11}$$

where the first term corresponds to the linear polarization (P_L) and the next terms correspond to the nonlinear polarization (P_{NL}). Usually, the nonlinear terms higher than the third term can be neglected and, in the

particular case of common optical fibers, the even terms cancel each other out because silica is a centrosymmetric molecule. Then, our interest is only in the first and the third terms. Below, we study the linear and nonlinear propagations separately.

2.2.1 Linear propagation

In the case of low optical power, the nonlinear term is neglected. In this case, by introducing the Fourier transform, the equation 2.10 is simplified to:

$$\nabla \times \nabla \times \tilde{\mathbf{E}} = -\epsilon(\mathbf{r}, \omega)\frac{\omega^2}{c^2}\tilde{\mathbf{E}} \tag{2.12}$$

where the Fourier transform of $\mathbf{E}$ is:

$$\tilde{\mathbf{E}}(\mathbf{r}, \omega) = \frac{1}{2\pi}\int_{-\infty}^{+\infty} \mathbf{E}(\mathbf{r}, t)e^{i\omega t}\partial t \tag{2.13}$$

and the dielectric constant in the frequency domain is defined as:

$$\epsilon(\mathbf{r}, \omega) = 1 + \tilde{\chi}(\mathbf{r}, \omega) \tag{2.14}$$

where $\tilde{\chi}$ is the Fourier transform of χ. This dielectric constant has a real part and an imaginary part, which are related to the refractive index (n) and the absorption coefficient (α) respectively as:

$$n(\omega) \approx 1 + \frac{1}{2}\Re[\chi] \tag{2.15}$$

$$\alpha(\omega) = \frac{\omega}{nc}\Im[\chi] \tag{2.16}$$

Another simplification can be made if we consider that $\alpha = 0$ and n are independent of the spatial coordinate $\mathbf{r}$ in both the core and the cladding.

After that, equation 2.12 is:

$$\nabla^2\tilde{\mathbf{E}} + n^2\frac{\omega^2}{c^2}\tilde{\mathbf{E}} = 0 \tag{2.17}$$

A complete analysis of the linear propagation regime can be found in [1, 39]. Here, we simply show the result. Taking spherical coordinates (z,r,ϕ), the solution for the z component is:

$$\tilde{E}_z(\mathbf{r},\omega) = \tilde{A}(\omega)F(r)e^{\pm im\phi}e^{i\beta z} \tag{2.18}$$

where $\tilde{A}(\omega)$ is the amplitude term and β is the propagation constant. Also, F(r) represents the modal distribution of each fiber mode, that usually takes the form of a Bessel function. The constant m is restricted to take only integer values since the field must be periodic in ϕ with a period of 2π. The solution for the fundamental mode corresponds to $m = 0$.

Chromatic dispersion

Chromatic dispersion is another important impairment that affects a signal propagating through an optical fiber. Dispersion is produced by the frequency dependence of β. To explain it, β can be written as a Taylor series around the carrier frequency ω_0:

$$\beta(\omega) = \beta_0 + \beta_1(\omega - \omega_0) + \frac{1}{2}\beta_2(\omega - \omega_0)^2 + ... \tag{2.19}$$

where

$$\beta_i = \frac{\partial^i\beta}{\partial\omega^i}|_{\omega=\omega_0} \tag{2.20}$$

These β_i parameters contain information about the phase velocity (v_p) and the group velocity (v_g). The phase velocity is the rate at which the

phase of the wave propagates through space and it is defined as the ratio between ω and β. On the other hand, the group velocity is the velocity with which the envelope of the wave propagates through space and it is calculated as:

$$v_g = \frac{\partial \omega}{\partial \beta} = \frac{1}{\beta_1} \tag{2.21}$$

Although both velocities are not usually identical, their values in optical fiber transmission are similar ($\approx 2 \times 10^8$ m/s). Chromatic dispersion causes group velocity dispersion (GVD), as group velocity depends on ω. Chromatic dispersion is typically characterized by β_2, as

$$\beta_2 = \frac{\partial}{\partial \omega}(\frac{1}{v_g}) = \frac{\partial \tau_g}{\partial \omega} \tag{2.22}$$

where τ_g is the group delay. Typically, in addition to β_2, another parameter is used to characterize dispersion:

$$D = \frac{\partial}{\partial \lambda}(\frac{1}{v_g}) = -\frac{2\pi c}{\lambda^2}\beta_2 \tag{2.23}$$

D is referred to as the dispersion parameter and is expressed in units of ps/(km·nm). As dispersion produces different delays for different frequency components, its effect is a broadening of the pulsed signals in the time domain. The wavelength at which D=0, denoted as the zero-dispersion wavelength λ_0, separates the dispersion in the fiber in two regions: one with normal dispersion (the value of D is negative) and one with anomalous dispersion (the value of D is positive). The use of fibers with zero-dispersion at the wavelength of transmission is not convenient because of the arising of nonlinear effects, that can not be partially canceled by dispersion and hence dominate transmission, distorting the signal. Since in SMF dispersion is

anomalous at 1550nm, fibers with normal dispersion are introduced after the transmission in order to compensate this impairment.

When the transmitted signal has a broad optical spectrum, one has to consider higher order dispersion effects or the dispersion slope $S = \partial D/\partial\alpha$. The parameter S is also called the differential-dispersion parameter.

Polarization-Mode Dispersion

Even single-mode fibers are not truly single-mode, as they admit two orthogonal polarization modes. These modes have the same group delay in a fiber with perfect radial symmetry but, in real fibers, there are many asymmetries that lead to a mixing of the two polarization states by breaking the mode degeneracy [40]. This difference is known as optical birefringence and it is the origin of polarization-mode dispersion (PMD). The mathematical definition of birefringence is [41]:

$$B_m = |n_x - n_y| = \frac{|\beta_x - \beta_y|}{k_0} \tag{2.24}$$

Due to this birefringence, the state of polarization of the light beam changes during its transmission. The beat length (L_B) is defined as the propagation distance for which the polarization rotates through a full cycle. A typical value of L_B is 10 m.

$$L_B = \frac{2\pi}{|\beta_x - \beta_y|} = \frac{\lambda}{B_m} \tag{2.25}$$

For short fibers, PMD effects can be seen as deterministic. However, B_m is not constant along the optical fiber, but actually a random variable. As a result, for long distances the state of polarization (SOP) of the beam also changes randomly and PMD effects become stochastic. The parameter used

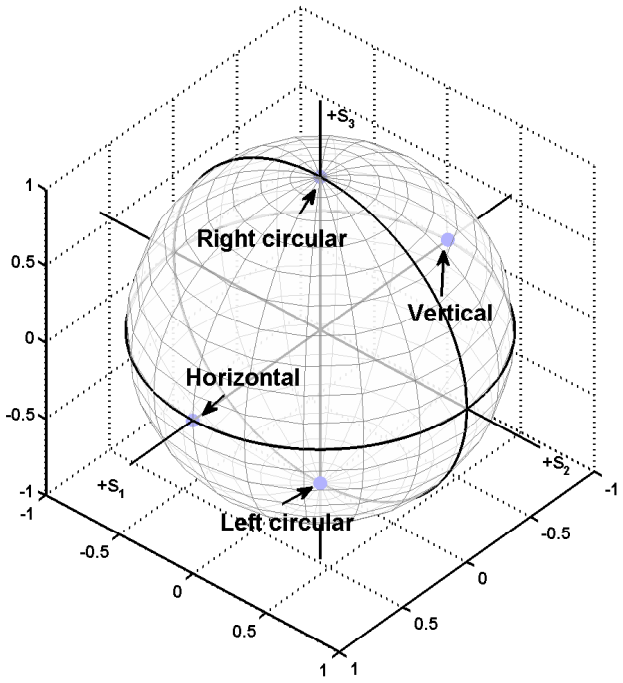

Figure 2.2: Representative points on the surface of the Poincaré sphere.

to distinguish between the short-length regime and the long-length regime is the correlation length (L_c). While the input polarization is fixed (assuming $\langle P_{\parallel} \rangle = 1$ and $\langle P_{\perp} \rangle$=0), it is equally probable to observe any polarization state at long enough lengths ($\langle P_{\parallel} \rangle - \langle P_{\perp} \rangle \rightarrow 0$ for $L >> L_c$). By definition [40], at L_c:

$$\langle P_{\parallel} \rangle - \langle P_{\perp} \rangle = \frac{1}{e^2} \tag{2.26}$$

Assuming that the rate of change of the birefringence orientation (θ) is driven by a white noise process (g_θ) [42] where $\langle g_\theta(z) \rangle = 0$ and $\langle g_\theta(z) g_\theta(z') \rangle = \sigma_\theta^2 \delta(z' - z)$, the fiber auto-correlation is

$$\langle cos[\theta(z) - \theta(0)] \rangle = \langle cos[\int_0^z g_\theta(z') \partial z'] \rangle = \exp(-\frac{\sigma_\theta^2}{2} z) \tag{2.27}$$

which implies that $L_c = \frac{2}{\sigma_\theta^2}$.

Generally, fiber manufacturers specify the PMD parameter, measured in $\mathrm{ps}/\sqrt{km}$ and defined as [43],

$$D_p = \frac{2\sqrt{(2)}\pi\sqrt{(L_c)}}{L_B\omega_s} \tag{2.28}$$

However, as it is explained in chapter 5, it is preferable to consider the beat and correlation lengths separately to obtain full information about the fiber.

To conclude this section it is convenient to introduce the Stokes formalism. The Stokes formalism is a complete description of the state of polarization that we will use later in the results chapters when dealing with Raman polarizers. In this formalism, we define a vector ($\mathbf{S} = (S_1, S_2, S_3)$) indicating the polarization of the field, whose components are $S_1 = E_x E_y^* + E_y E_x^*$, $S_2 = i(E_y E_x^* - E_x E_y^*)$ and $S_3 = |E_x|^2 - |E_y|^2$. Moreover, the power of the beams is described by a fourth component $S_0 = |E_x|^2 + |E_y|^2$. Components 1, 2 and 3 of the Stokes vector ($\mathbf{S}$) can be represented in a tree-dimensional space. All possible value forms an unit sphere known as the Poincaré sphere. In this sphere, linear polarizations are plotted along the equator, circular ones are at the poles and elliptical ones are elsewhere (see figure 2.2).

2.2.2 Nonlinear propagation

Nonlinear effects become relevant when short pulses (typically of 10 ns of less) are used. Here, the starting point for their accurate description is equation 2.10 taking into account the linear part and non-linear part of the polarization vector ($\mathbf{P}$). As we previously pointed out, the non-linear part of the polarization vector corresponds only to the third order susceptibility tensor. Moreover, this tensor has only four non-negligible components

$(\chi^{(3)}_{xxxx}(t), \chi^{(3)}_{xxyy}(t), \chi^{(3)}_{xyxy}(t), \chi^{(3)}_{xyyx}(t))$ that, under the Born-Oppenheimer approximation [44], can be written as:

$$\chi^{(3)}_{ijkl}(t-t_1, t-t_2, t-t_3) = \chi^{(3)} R_{ijkl}(t-t_1)\delta(t-t_2)\delta(t-t_3) \tag{2.29}$$

where the normalized non-linear responses (R_{ijkl}) have an almost instantaneous term (σ_{ijkl}) and a retarded term (h_{ijkl}), associated with nonlinear scattering:

$$R_{ijkl} = \sigma_{ijkl}\delta(t) + h_{ijkl}(t) \tag{2.30}$$

The values of σ_{ijkl} and h_{ijkl} are simplified under the Kleinman symmetry conditions[45]: $\sigma_{xyxy} = \sigma_{xxyy} = \sigma_{xyyx} = \sigma_{xxxx}/3$. The retarded term has only two independent components denoted as $h_{\parallel}$ and $h_{\perp}$, that correspond, respectively, to the parallel and perpendicular medium responses to the pump polarization.

To solve the non-linear propagation problem, some simplifications can be assumed. Firstly, polarization is considered to be maintained along the fiber length. Although as we will see in our treatment of Raman polarisers (chapter 5) this is not always true, it simplifies calculations and the result is accurate for most common situations. Also, we should consider that most nonlinear effects, except for Raman scattering, are almost instantaneous. With these considerations, equation 2.10 is written in the frequency domain as,

$$\begin{aligned}\nabla^2\tilde{E} + \epsilon(\omega)\frac{\omega^2}{c^2}\tilde{E} = \chi^{(3)}_{xxxx}\frac{\omega^2}{c^2}\int\int_{-\infty}^{\infty}\tilde{R}(\omega_1-\omega_2) \\ \tilde{E}(\omega-\omega_1+\omega_2)\tilde{E}(\omega_1)\tilde{E}^*(\omega_2)\partial\omega_1\partial\omega_2\end{aligned} \tag{2.31}$$

Similarly to the case of the linear analysis, a solution of this equation in

spherical coordinates (z, r, ϕ) is found as,

$$\mathbf{E}(\mathbf{r},t) = \frac{1}{2}\hat{x}[A(t)F(r)exp(i(\omega_0 t - \beta_0 z)) + c.c.] \tag{2.32}$$

The nonlinear contribution is considered as a perturbation of the linear case ($n = n_0 + n_2|E|^2$). The distribution of the fundamental mode is not affected by the nonlinear effects, however they modify the propagation constant (β) as it is illustrated in section 2.3.1. As a last step, we obtain the equation for the evolution of the normalized complex amplitude (A) by means of different mathematical tools. The complete process is shown in [46]. The equation, that includes losses, dispersion and the main nonlinear effects, is:

$$\begin{aligned} &\frac{\partial A}{\partial z} + \frac{\alpha}{2}A + \beta_1\frac{\partial A}{\partial t} + \frac{i\beta_2}{2}\frac{\partial^2 A}{\partial t^2} - \frac{\beta_3}{6}\frac{\partial^3 A}{\partial t^3} \\ &= i\gamma(1 + \frac{i}{\omega_0}\frac{\partial}{\partial t})(A(z,t)\int_{-\infty}^{\infty}\frac{1}{\chi_{xxxx}}R_{xxxx}(t_1)|A(z,t-t_1)|^2 dt_1) \end{aligned} \tag{2.33}$$

where γ is a constant used to measure the nonlinearity of the fiber, known as the nonlinear parameter, which is related to the third order susceptibility as:

$$\gamma = \frac{3\sigma_{xxxx}\omega_0}{8ncA_{eff}} = \frac{n_2\omega_0}{cA_{eff}} \tag{2.34}$$

n_2 is the nonlinear refractive index as it is described in section 2.3.1 whereas A_{eff} is the effective core area of the fiber for the propagating beam, defined as

$$A_{eff} = \frac{(\int\int_{-\infty}^{\infty}|F(x,y)|^2\partial x\partial y)^2}{\int\int_{-\infty}^{\infty}|F(x,y)|^4\partial x\partial y} \tag{2.35}$$

This parameter measures the real area of the field inside the fiber. Since its calculation depends on the distribution of the fundamental mode, its value is affected by the core radius, the core-cladding index difference and the operating frequency. A typical value for SMF with a signal propagating at a wavelength of 1550 nm is 84 μm^2.

For pulses longer than 1 ps and up to the continuous regime, it is possible to consider the medium response as instantaneous and equation 2.33 is expressed as:

$$\frac{\partial A}{\partial z} + \frac{\alpha}{2}A + \beta_1 \frac{\partial A}{\partial t} + \frac{i\beta_2}{2}\frac{\partial^2 A}{\partial t^2} = i\gamma A|A|^2 \tag{2.36}$$

This equation is often referred to as the nonlinear Schrödinger equation (NLSE) and it is generally the simplest and most efficient way to describe the propagation of optical pulses including attenuation, dispersion and nonlinear effects in fibers.

In some particular cases of transmission over short distances, it is possible to neglect dispersion or the nonlinear effects in the analysis of the NLSE. To distinguish these cases, two parameters are defined:

$$L_D = \frac{T_0^2}{\beta_2} \tag{2.37}$$

$$L_{NL} = \frac{1}{\gamma P_0} \tag{2.38}$$

where T_0 is the input pulse width and P_0 is its peak power. When fiber length is $L << L_{NL}$ (nonlinear length) or $L << L_D$ (dispersion length) respectively, nonlinear effects or dispersion can be neglected. Similarly, comparing the relative values of nonlinear and dispersion length will give us information on whether dispersive or nonlinear effects dominate the propagation of the signal.

The last concept to explain in this section is the effective length (L_{eff}). Because the nonlinearities are directly dependent on the signal power, its relevance decreases as the signal is degraded by the attenuation. L_{eff} is defined from the expression,

$$P_0 L_{eff} = \int_0^L P(z)dz \tag{2.39}$$

Assuming that signal power is exponentially decreasing with length due to fiber loss (α), it yields

$$L_{eff} = \frac{1 - e^{-\alpha L}}{\alpha} \tag{2.40}$$

For short distances or lossless systems, $L_{eff} = L$ whilst for a long distance of SMF fiber L_{eff} ≈22 km for a wavelength of 1550 nm.

2.3 Nonlinear effects in optical communications

The nonlinear effects in optical fiber can be classified into inelastic or elastic depending on whether energy is exchanged or not between the electromagnetic field and the dielectric medium. Among the elastic effects there are important phenomena such as harmonic generation, four wave mixing (FWM) and nonlinear refraction. The two first effects, also known as parametric processes, involve the generation of new frequencies and, unless special efforts are made to achieve phase matching, they are not efficient in optical fibers. Here we firstly explain nonlinear refraction and parametric processes and later, we focus on the inelastic effects such as Brillouin scattering and Raman scattering, which will be of particular relevance in this thesis.

2.3.1 Nonlinear refraction

Most of the nonlinear effects in optical fibers therefore originate from nonlinear refraction or Kerr nonlinearity, a phenomenon referring to the intensity dependence of the refractive index

$$n = n_0 + n_2|E|^2 \tag{2.41}$$

where the nonlinear-index coefficient (n_2) has been defined as

$$n_2 = \frac{3}{8n} Re(\chi^3_{xxxx}) \tag{2.42}$$

A typical value of n_2 in standard fibers is $2\times10^{-20}\ m^2W^{-1}$ [47]. The nonlinear refraction leads to two important nonlinear effects: self-phase modulation (SPM) and cross-phase modulation (XPM). Self-phase modulation is a self-induced phase shift suffered by an optical field that is propagating through an optical fiber. Mathematically, the phase shift experienced by the optical field can be expressed as

$$\phi = nk_0L = (n_0 + n_2|E|^2)k_0L \tag{2.43}$$

where $k_0 = \omega/c = 2\pi/\lambda$ and the second term, dependent on the optical field, is the accumulated nonlinear phase. This phenomenon is the reason for the spectral broadening of ultrashort pulses [48]. Analyzing the combined effect of dispersion and SPM, we note that, in the anomalous-dispersion regime, the GVD induced pulse-broadening is reduced by the effect of SPM. In fact, there is a particular kind of optical pulses that can propagate without distortion, they are known as solitons [49, 50]. In the case of normal GVD, an extra broadening occurs.

Cross phase modulation, on the other hand, refers to the phase shift induced by another optical field, with different wavelength, direction, or state of polarization, propagating simultaneously to the affected field through the same fiber. The total nonlinear phase shift, including both SPM and XPM can be expressed as

$$\phi_{NL} = n_2 k_0 L(|E_1|^2 + 2|E_2|^2) \tag{2.44}$$

where the first term includes SPM and the second one is the XPM. An important feature of XPM is that its contribution is twice that of SPM [51]. Among other things, XPM is responsible for the asymmetric spectral broadening of co-propagating optical pulses [52].

2.3.2 Parametric processes

Parametric processes in optical fiber are generally caused by third-order susceptibility. Among them, four wave mixing (FWM) is widely studied because of its high efficiency for generating new waves [53].

FWM can occur when at least two different frequency components (ω_1 and ω_2) propagate in the optical fiber. This produces a refractive index modulation at the frequency of the difference ($\omega_2 - \omega_1$, assuming $\omega_2 > \omega_1$). In the degenerate case, there are no other optical waves with a different frequency and the new frequencies generated are: $\omega_3 = 2\omega_2 - \omega_1$ and $\omega_4 = 2\omega_1 - \omega_2$. In the non-degenerate case, another optical wave with a frequency ω_3 propagates in the fiber and the new frequencies generated are: $\omega_4 = \omega_3 \pm (\omega_2 - \omega_1)$ [54].

The efficiency of the parametric processes is determined by the phase matching condition. This means that a proper phase relationship between

the interacting waves is necessary. In the case of FWM, the maximum gain is obtained when the accumulative phase of the two waves are identical. To obtain this phase matching, optical waves should transmit close to the zero-dispersion wavelength.

FWM can be used for parametric amplification or the generation of new wavelengths [55]. On the other hand, it can be a noise source when several channels are co-propagating with wavelength-division multiplexing (WDM).

Parametric amplifier work in the degenerative case. Initially there are two waves at wavelength ω_p (pump) and ω_s (signal) and a new wave is generated at wavelength $\omega_i = 2\omega_p - \omega_s$ (idler). The equations of the evolution of the three signals were:

$$\frac{dA_p}{dz} = i\gamma[(|A_p|^2 + 2(|A_s|^2 + |A_i|^2))A_p + 2A_iA_sA_p^* \exp(i\Delta\beta z)] \quad (2.45)$$

$$\frac{dA_s}{dz} = i\gamma[(|A_s|^2 + 2(|A_i|^2 + |A_p|^2))A_p + 2A_i^*A_p^2 \exp(-i\Delta\beta z)] \quad (2.46)$$

$$\frac{dA_i}{dz} = i\gamma[(|A_i|^2 + 2(|A_s|^2 + |A_p|^2))A_p + 2A_s^*A_p^2 \exp(-i\Delta\beta z)] \quad (2.47)$$

Here, only SPM, XPM and FWM are considered, neglecting other terms (Raman, Rayleigh and fiber losses). $\Delta\beta$ is defined as $\Delta\beta = \beta(\omega_s) + \beta(\omega_i) - 2\beta(\omega_p)$. The explanation of these equations can be found in [56, 57].

2.3.3 Inelastic scattering

A scattering process is the dispersal of a beam of radiation into a range of directions as a result of physical interactions. In fiber optics, three scattering processes are particularly important: Rayleigh scattering, Raman scattering and Brillouin scattering. Other forms of light scattering, such as Mie scattering, have very limited relevance and only in very specific situations (e.g. at the core-cladding interface of polymer optical fibers). Simplified energy

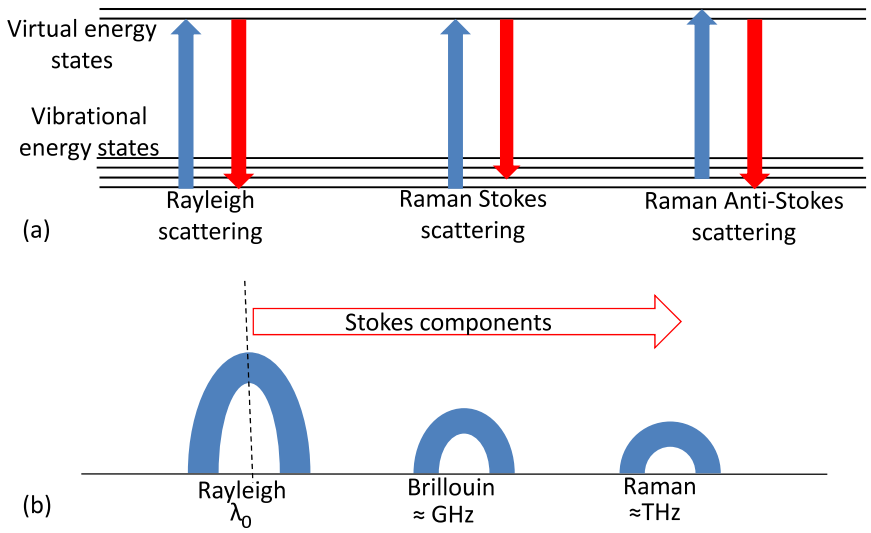

Figure 2.3: (a) Energy diagram for different scattering processes. (b) Schematic frequency shift differences for different scattering processes.

diagrams for those three main processes are depicted in figure 2.3(a). The simplest is Rayleigh scattering, a linear and elastic process (the frequency of the radiated light is identical to incident light). In optical communications, Rayleigh effect contributes to increasing losses by scattering photons beyond the critical angle, and DRBS is a critical source of noise in Raman amplification [58, 59].

Raman and Brillouin effects are nonlinear and inelastic scatterings, dependent on the intensity of the incident light and leading to wavelength shifts. In the basic quantum-mechanical representation, an incident photon (called the pump photon) is absorbed by the silica molecule which then radiates a photon at lower frequency (Stokes wave), and emits a phonon to preserve both energy and momentum. The creation of an anti-Stokes wave (emission at higher frequency) is generally a much less probable occurrence because it requires the scattering molecule to be already on an excited

state, with the corresponding phonon energy available to be transferred to the emitted photon.

A particular case is the stimulated scattering (stimulated Raman scattering, SRS or stimulated Brillouin scattering, SBS) [60, 61], that happens when two signals (a pump and a signal) are propagating by the same medium. As a condition, the pump has to be enough intensive and the signal frequency has to be close to the Stokes frequency. Part of the energy of the pump is absorbed and the generated photons are a copy of the signal photons. Occasionally, a signal generated by spontaneous scattering can act as a seed for following stimulated processes. This is the basis of the performance of Raman lasers.

A simple mathematical description of SRS is,

$$\begin{aligned} \frac{\partial I_p}{\partial z} &= \pm g_R \frac{\nu_p}{\nu_s} I_p I_s \\ \frac{\partial I_s}{\partial z} &= g_R I_p I_s \end{aligned} \tag{2.48}$$

where g_R is the Raman gain coefficient and the sign in the first equation varies if the signals are co-propagating (-) or counter-propagating (+). Replacing g_R by g_B (Brillouin gain coefficient), we obtain the equation that governs the SBS. The value of g_R (or g_B) is variable with the frequency shift between the pump and the signal and it is affected by the composition of the core of the fiber. A representation of the Raman-gain spectrum for fused silica is in figure 2.4. As can be seen, g_R is not null over a large frequency range (up to 40 THz) and the maximum is reached for the frequency component shifted from the pump frequency by about 13.2 THz [62]. This is a typical behaviour of amorphous materials such as fused silica. In these materials, molecular vibrational frequencies extend into bands that overlap

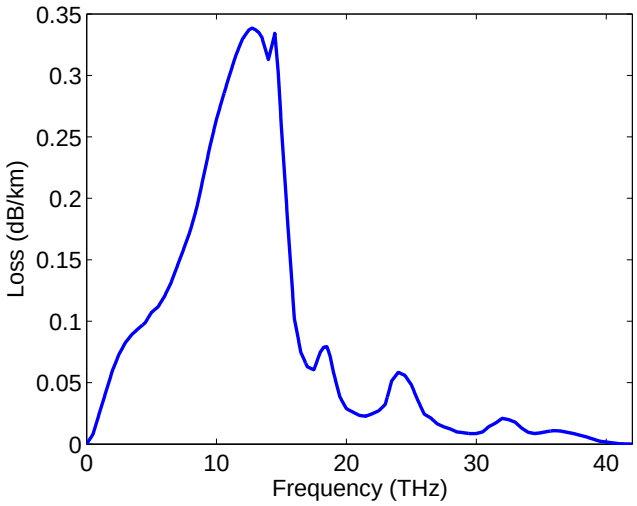

Figure 2.4: Raman-gain spectrum for fused silica at a pump wavelength $\lambda_p = 1.45\mu m$.

and create a continuum [63]. On the other hand, in other materials, Raman scattering only happens at specific well-defined frequencies. In any case, the structure of vibrational levels is univocally linked to the molecular structure of the medium. This is one of the reasons why Raman scattering is so useful in spectroscopy.

The main physical difference between Raman and Brillouin effects lies in the form of the generated phonon: an optical phonon (Raman effect) or an acoustic phonon (Brillouin effect). In the Brillouin effect, the generated acoustic wave produces a modulation of the refractive index of the core. It produces the scattering of the incident beam and, as the acoustic wave is moving with a velocity v_A, the scattered light is downshifted in frequency due to the Doppler shift.

This difference leads to important differences in the resulting scattering spectrum for both effects. A fundamental one is that SBS only happens between counter-propagating signals whilst SRS can occur in both directions.

This is because the Brillouin shift (Ω_b) satisfies the standard dispersion relation:

$$\Omega_b = \upsilon_A |\mathbf{k_A}| = \upsilon_A |\mathbf{k_p} - \mathbf{k_s}| \approx 2\upsilon_A \mathbf{k_p} \sin(\theta/2) \tag{2.49}$$

where $\mathbf{k_A}, \mathbf{k_p}$ and $\mathbf{k_s}$ are the wave vectors of the acoustic, the pump and the Stokes waves, respectively. For the first equality, the momentum conservation is considered. Secondly, we use $|\mathbf{k_p}| \approx |\mathbf{k_s}|$. Then, the Brillouin shift reaches the maximum value for the counter-propagating direction and it vanishes for the co-propagating direction.

Other difference is relative with the gain spectrums. In contrast with SRS, the Brillouin-gain spectrum is narrow (on the order of tens of MHz) and g_B is maximum for a shift of approximately 10 GHz [64].

As we previously point out, another feature of SRS and SBS is that they only occur when the pump power exceeds a threshold. This threshold is also different for Brillouin and Raman. It can be calculated for long fiber distances ($L >> 1/\alpha$) by [65],

$$\begin{aligned} I_R^{th} &\approx 16 \frac{\alpha}{g_R} \\ I_B^{th} &\approx 21 \frac{\alpha}{g_B} \end{aligned} \tag{2.50}$$

In practice, SRS arises for pump powers around 1 W and SBS for pump powers of 10 mW in standard SMF at the typical wavelengths for optical communications.

Due to the gain spectrum differences, SRS is more used in amplification systems, whereas sensor applications take advantages of SBS. In the next section, we explain the different kind of amplifiers.

2.4 Amplification systems

As we have seen above, signals propagating through an optical fiber suffer mainly from three limiting factors: attenuation, dispersion and nonlinear effects. All three problems increase as the fiber length increases, and consequently, the use of mitigation techniques is required for optical fiber systems to be able to operate at long transmission distances.

Of the three, the distortion caused by nonlinear effects is the hardest to compensate from a fundamental point of view, and although techniques such as optical phase conjugation [66] have been applied successfully, they present technological challenges and have limited application. Still, the negative impact of nonlinear effects can usually be managed by keeping signal powers under constraint.

Chromatic dispersion can be periodically compensated through the use of dispersion compensating optical fiber with dispersion of the opposite sign to that of the transmission fiber, or through the introduction of lumped dispersion compensating elements such as chirped fiber Bragg gratings.

Attenuation, on the other hand, requires some form of amplification, and this, on itself, introduces yet another undesirable but also unavoidable element: noise. In the early ages of optical fiber communication, optical signals were converted to electrical signals, regenerated, converted again to the optical domain and re-launched into the fiber. This solution was expensive and complex for wavelength-division multiplexed (WDM) lightwave systems, and the speed of the electronics introduced a cap in the maximum bit-rate of the system. In the 90's the possibility of using all-optical amplification become a reality with the advent of semiconductor optical amplifiers (SOAs) [67], and later doped fiber Amplifiers (DFAs) [8] and nonlinear amplifiers such as distributed Raman amplifiers (DRAs), distributed Brillouin

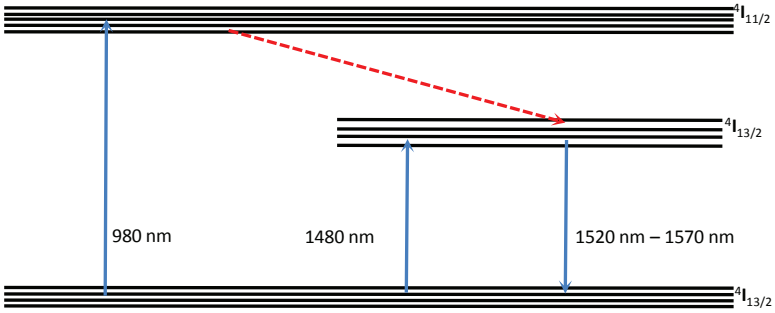

Figure 2.5: Energy-level diagram of erbium ions in silica fibers.

amplifiers (DBAs) and parametric amplifiers (PAs).

Doped-fiber and nonlinear-effect based amplifiers will be dealt with in more detail below. As for semiconductor optical amplifiers (SOAs), they include a semiconductor (InP, GaInAsP...) as active medium inside a Fabry-Perot cavity with anti-reflection elements at the endfaces [68]. SOAs are usually less expensive than other optical amplifiers, because its small size and they are electrically pumped. Another advantage is the possible integration of the SOA with the receiver. However, performance-wise they present some important disadvantages: high noise, low gain, moderate polarization dependence and interchannel crosstalk due to high nonlinearities and large coupling losses. For these reasons, SOAs have limited application as the main source of amplification in long-haul optical communication schemes, although they have proven very useful in the development of compact and integrated photonic devices.

The most commonly used optical amplifiers make use of optical fibers doped with rare-earth elements as their gain medium. A rare-earth doped amplifier is basically, a small span of silica fiber that has been doped by one rare-earth element, introducing a transition that can be exploited to transfer energy from a pump to a fixed range of frequencies. Hence, a pump

laser excites the doping ions to a higher energy level. Decay from this excited states can be made very efficient by stimulated emission of photons at the signal wavelength. The operating wavelengths and the gain bandwidths are determined by the energy-level diagram of the dopant element. Erbium-doped fiber amplifiers (EDFAs) are specially attractive in optical communications, since Erbium has emission in the optical C-band typically used in telecommunication applications (centred around 1.55μm) [69] and part of the L-Band (around 1.59μm). The energy-level diagram of Erbium and the spectrum of a typical EDFA are shown in figures 2.5 and 2.6, respectively. The pumping wavelengths for EDFAs are 980 nm and 1480 nm. Efficiencies as high as 11 dB/mW were achieved in early EDFAs with 0.98μm pumping [70], and have improved notably since then. Apart from the pumping wavelength, a large number of parameters affect the EDFA gain, such as erbium-ion concentration, core radius, amplifier length and pump power. The main source of impairment in EDFAs is amplified spontaneous emission (ASE). Some of the electrons in the upper energy level can decay by spontaneous emission and the emitted photons interact with other dopant ions to be amplified by stimulated emission. The ASE power spectral density is written as [71],

$$S_{ASE} = (G-1)h\upsilon n_{sp} \tag{2.51}$$

where h is the Planck's constant, υ is the energy of the photon, G is the gain and n_{sp} is the spontaneous emission factor defined as,

$$n_{sp} = \frac{\eta N_2}{\eta N_2 - N_1} \tag{2.52}$$

N_2 and N_1 are the electron densities in the ground and the excited state,

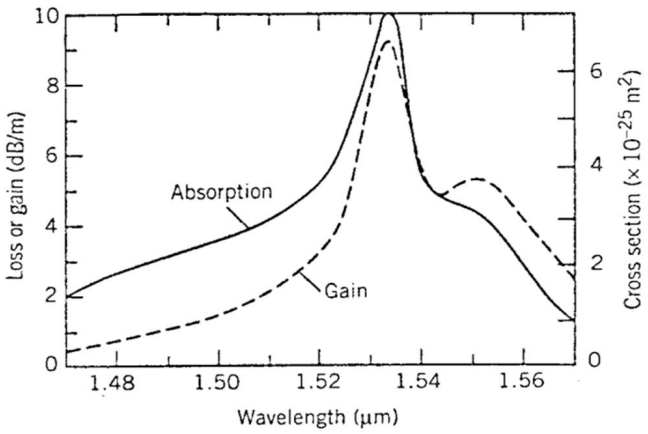

Figure 2.6: Absorption and gain spectra of an EDFA. After [1, 72].

respectively and η has information of the cross sections for the spontaneous emission and the absorption processes. The minimum value of n_{sp} is 1, reached when the total population inversion is produced ($N_1 \approx 0$).

Given the high cost of doped fibers and their high conversion efficiency, doped fibers are not adequate for transmission, but are perfectly suited to be used as lumped amplifier elements that are periodically inserted into the transmission line to boost the depleted optical signal back to high intensity levels. Of course, this process introduces ASE noise, and if the intensity of the transmitted signal is allowed to drop too much before amplification, the introduced ASE will seriously degrade the optical signal-to-noise ratio. This means that a balance must be found between keeping signal intensity from being too low, which leads to noise limited transmission, and using a too high intensity, which leads to nonlinear-distortion limited transmission. An optimal solution would be to reduce the spacing between amplifiers, so power could be kept at a close-to-constant optimal level, but this would be too costly to achieve with doped fibers.

Fortunately, the use of doping ions is not the only way to achieve energy

conversion from a pump to the signal wavelength. As we have seen in the nonlinear effects section above, inelastic scatterings and four wave mixing can achieve a similar effect, albeit not as efficiently. Still, nonlinear-effect based amplifiers can exploit the whole length of the transmission fiber instead of a few meters, and so the levels of efficiency of an EDFA are not required to achieve signal amplification. Within the whole family of nonlinear amplifiers, Raman amplifiers are the most popular thanks to their remarkable features, which are described in detail in the next section.

2.5 Raman amplification

Raman amplifiers exploit SRS, as previously explained, to transfer energy from a pump source to a signal at the corresponding Stokes wavelength. In this process, the two optical beams are launched into the fiber. The pump photons are absorbed by the molecules of the material, which get excited into a virtual state, and then emitted at a longer wavelength (lower energy) while part of the energy is stored in the molecule in the form of excited vibrational levels (phonons). The effectiveness of the process is determined by the profile of the Raman gain (see figure 2.4) and parameters such as the attenuation of the fiber at both the pump and its Stokes wavelength. The Raman gain curve for Silica spans over 40 THz with a gain peak obtained for a shift of approximately 13.2 THz. At typical telecommunication wavelengths, this corresponds to about 100 nm.

From the physics of SRS, some of the advantages of Raman amplifiers are obvious. The first advantage with respect to EDFAs comes from the fact that SRS can take place in any optical material, and hence in standard fibers, without the need for any additional doping. This allows us to use the same fiber to transmit the signal and compensate the attenuation

losses over kilometric distances with a relative low cost. Secondly, Raman gain is available at any wavelength for which a suitable pump source can be found, while EDFAs are limited to operate in the C and L bands. Systems with Raman amplification are useful over the entire transparency region of fibers, the only requirement to amplify a desired wavelength being the correct selection of the pump wavelength and careful management of the interactions between pumps in a multi-wavelength pump setup. The possibility of combining several pumps to cover a broad bandwidth is on itself a third advantage. Moreover, gain flatness over very broad bandwidths (in excess of 100 nm) can be achieved by optimizing the relative contribution from each pump [73]. The pumps themselves can be spectrally broadened to reduce the number of required sources to achieve a certain level of flatness [74]. Finally, and perhaps more importantly, Raman amplifiers present a reduced ASE noise build-up than EDFAs and other lumped optical amplifiers. Raman amplifiers are always a fully inverted system, that is the population of the second level (N_2) is much higher than the population of the lower level (N_1). Furthermore, as they can also operate in a distributed manner the signal is kept from dropping too low and reduces accumulation of ASE noise.

Despite their potential, Raman amplifiers were not developed until the late 1990s. The main problem was the high power required from the pumps, which were on the order of 1 W, as opposed to the case of EDFAs, where a few milliwatts would suffice. This problem was sorted out by the development of high power Raman fiber lasers. While Raman fiber lasers have allowed for a rapid expansion of Raman amplification, they are still far from ideal pump sources, as they are inherently afflicted from relative-intensity noise which, as we will see, can be transferred to the signal.

Equation 2.49, including the attenuation losses, can be solved to determine the evolution of the average pump and signal power inside the fiber. In general, pump depletion (pump losses due to SRS) can be neglected when pump power is more than three orders higher than signal power. Assuming that signal and pump are co-propagating, the value of the signal intensity at any point is,

$$I_S(z) = I_S(0)\exp(g_R I_P(0) L_{eff} - \alpha_S L) \tag{2.53}$$

where L_{eff} is dependent on α_P. From here, the Raman gain in the unsaturated regime is:

$$G_R(z) = \frac{I_S(L)^{(Raman)}}{I_S(L)} = \exp(g_R I_P(0) L_{eff}) \tag{2.54}$$

It is worth noting that for long distances, the effective interaction length can be found to be equal to L_{eff}, whose value for SMF is capped at approximately 20 km [2]. In order to know the Raman gain in saturated regime, we solve numerically the complete set of equation including pump depletion [75],

$$G_{R,sat} = \frac{1 + r_0}{r_0 + G_R^{-(1+r_0)}} \tag{2.55}$$

where $r_0 = \omega_p/\omega_s P_s(0)/P_p(0)$. Because of the values of P_p, the saturation power in Raman amplifiers is much larger compared with other amplifiers.

Those equations have been obtained for a pump co-propagating with the signal. Similar equations describe the gain when the pump and signal are counter-propagating. In the following section we will show the general model

for a bi-directionally pumped system with ASE and Rayleigh scattering components.

2.5.1 Configurations

In terms of its architecture, there are three basic configurations for a single-Stokes Raman amplifier, depending on the pumping point of choice. To illustrate the particularities of each scheme, we have simulated a 100 Km amplified link with a total pump power of 645 mW and input signal power of 0.1 mW. The evolution of the power of its different spectral components is shown in figure 2.7 for each of the three configurations.

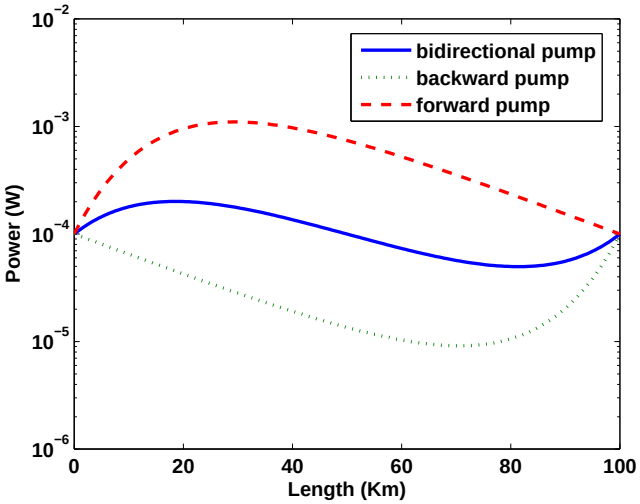

Figure 2.7: Theoretical signal evolution in a transmission fiber for different pumping configurations.

The most intuitive case is the forward-pumping configuration. Here amplification is obtained in the first kilometers of fiber and, initially, the signal is over-amplified to compensate for the attenuation that it will suffer beyond the effective gain length. In the example, the signal reaches the maximum value at 28 km (ten times the initial value). Due to this, this kind of con-

figuration is bound to be more prone to nonlinear distortion. On the other hand, the contribution of the noise (Rayleigh and ASE) is slightly lower. Considering an initial signal-to-noise ratio equal to 20 dB and a bandwidth of the noise equal to 125 GHz, the degradation is less than 0.3 dB.

Another possibility would be to launch the pump from the receiver end, so it counter-propagates with the signal. Now the signal power is kept low, since amplification takes place mainly in the last kilometers of fiber. Nonlinear effects are avoided but noise is higher (the degradation is approximately 3 dB in the simulation).

Finally, bidirectional pumping combines the advantages of the other two configurations as amplification is more evenly distributed, and takes place all along the fiber. In our simulation, the noise degradation is approximately 0.8 dB.

Other, more complex configurations, include pumping at various wavelengths for increased bandwidth or second order (cascading) pumping. We will see more of the second case later.

A complete mathematical description of the bidirectional pumping scheme including ASE and double backscattering Rayleigh (DBR) for the evolution of the average powers (P_j) and the noises (n_s) can be written as,

$$\frac{dP_p^{\pm}}{dz} = \mp\alpha_p P_p^{\pm} \mp \frac{\upsilon_p}{\upsilon_s}\frac{g}{A_{eff}}(P_s + n_s^+ + n_s^- + 2h\upsilon_s\Delta\upsilon_s(1 + \frac{1}{e^{\frac{h(\upsilon_p-\upsilon_s)}{K_BT}}-1}))P_p^{\pm} \pm \epsilon_p P_p^{\mp} \tag{2.56}$$

$$\frac{dP_s}{dz} = -\alpha_s P_s + \frac{g}{A_{eff}}(P_p^+ + P_p^-)P_s \tag{2.57}$$

$$\frac{dn_s^+}{dz} = -\alpha_s n^+ + \frac{g}{A_{eff}}(P_p^+ + P_p^-)(n^+ + h\upsilon_s\Delta\upsilon_s (1 + \frac{1}{e^{\frac{h(\upsilon_p-\upsilon_s)}{K_BT}}-1})) + \epsilon_s n^- \tag{2.58}$$

$$\frac{dn^-}{dz} = \alpha_s n^- - \frac{g}{A_{eff}}(P_p^+ + P_p^-)(n^- + h\upsilon_s \Delta\upsilon_s \\ (1 + \frac{1}{e^{\frac{h(\upsilon_p - \upsilon_s)}{K_B T}} - 1})) - \epsilon_s(P_s + n^+) \tag{2.59}$$

where h is is Plank's constant, K_B is Boltzmann's constant, T is the absolute temperature of the fiber. The (+) and (-) superscripts represent forward and backward propagation and p and s subscripts identify the pump and signal. The υ_i are the corresponding frequencies of the pumps and signal and $\Delta\upsilon_s$ represents the effective bandwidth. In the next section, the main impairments included in this model are briefly explained.

2.5.2 Sources of noise

There are three main sources of noise in Raman amplifiers. The first is the DRBS, caused by two scattering events (one backward and the other forward) [76] affecting a signal photon. DBRS noise is particularly problematic, as Rayleigh scattering is an elastic and random process, which means that DRBS carries no information, but follows the exact same spectrum as the signal. While the efficiency of the double backscattering process is very low in non-amplified fibers, in a distributed amplifier the scattered photons make a double pass through the gain medium, which can greatly increase efficiency. In Raman amplifiers, this noise is dependent on length and the total gain and can be on occasion the main source of signal degradation.

The second source is the usual ASE. This is the main source of noise in EDFA-amplified systems, and even though its contribution is lower in distributed Raman amplifiers, it remains important. The ASE noise advantage of Raman amplifiers is typically exploited to achieve longer spacings between pumps, reducing costs.

The last relevant source of noise is the RIN transfer from the pump power

to the signal. RIN describes the instability in the power level of an optical signal. In systems based on Raman amplification, the RIN of the pump lasers can be transferred to the signal. Due to the fast gain dynamics of the Raman effect, this transfer is a potentially important source of impairment for these amplification systems [77]. RIN transfer in ultralong lasers, focusing mainly on the novel case of random distributed feedback lasers, is studied in chapter 3.

To conclude, another important feature of Raman amplification is its dependency on the state of the polarization of the pump and signal. If the pump and signal states of polarization are parallel, the gain is maximum. This characteristic is extended in chapter 5.

2.5.3 Ultra-long Raman lasers

In higher order Raman pumping schemes or cascade Raman lasers, more than two signals at different wavelengths interact. Some schemes use several pumps separated by the Stokes frequency shift and the higher frequency pumps are used to amplify the lower frequency pumps, with the lowest frequency pump amplifying the transmitted signal. This configurations produce a more uniform amplification along a longer span of fiber, by pushing the effective gain length further away from the pumping point. Some examples of higher order Raman amplifiers have been presented in the last decade [78, 18].

An example of second order Raman amplifier is the ultra-long Raman fiber laser (URFL), proposed in 2004 [20] and experimentally demonstrated in 2006 [21]. This configuration, whose scheme is depicted in figure 2.8, was initially proposed used to amplify a signal in the vicinities of 1550 nm. This device consists of a cavity delimited by two fiber Bragg grating reflectors

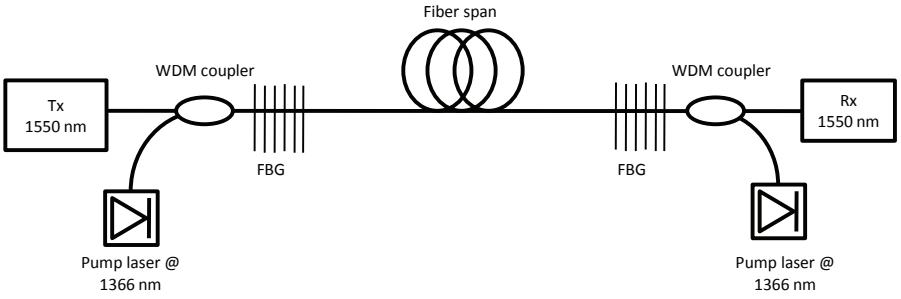

Figure 2.8: Schematic description of the URFL.

(FBGs) resonant at 1455 nm wavelength. A 1366 nm pump is launched from the both ends of the transmission span and, by Raman scattering, a 1455 nm secondary pump is created and confined inside the cavity. This secondary pump is the one that provides amplification to the 1550 nm input signal.

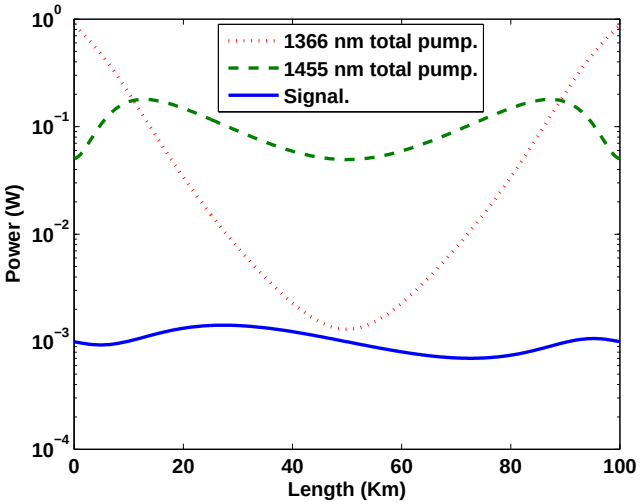

Figure 2.9: Evolution of the signal and total pumps in a URFL.

As can be seen in figure 2.9, the first Stokes signal (1455 nm) is very efficiently distributed over the total length. Hence, the gain provided to

the 1550 nm signal is almost uniform and signal excursion is very small. Moreover, noise degradation is also very low for 100 km. Another important feature of this configuration is that, due to the natural bandwidth of the Raman gain profile, and the superposition of the Raman gain curves of the 1366 nm and 1455 nm pumps, the system can provide flat gain over a 20 nm bandwidth for WDM communications [22]. This has been used to achieve simultaneous spatio-spectral transparency over 20 nm and 20 km [79].

The complete mathematical model for the evolution of the signals in this configuration is described in [20] and reproduced below,

$$\frac{dP_{p1}^{\pm}}{dz} = \mp\alpha_{p1}P_{p1}^{\pm} \mp \frac{\upsilon_{p1}}{\upsilon_{p2}}\frac{g_1}{A_{eff}}(P_{p2}^{+} + P_{p2}^{-} \tag{2.60}$$
$$+2h\upsilon_{p2}\Delta\upsilon_{p2}(1 + \frac{1}{e^{\frac{h(\upsilon_{p1}-\upsilon_{p2})}{K_BT}}-1}))P_{p1}^{\pm} \pm \epsilon_{p1}P_{p1}^{\mp}$$
$$\frac{dP_{p2}^{\pm}}{dz} = \mp\alpha_{p2}P_{p2}^{\pm} \mp \frac{\upsilon_{p2}}{\upsilon_{s}}\frac{g_2}{A_{eff}}(P_s + n_s^{+} + n_s^{-} \tag{2.61}$$
$$+2h\upsilon_{s}\Delta\upsilon_{s}(1 + \frac{1}{e^{\frac{h(\upsilon_{p2}-\upsilon_{s})}{K_BT}}-1}))P_{p2}^{\pm} \pm \frac{g1}{A_{eff}}(P_{p1}^{+} + P_{p1}^{-})P_{p2} \pm \epsilon_{p1}P_{p1}^{\mp}$$
$$\frac{dP_s}{dz} = -\alpha_s P_s + \frac{g}{A_{eff}}(P_{p2}^{+} + P_{p2}^{-})P_s \tag{2.62}$$

where sub-index 1 and 2 has been chosen to distinguish the primary pump and the generated pump, respectively. Equation for the evolution of the noise have not changed. Note that the boundary conditions for the secondary pump are that $P_{p2}^{+}(0) = R \cdot P_{p2}^{-}(0)$ and $P_{p2}^{-}(L) = R \cdot P_{p2}^{+}(L)$.

Since their inception, URFLs have found a large number of applications, including long distance communications [80], classical soliton transmission over tens of soliton periods [81], extremely flat supercontinuum generation in conventional fibers [82], improving of the sensitivity and measurement range of distributed sensors [25], and many others.

2.5.4 Random distributed feedback Raman lasers

An important issue in the analysis of ultralong Raman fiber laser is the physical mechanisms that restrict the boundless increase of a fiber laser cavity length. Increasing the fiber length leads to new physical phenomena underlying the light generation regimes. In particular, the huge number of longitudinal modes present in an ultralong laser cavity weakly interacting between them via four-wave mixing, produces interesting properties that resemble the random behavior associated with the so called weak wave turbulence [83]. If this weak interaction were the main cause for the broadening of the cavity modes, one could expect to see a resolvable mode structure for cavities of up to 1000 km [84], provided power in the laser is kept very low. However, there is another physical mechanism that limits cavity length: distributed Rayleigh backscattering. From the full model from the previous section, it can be calculated that, for a long enough cavity, most of the photons propagating through the fiber are not being back reflected at the fiber Bragg gratings, but have instead been randomly Rayleigh backscattered by the medium molecules before traversing the whole cavity. Specifically, at a threshold length of about 270 km for standard fiber, longitudinal cavity modes become blurred, and the laser can be assumed to present instead multiple effective resonators of randomly varying length due to this backscattering [85].

Random distributed feedback Raman lasers (RDFL) are a particular case of URFLs that take advantage of distributed Rayleigh backscattering to remove the external mirror [26]. In figure 2.10, we present the scheme of a typical random laser used to amplify optical signals at 1550 nm. The 1366 nm-wavelength pumps are launched from the central point. The process to generate the first Stokes signal is identical to the process in other

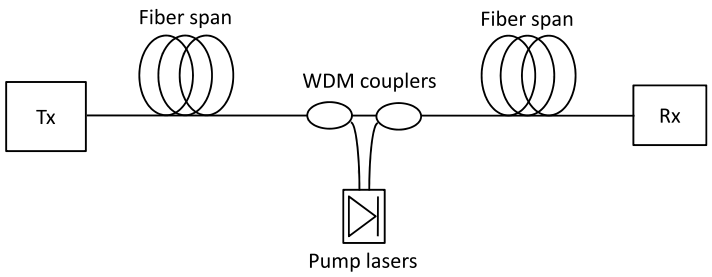

Figure 2.10: Schematic description of the RDFL.

Raman lasers but, as there are no mirrors, the feedback is mainly produced by Rayleigh backscattering. As we mentioned before, Rayleigh scattering occurs in all directions, but only a small part ($< 0.1\%$) of the radiation is scattered back into the core of the fiber. In the vicinities of the pumping point, the process is made dramatically more efficient due to amplification of the scattered light.

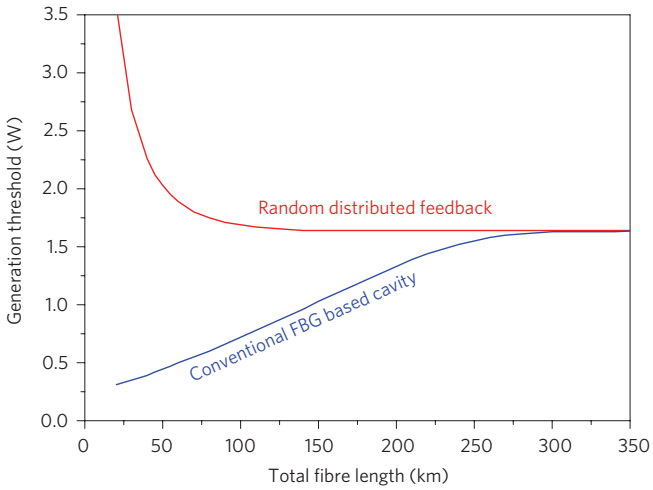

Figure 2.11: Numerical comparison of the lasing threshold for URFL and DRFL. The pump wavelength is 1455nn and the lasing wavelength is 1550nm. From [26].

A comparison between URFL and RDFL in terms of pump power threshold versus length is shown in figure 2.11. While the generation threshold in URFL increases with the cavity length, the threshold tends to a constant value in RDFL. For long fibers, the threshold is identical in both configurations because the feedback effect of Rayleigh backscattering is higher than the effect of mirrors (i.e. any long-enough cavity laser becomes a random distributed feedback laser).

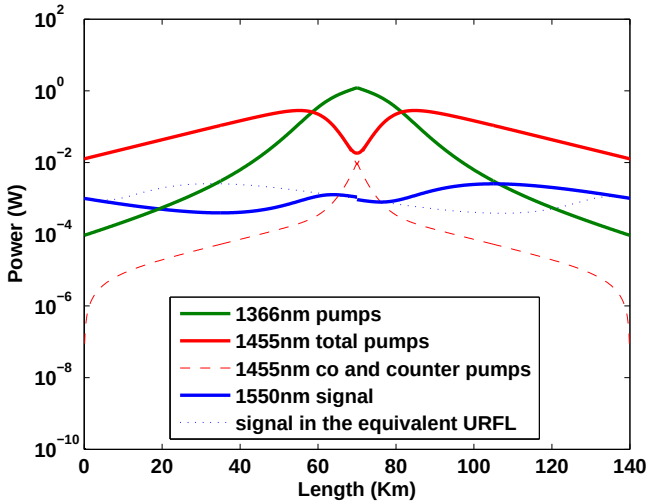

Figure 2.12: Evolution of the power signals for the RDFL configurations with L=140Km and the required power pump to compensate all the attenuation losses. To enable comparison, the evolution of the 1550nm in URFL is included.

RDFLs present similar characteristics to other random lasers, but in contrast to classical random lasers, RDFLs deliver well-confined stable laser radiation in a narrow bandwidth similar to conventional lasers.

The first application reported for RDFLs was their use for remote sensing with FBGs [86], but they have also been used to provide amplification in ultra-long communication links [87], as well as to achieve multi-wavelength lasing [88]. Its use for providing amplification has been simulated and in

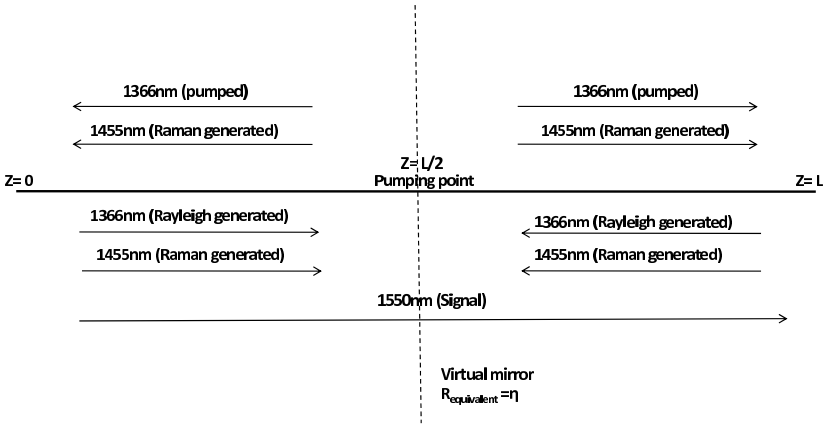

Figure 2.13: Scheme of all signals in RDFL.

figure 2.12, the evolution of the pump and signal power is described for a 140 km length RDFL. The power of the first Stokes signal is enough to compensate losses at 1550 nm in the fiber. The excursion of the 1550 nm signal is similar to that observed in a cavity URFL.

To model this configuration, we solve the set of equations 2.60-2.62 from z=0 to z=L/2 taking advantage of the symmetry of a centrally-pumped RDFL. We consider a virtual mirror at z=L/2 and the boundary conditions are:

$$P_{p1}^{+}(0) = 0;\ P_{p2}^{+}(0) = 0;\ P_{s}^{+}(0) = P_{s,in}$$

$$P_{p1}^{-}(L/2) = P_{p,in} + \eta \cdot P_{p1}^{+}(L/2);\ P_{p2}^{-}(L/2) = \eta \cdot P_{p2}^{+}(L/2)$$

where $P_{s,in}$ and $P_{s,in}$ are the initial signal power and initial pump power and η is the efficiency of the connection (1 for the ideal case). The solution for the range from L/2 to L, is totally symmetric when there is no signal ($P_{s,in} = 0$):

$$P_{p1}^{+}(0 : L/2) = P_{p1}^{-}(L : L/2);\ P_{p2}^{+}(0 : L/2) = P_{p2}^{-}(L : L/2)$$

$$P_{p1}^{-}(L/2 : 0) = P_{p1}^{+}(L/2 : L);\ P_{p2}^{-}(L/2 : 0) = P_{p2}^{+}(L/2 : L)$$

When RDFL are used for amplify transmitted signal, the signal and noises are not symmetric. For this reason, we again solve the set of equations from z=L/2 to z=L using the values at z = L/2 previously calculated as initial conditions. Figure 2.13 includes all the signals of interest in order to understand the symmetry of the configuration.

Chapter 3

RIN transfer in ultra-long Raman lasers

In this chapter, the relative intensity noise (RIN) transfer from the pump sources to lower Stokes in ultra-long Raman lasers, including both cavity-based and random distributed feedback lasers, is analysed. Previous studies on RIN transfer have focused on the RIN transfer from the pumps to the output laser component in standard (not ultralong) Raman fiber lasers [89] or the RIN transfer from the primary pumps to the amplified signal in cavity ultra-long fiber laser amplification schemes [90]. Here, for the first time, we present the analysis of RIN transfer in random distributed feedback lasers (RDFLs) configurations, as well as offer a comparison between the impact of this impairment in RDFLs and cavity ultra-long Raman fiber lasers (URFLs). This is particularly relevant when considering each of the two ultralong laser option for amplification in areas such as distributed sensing, where the relatively long duration of the pulses (of the order of tens of ns) makes them particularly vulnerable to the impact of RIN.

The complexity of studying the transfer of amplitude fluctuations in

higher-order cascaded amplification schemes, such as ultralong Raman fiber lasers, makes it necessary to rely on a numerical approach, since the system of equations governing the noise exchange is not directly integrable. To develop a mathematically accurate model for the description of RIN transfer, we begin from the well known set of ordinary differential equations (ODE) describing the evolution of the average powers of all the spectral components, used widely in our numerical analysis of URFLs and RDFLs [20]. This set must be extended with a set of equations containing information on the evolution of the average level of the fluctuations in signal power due to RIN. The complete system is numerically solved for fluctuations of frequency ranging from a few Hz to beyond 10 MHz. The results are grouped in two sections. In section 3.2, our interest is on the RIN transfer from the pumps to the first Stokes signal while section 3.3 shows the RIN transfer from the pumps to the transmitted signal.

3.1 Introduction

RIN describes the instability in the output power of a laser or, in other words, its intensity fluctuations. These fluctuations can be produced by many causes, such as small variations in the gain medium or the cavity length of the pump laser, or the dependence of gain on a randomly varying polarization, to name a few. Polarization dependent-gain (PDG) as a source of RIN will be explored in some more detail on chapter 5. Here, our interest is not in the origin of the intensity fluctuations in the pump source, but on how these fluctuations get transferred from the pump lasers to the amplified signals.

The fast response time of the Raman effect makes it possible for slow intensity fluctuations in pump power to transfer into variations of the gain

and, consequently, into amplitude fluctuations of the amplified continuous or modulated the signal. When signal and pump are propagating in the same direction, the nonlinear interaction between them is limited only by the attenuation they suffer and the transmission delay between the two different spectral components caused by group velocity dispersion. This relative delay effect is known as temporal walk-off and produces an averaging of the noise caused by fast intensity fluctuations, limiting the efficient transfer of RIN to a limit frequency of about 10 MHz or less. In the counter-propagating case, the overlapping time of signal and pump is much smaller and, consequently the averaging out of the fluctuations takes place for lower cut-off frequencies. Here, the cut-off frequency (also referred to as corner frequency or 3-dB frequency) is defined as the frequency at which RIN transfer is 3dB lower than the RIN transfer at a frequency equal to 0.

To model the RIN transfer process, our analysis is based on the RIN transfer analysis in first order Raman amplification scheme found in [77, 91, 92]. We consider the pump power is dependent on z and t as $P_p(t,z) = \overline{P}_p(z) + \triangle P_p(z,t)$, with a constant average power part, $\overline{P}_p$, and a fluctuating part depending on time, $\triangle P(t)$. We assume that the spectral density of the fluctuating part $\triangle P_p(z,t)$ may be written as

$$\frac{dN_p^{\pm}}{dz} + i\beta_p^{\pm}\omega N_p^{\pm} = \mp\alpha_p N_p^{\pm} \mp \frac{\upsilon_p}{\upsilon_s} g N_s P_p^{\pm} \mp \frac{\upsilon_p}{\upsilon_s} g P s N_p^{\pm} \pm \epsilon_p N_p^{\mp} \qquad (3.1)$$

$$\frac{dN_s}{dz} = -\alpha_s N_s + g(N_p^{+} + N_p^{-})P_s + g(P_p^{+} + P_p^{-})N_s \qquad (3.2)$$

Taking the group velocity of the signal (V_p) as the reference velocity, the walk-off constant of the pump is $\beta_p^{\pm} = \frac{1}{V_p} \mp \frac{1}{V_s}$. Simplifying $\beta^{+} = D(\lambda_s - \lambda_p)$ and $\beta^{-} \approx 2/V_s$ where D is the chromatic dispersion. The normalized RIN

in the linear scale is defined as

$$RIN = \frac{|N_i|}{\overline{P}_i} \tag{3.3}$$

where the subindex i represents p or s for pump and signal, respectively. And the RIN transfer function is defined as,

$$H = \frac{RIN_{signal}}{RIN_{pump}} \tag{3.4}$$

Note that the RIN transfer function provides a relative measure of the amount of RIN transferred from the pump to the signal. As such, it turns out to be independent of the initial value of the RIN set to the pump. This means that, knowing the value of the RIN noise of the pump at a given frequency, we will be able to infer the value of the RIN at the same frequency in the output signal.

In the case of first order Raman amplification and for long fibers, the RIN transfer function has the form of a low-pass filter with a -3dB frequency equal to $f_c^{\pm} = \frac{\alpha_p}{2\pi\beta^{\pm}}$. In the counterpropagating configuration, attenuation is the dominant factor that defines the cut-off frequency. For standard fibers, the cut-off frequency is close to 1 kilohertz at wavelengths close to 1500 nm. In the co-propagating configuration, the cut-off frequency is mainly dependent on the dispersion. Therefore, the cut-off frequency in standard fiber is close to 10 MHz but is increasing as the used wavelengths are close to zero dispersion wavelength. For very short lengths of fiber or very low loss, dips will arise on the RIN transfer function for frequencies higher than the corner frequency. Note the differences between short length and long length in the RIN transfer in figure 3.1.

To extend this analysis to the cases of URFL and RDFL, a three level

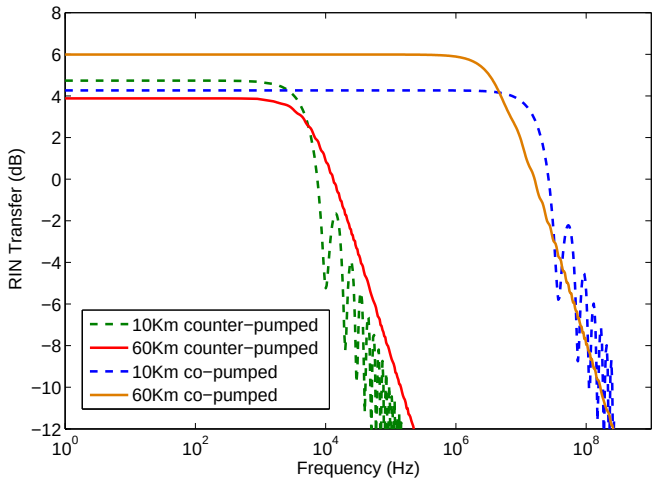

Figure 3.1: RIN transfer for co-pumped and counter-pumped amplification schemes. The results are obtained for two fiber length: 10 km and 60 km. The gain is always equal to 8.3 dB

set of ODEs is necesary,

$$\frac{dN_{p1}^{\pm}}{dz} + i\beta_{p1}^{\pm}\omega N_{p1}^{\pm} = \mp\alpha_{p1}N_{p1}^{\pm} \mp \frac{\upsilon_{p1}}{\upsilon_{p2}}g_1(N_{p2}^{+} + N_{p2}^{-})P_{p1}^{\pm} \tag{3.5}$$
$$\mp\frac{\upsilon_{p1}}{\upsilon_{p2}}g_1(P_{p2}^{+} + P_{p2}^{-})N_{p1}^{\pm} \pm \epsilon_{p1}N_{p1}^{\mp}$$
$$\frac{dN_{p2}^{\pm}}{dz} + i\beta_{p2}^{\pm}\omega N_{p2}^{\pm} = \mp\alpha_{p2}N_{p2}^{\pm} \mp \frac{\upsilon_{p2}}{\upsilon_{s}}g_2N_sP_{p2}^{\pm} \mp \frac{\upsilon_{p2}}{\upsilon_{s}}g_2P_sN_{p2}^{\pm} \tag{3.6}$$
$$\pm g_1(N_{p1}^{+} + N_{p1}^{-})P_{p2}^{\pm} \pm g_1(P_{p1}^{+} + P_{p1}^{-})N_{p2}^{\pm} \pm \epsilon_{p2}N_{p2}^{\mp}$$
$$\frac{dN_s}{dz} = -\alpha_sN_s + g_2(N_p^{+} + N_p^{-})P_s + g_2(P_p^{+} + P_p^{-})N_s \tag{3.7}$$

In the case of a typical URFL, the pump is launched from both sides. We consider that the RIN in the backward and the forward pump laser are identical, and evenly distributed between the real and imaginary part (although this choice will have no bearing on the final results). The generated first Stokes signal is reflected by the FBG at both ends. Consequently, the initial RIN of the copropagating signal is equal to the RIN of the counterpropagating signal at z=0 and viceversa at z=L. At the second Stokes

level, corresponding in a quasi-lossless transmission setup with the 1550 nm component, we suppose an initially RIN-free signal, so all the output RIN at this wavelength comes from RIN transfer. The initial conditions are

$$Re(N_{p1}^{+}(0)) = Im(N_{p1}^{+}(0)) = Re(N_{p1}^{-}(L)) = Im(N_{p1}^{-}(L)) = \frac{\sqrt{2}N_0}{P_T}$$

$$Re(N_{p2}^{+}(0)) = R \cdot Re(N_{p2}^{-}(0)) \quad Im(N_{p2}^{+}(0)) = R \cdot Im(N_{p2}^{-}(0))$$

$$Re(N_{p2}^{-}(L)) = R \cdot Re(N_{p2}^{+}(L)) \quad Im(N_{p2}^{-}(L)) = R \cdot Im(N_{p2}^{+}(L))$$

$$Re(N_s(0)) = Im(N_s(0)) = 0$$

where N_0 is the RIN of a pump laser, P_T is the total pump power and R is the reflectivity of the FBG.

The mirrorless case is slightly more complex due to the fact that the pump is typically injected from the center of the laser into both directions. Note that the problem is divided in two symmetric sections. Hence, it is only necessary to solve the set of equations between 0 and L/2 (See figure 2.13 to clarify). At z=0, only the signal at the second Stokes level is launched, which we consider, as in the cavity URFL case, to be free of initial RIN. At z=L/2, the primary pump is launched and the symmetry of the problem allows for all the co-propagating Stokes to behave as if reflected into a counter-propagating signal with their associated RIN. Note that it is necessary to include another equation for the counter-propagating signal at the second Stokes level.

$$Re(N_{p1}^{+}(0)) = Im(N_{p1}^{+}(0)) = Re(N_{p2}^{+}(0)) = Im(N_{p2}^{+}(0)) = Re(N_s^{+}(0)) = Im(N_s^{+}(0)) = 0 \quad Re(N_{p1}^{-}(L/2)) = \frac{\sqrt{2}N_0}{P_T} + \eta \cdot Re(N_{p1}^{+}(L/2))$$

$$Im(N_{p1}^{-}(L/2)) = \frac{\sqrt{2}N_0}{P_T} + \eta \cdot Im(N_{p1}^{+}(L/2))$$

$$Re(N_{p2}^{-}(L/2)) = \eta \cdot Re(N_{p2}^{+}(L/2)) \quad Im(N_{p2}^{-}(L/2)) = \eta \cdot Im(N_{p2}^{+}(L/2))$$

$$Re(N_s^{-}(L/2)) = \eta \cdot Re(N_s^{+}(L/2)) \quad Im(N_s^{-}(L/2)) = \eta \cdot Im(N_s^{+}(L/2))$$

Here η means the effectiveness of the connection.

3.2 RIN Transfer from pumps to first Stokes

In this section, the RIN transfer between the pump and its first Stokes in an RDFL is analyzed. We consider that the wavelength of the primary pumps is 1455 nm in this case, for easiness in comparison with most of the existing literature on random distributed feedback fiber lasers, and consequently, the wavelength of the first Stokes signal is 1550 nm. The method and conclusions, though, are easily translatable to the case in which the primary pump is set at 1366 nm and the first Stokes at 1455 nm, as it would be required from second-order amplification schemes. In table 3.1, the main values of SMF for the wavelengths used in the simulation are summarized. The Raman gain from the pump to its first Stokes is 0.42 $W^{-1}km^{-1}$. the transmittance of the central connection in the RDFL is 0.85 in either direction.

λ (nm)	α (dB/km)	ϵ (m^{-1})	n
1455	0.263	6.0×10^{-8}	1.4996
1550	0.197	4.28×10^{-8}	1.5004

Table 3.1: Main parameters in the simulation.

Our analysis begins with the study of the evolution of the RIN noise transfer function across the gain medium, for a Stokes signal propagating from the left to the right of the laser. This kind of spatial analysis is not a feature usually present in the published literature analyzing RIN performance in lasers, but it becomes relevant in ultralong structures, particularly if they are going to be used for distributed sensing, since sensitivity and sensing range will depend on the noise distribution along the line.

In the case of the RDFLs, given that the pumping beams are launched bi-directionally from a central point, the results show two well-differentiated sections from the standpoint of a Stokes component propagating from left

to right. In the first section, the Stokes signal is counter-propagating with the launched pump, with a small amount of co-propagating pump power being present due to Rayleigh backscattering. In the second section, past the mid-point at L/2, the Stokes signal is co-propagating with the launched pump, although a small amount of Rayleigh-backscattered pump-power is presented. Both cases are depicted in figure 3.2. As it was expected, the cutoff frequency for the counter-propagating case is 10 KHz while it is higher for the co-propagating case (approximately 80 MHz). On the other hand, the transfer figure remains almost uniform along the distance and, consequently, the amount of impairments imposed by RIN transfer to the local sensitivity in a distributed sensing scheme would be similarly uniform along the sensing line.

There is another special feature of this RIN transfer function, namely the appearance of small fluctuations in the spectrum after the value of the cutoff frequency for the counter-propagating case. Such fluctuations have been also observed on traditional Raman lasers [89] and they are caused by the interaction between the generated counter-propagating signals. Their separation (the frequency difference between oscillations) is equivalent to the resonant cavity frequency in traditional lasers, as it has been observed in the literature, whereas in the random laser it depends on the distance between the pump point and the observation point as: $f_c = 1/(2\pi L)$, where L is this distance. These oscillations have also a much smaller amplitude in the case of RDFLs, and are often non-observable in standard-fibre configurations, except for cavities longer than 80 km and total pump powers above 2.8 W.

In order to find the optimal configurations that could minimise noise transfer while still offering a meaningful performance in terms of amplification and output power, the most relevant parameters of our system were

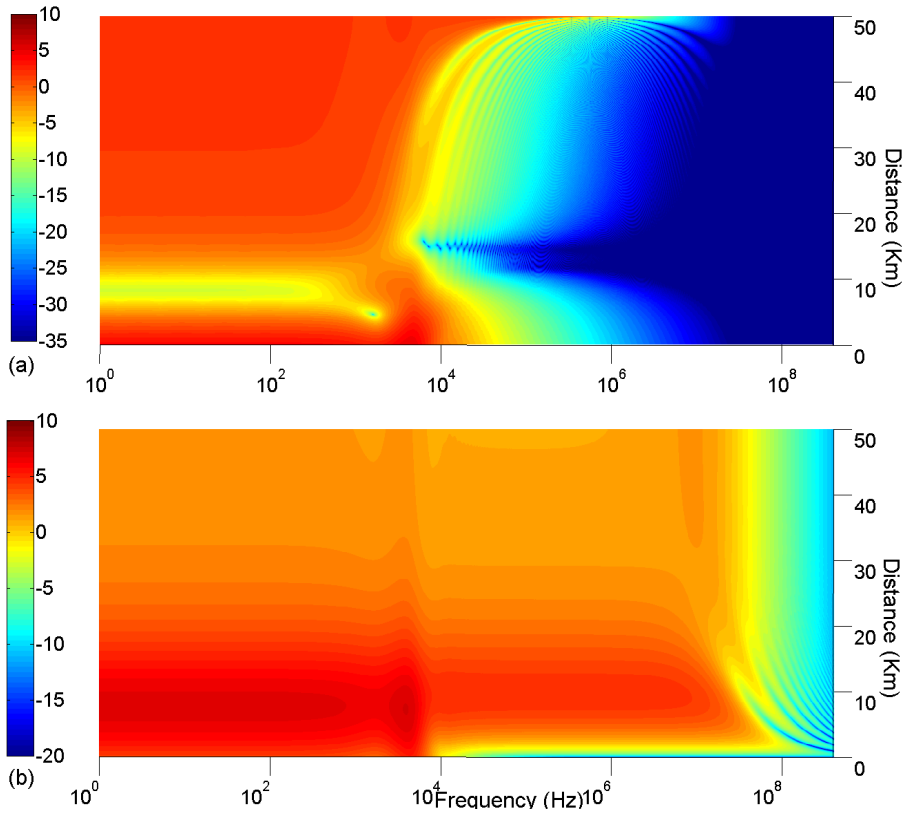

Figure 3.2: Evolution of the RIN transfer versus frequency along the fiber length for the situation where the amplification is mainly counter-propagated (top) or co-propagated (bottom). The total pump power is 3 W and the total length is 100 km.

varied over broad ranges, scanning the multi-dimensional parameter space. In figure 3.3 total pump power and total length have been varied between 2 and 3.8 W and between 30 and 200 km, respectively.

Note that the higher the total pump power launched, the less RIN is transferred. Nevertheless, increasing the total pump power beyond 3.8 W is not practical, since that is the threshold for the second Raman Stokes, which would cause a rapid depletion of the signal, as well as introduce in most cases an excess gain in the signal that would lead to nonlinear distortion. Note also that the cut-off frequency is slightly, but linearly, dependent on the pump

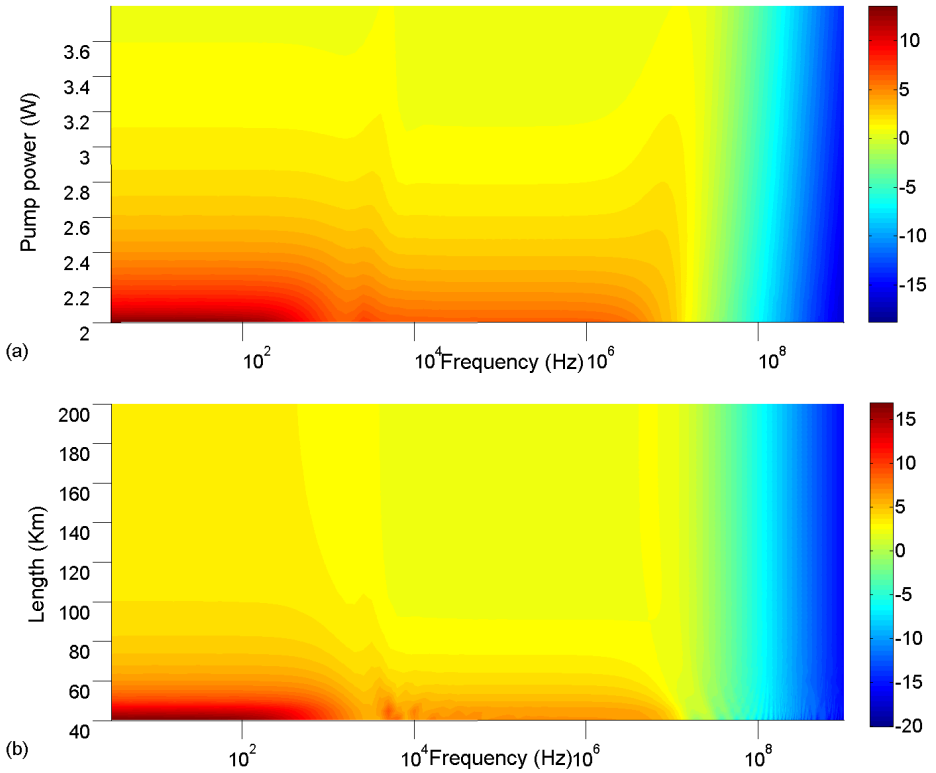

Figure 3.3: Variation of the RIN transfer vs. frequency with the total pump power (top) and the total length (bottom). In the first case, the total length is 100 km and, in the second case, the total pump power is 3W.

power. Finally, the most important source of impairment to be considered when the pump power increases is related with the fluctuation described previously: for total pump powers higher than 2.8 W the peak of maximum RIN transfer is reached in the oscillations taking place after the cut-off frequency (usually in one immediately after the first drop corresponding to the cut-off frequency for the counter-propagating component).

As can be seen in figure 3.3, the minimum RIN transfer is obtained for the longest laser. However, from our pump and signal power calculations we can observe that the peak output power is reached at 58 km length. The cut-off frequency itself is not affected by the fiber length. Regarding the

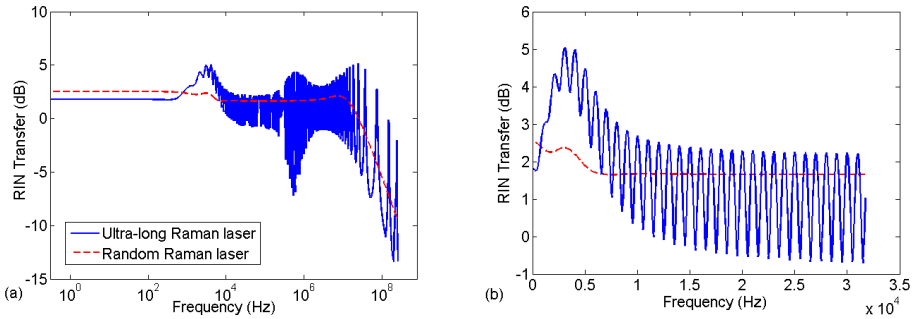

Figure 3.4: Comparative between the RIN transfer for the RDFL configuration and the traditional RFL in a logarithmic scale (left side) and a linear scale (right side).

oscillations, their separation decrease with length, and so will do their peak intensities.

Although this configuration is mirrorless, and so no reflector characteristics can be optimized, it is interesting to know if some control over RIN transfer can be achieved by using fibers with different Rayleigh scattering parameters. In this case, the maximum RIN transfer is inversely proportional to the Rayleigh scattering coefficient, as is output power. Generally speaking, the RIN transfer function is in most cases below 10 dB, comparable to those seen in distributed Raman amplification systems based on standard fiber operating at similar gain values and power levels.

Finally, a comparison between RDFL and an ultra-long cavity Raman laser pumped from both ends is provided. In both configurations, we consider the transfer between the pump at 1455 nm and the generated signal at 1550 nm along a 100 km fiber span. The reflectivity R in the cavity URFL gratings is set to 0.9. In order to obtain an equivalent power level for the generated Stokes signal in both lasers, the total pump power in the shown example needs to be much higher in the RDFL laser (2.7 W) than in the URFL (1.7 W). The results are shown in figure 3.4. The average level of

the RIN transfer is similar in both configurations but the oscillations are noticeable only in the ultra-long cavity laser case. For this reason, the use of the ultra-long cavity configuration can be useful to reduce RIN transfer of specific spectral components in the pump laser, as we can chose the length of the cavity to minimize its effect at a particular frequency. Obviously, ultralong cavities also have a clear advantage in terms of conversion efficiency except in the case of extreme cavity lengths [26, 93]. In cases in which these two issues are not a priority, the use of an RDFL configuration could prove more convenient given the reduced level of the RIN oscillations, their lack of a power-dependent effective reflector response [94], and their comparative advantage in terms of tunability.

3.3 RIN Transfer from pumps to the second Stokes

As it was previously explained, the main application of RDFLs and cavity URFLs can be found in the second order amplification of an input signal. In this section, the RIN transfer from the pumps to a signal at the second Stokes wavelength in RDFLs is analyzed and compared with the results obtainable in cavity URFLs. In this case, the pump wavelength is 1366 nm, the first Stokes wavelength is 1455 nm and the signal wavelength is 1550 nm. The main values used in the simulation are summarized in table 3.2. The reflectivity (R) of the FBGs is 0.9 in the case of URFL and the transmittance of the connection (η) in the RDFL is 0.85.

λ (nm)	α (dB/km)	ϵ (m^{-1})	n	g_R ($W^{-1}km^{-1}$)
1366	0.328	1.01×10^{-7}	1.4996	
1455	0.263	6.0×10^{-8}	1.4998	0.508
1550	0.197	4.28×10^{-8}	1.5004	0.42

Table 3.2: Main parameters in the simulation.

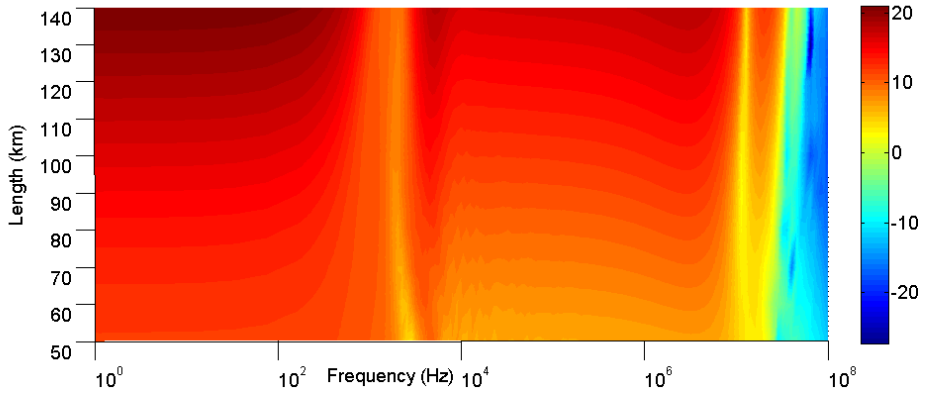

Figure 3.5: Variation of the RIN transfer vs. frequency with the total length.

Now, we consider the variation of three parameters: the total length, the initial signal power at 1550 nm and the total pump power. In the first case, the total length is varied from 60 km to 140 km, whereas the initial signal power is 1mW and the total pump power has been chosen for compensating all the losses during the transmission ($P_s(0) = P_s(L)$). As we can see in figure 3.5, the longer the RDFLs, the more RIN is transferred between the pump and the signal. This performance is similar to the performance observed in URFLs [90]. The first cut-off frequency, corresponding to the counter-propagating case, arises between 0.5 and 0.9 KHz. This cut-off frequency is minimum when the fiber length is 110 km. For frequencies higher than the cut-off, some oscillations appear. The first oscillation is the most visible with minimum RIN transfer at approximately 2 KHz independently on the length of the system. The second 3-dB frequency, corresponding to the co-propagating case, takes place at approximately 10 MHz and it is higher for longest RDFLs.

Figure 3.6 represents the variation of the RIN transfer function vs. frequency when the total fiber length is kept constant (100 km) and the initial signal power is varied from 1 mW to 50 mW. The total pump power is auto-

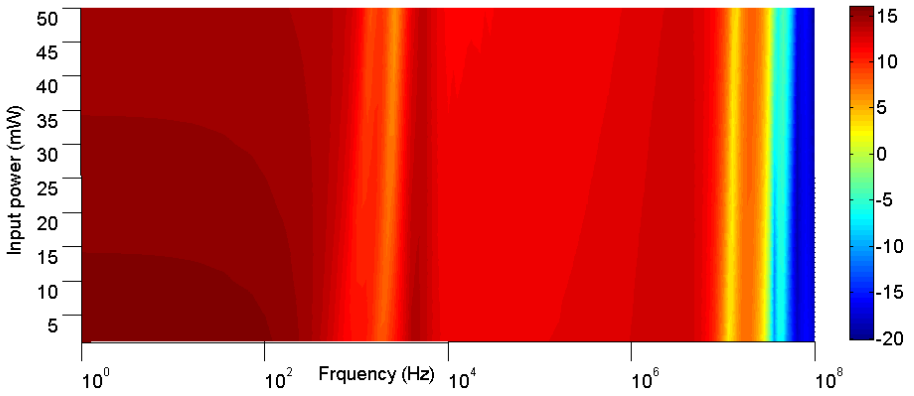

Figure 3.6: Variation of the RIN transfer vs. frequency with the input signal power.

matically adjusted so that all signal losses at 1550 nm are compensated via Raman gain. As can be seen, RIN transfer is reduced as the power of the 1550 nm signal is increased, and the effect of pump depletion is definitely relevant. Now, both counterpropagating and copropagating cut-off frequencies are dependent on initial signal power. The higher the input signal power launched, the higher the cut-off frequencies.

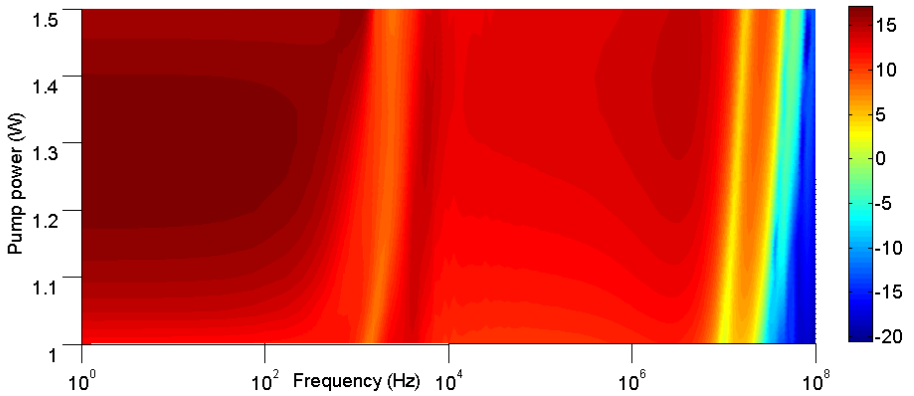

Figure 3.7: Variation of the RIN transfer vs. frequency with the total pump power at each arm.

It is also interesting for illustration to consider the case in which fiber

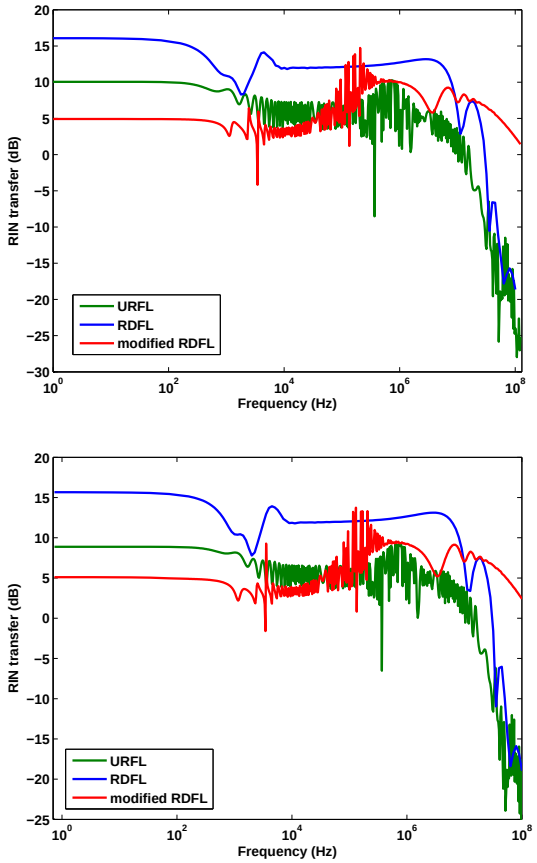

Figure 3.8: Comparison between the performance of RDFL and URFL for L = 100 km and (top) P_{in} = 1 mW or (down) P_{in} = 10 mW.

length and signal power are kept fixed, while total pump power varies. In figure 3.7 fiber length is a 100 km and input signal power is 1 mW, while total pump power (50% in each direction) is varied from 2 W to 3 W. The results, in figure 3.7, show that RIN transfer is maximum when the total pump power is 2.6 W. At this value, the 1550 nm signal power at z=L is over-amplified (the output power is ten times the input power). In terms of RIN, the best performance is obtained when the signal is slightly under-amplified. For very low total pump powers (less than 2.1 W) or very high total pump powers (more than 2.9 W), the RIN transfer is not maximum for

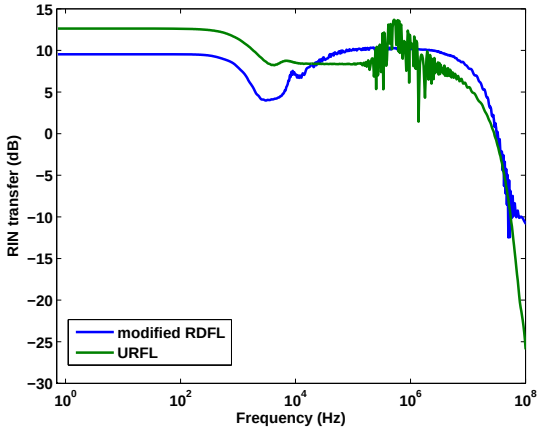

Figure 3.9: Comparison between the performance of URFL and RDFL pumped from the ends for L = 200 km and P_{in} = 1 mW.

frequencies close to 0, but instead for a frequency close to the first cut-off frequency. The cut-off frequency itself increases as the pump power goes up.

To conclude this section, we compare the performance in terms of the RIN of URFLs and RDFLs. Moreover, two cases of RDFLs are studied (the typical centrally-pumped configuration and a modified alternative that is pumped from the ends). In fact, this alternative is equivalent to the cavity URFL case with no gratings. The results are summarized in figure 3.8 and both in the cavity URFL and the alternative RDFL the maximum RIN transfer is lower than in the centrally-pumped case. The main advantage of the centrally-pumped RDFL is that the maximum RIN transfer is typically associated with the lower frequencies, while in the other two cases, the oscillations in the RIN transfer function after the first cut-off frequency can more easily exceed its initial value. Comparing the cavity URFL and the modified RDFL, in most of the situations the RIN transfer at zero frequency is higher for the URFL but the modified RDFL configuration presents oscillations at high frequencies that exceed the RIN transfer at zero frequency. As it is depicted in figure 3.9, this detrimental performance is reduced when

the fiber lenght is increased and oscillations are not visible for 200km length simulations.

3.4 Conclusions

In this chapter, the RIN transfer function for RDFLs has been investigated. A limited control over RIN transfer function of the laser can be applied at the design stage through appropriate selection of fibers and choice of length.

The cut-off frequencies for the co- and counter-propagating components appear, as expected, at positions independent of the fiber length and showing a weak linear dependence with the pump power for the one-level RDFL. Nevertheless, the cut-off frequencies for the RIN transfer from the pump to the second level is dependent on both the length and the pump power.

Our results in the first part of the chapter show that optimal configurations to minimize noise transfer to the first Stokes imply the use of higher pump power and long fibers, but not long enough to allow for the quick generation of additional Stokes, which would cause a rapid depletion of the signal. For cavities longer than 80 km and pump powers above 2.8 W, fluctuations in the RIN transfer appear, which seem to be related to the interaction of the co-propagating signal with the counter-propagating seed generated on the symmetric arm. These fluctuations are, nevertheless, generally smaller in amplitude than those appearing in cavity-based laser configurations.

In the second part of the chapter, the results show that the less noise transfer to the second Stokes is obtained when the signal is slightly under-amplified. For lossless transmission, the RIN transfer is minimized for shorter lengths and lower signal powers.

Overall, the behavior of RIN transfer in RDFLs should not impede their use in communication schemes and distributed optical fiber sensing applica-

tions, but as in the case of traditional URFLs, configurations that minimize RIN transfer should be chosen over noisier ones.

Chapter 4

Applications of URFLs and RDFLs

4.1 Introduction

In this chapter, three different potential applications of ultra-long Raman laser configurations are studied, namely:

1. Distributed amplification in telecommunications with advanced phase modulated formats, in comparison to the use of lumped amplification. This is perhaps the most natural continuation of previous application-oriented work on URFLs, as many of their advantages in this regard have been previously demonstrated for amplitude-keyed transmission formats. It is particularly interesting from an application standpoint, though, to know if the well known advantages of URFLs hold up for phase-keyed formats, which present an increased resilience to noise when compared to amplitude-keyed ones, but are on the other hand more sensitive to the effects of nonlinearity.

2. Measurement range and sensitivity improvement in Brillouin optical time-domain analysis (BOTDA) distributed sensing schemes. Recent times have seen a number of experimental and theoretical publications showcasing the possibility of using cavity and random ultralong Raman fiber lasers to improve the performance of distributed and quasi-distributed optical fiber sensors. This section lays its emphasis on comparing the potential performance and design constraints imposed by both cavity and random ultralong lasers when used in BOTDA sensing schemes.

3. Finally, we study the possible application of cavity URFLs and RDFLs to the betterment of interferometric sensors, and in particular of Sagnac interferometers. We will show that the use of first and second-order Raman amplification can, under certain constraints, increase the sensitivity of fiber optic gyroscopes, with direct potential application to areas such as seismic detection.

4.2 Ultralong Raman fiber lasers in PSK communications

4.2.1 Introduction

The use of distributed Raman amplification in optical fibre transmission links has been widely studied in recent years. Since URFLs were first proposed for quasi-lossless transmission, their use for long-haul communication systems has been studied in direct comparison to more traditional amplification solutions on several occasions, generally in laboratory setups relying on the use of the re-circulating loop technique. In [95], four non-modulated channels were transmitted up to 4000 km and the losses compensated ev-

ery 75 km by means of EDFA or URFL. For an initial OSNR of 36 dB, the degradation of the OSNR was shown to be 4.3 dB less in the case of URFL than in the case of EDFA. Similarly, the improvement offered by URFL amplification for 42.7 Gb/s ASK (Amplitude shift keying) transmission has been demonstrated both in a single channel [80] and in a DWDM (dense wavelength-division multiplexion) configurations with up to 20 channels [24]. In these cases, similar results in terms of BER (Bit error rate) were obtained for the use of EDFAs and URFLs, despite the better noise performance of URFLs, due to the impact of RIN noise, which is higher in distributed amplification. Still, URFLs presented a clear advantage in terms of signal power requirements. In this section, our objective is to perform a similar comparative study for 42.7 Gb/s transmission, using DPSK (Differential phase shift keying) modulation.

In lightwave systems, there are three major digital modulation formats: ASK (Amplitude shift keying), PSK (Phase shift keying) and FSK (Frequency shift keying) depending respectively on whether the information is encoded in the amplitude, phase or frequency of the optical carrier. ASK is the simplest format and the most widespread, but it is very susceptible to noise interference. FSK is limited in its application by its requirement of twice the bandwidth of ASK and PSK. PSK, on the other hand, is fast becoming the most popular option for next-generation communication schemes, as it is more robust (in 3 dB) to noise than ASK with a similar bitrate - spectral bandwidth product. However, modulation and demodulation are more complex for PSK and, in order to extract the phase information without ambiguity, it requires the phase of the optical carrier to remain stable. The latter requirement can be relaxed by using DPSK, which consists on coding the information not on the absolute phase, but on

the phase difference between two neighboring bits. This is the format used in our experiments.

4.2.2 Schematic setup

For this experiment, a re-circulating loop has been used. The objective of this device is to experimentally simulate a multi-span optical transmission. In order to achieve this, a controlled optical switch is used that allows an optical signal to traverse an optical system a given number of times [96] before being taken out to the receiver. In our configuration, for which schemes for EDFA and Raman amplification are shown in figures 4.1-4.2 respectively, the switching is made by means of two AOMs (acousto-optic modulators) that select the correct input for the transmission span. During the first period, AOM1 is closed and AOM2 is opened and the modulated signal is introduced in the transmission span. For a selected number of periods, AOM1 is opened and AOM2 is closed. Consequently, the output of the transmission span is reinjected into the starting point of the span. In this manner, the signal is re-circulating n times along the transmission span where n is the number of periods during which AOM2 is closed. The driver that controls the AOMs is also used to control the measurement elements (OSA, scope and BER analyzer). The main reason to choose AOMs is their extintion ratio, typically higher than 50 dB, and their polarization insensitivity [97]. We have used an analogue AOM with an extinction ratio equal to 50.6 dB and a digital one whose extinction ratio was measured only 48.6 dB.

At the input, 8 channels centered at 1555 nm are launched, with a separation between channels of 1.5 nm. The modulation used is DPSK, the clock rate is 42.7 Gb/s. A $2^{16} - 1$ bit pseudo-randomly generated sequence is used. The spectrum of the input signal can be seen in figure 4.3.

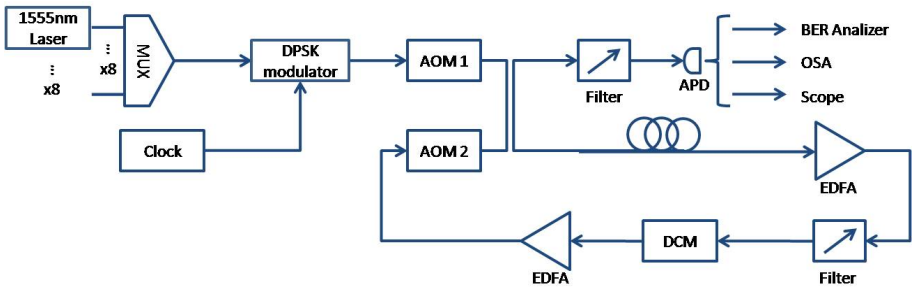

Figure 4.1: Re-circulating loop configuration using EDFA.

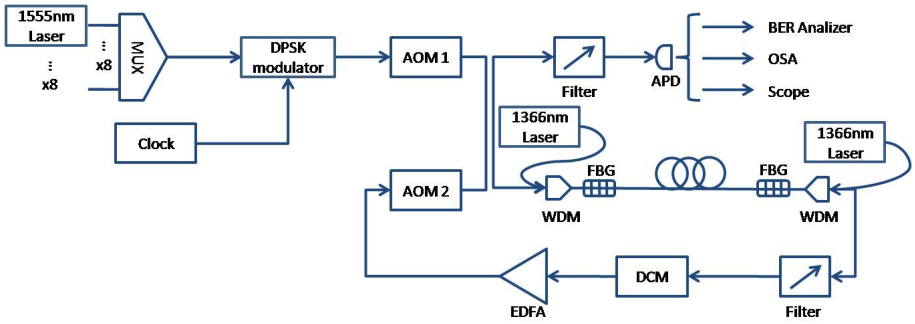

Figure 4.2: Re-circulating loop configuration using URFL.

The periodically repeated transmission span is 80 km long, and within it the losses are compensated by the use of one EDFA or the URFL configuration. In the EDFA configuration the amplifier is placed at the end of the 80 km span. The option of placing the EDFA at the beginning of the 80-km transmission span has also been tested, but the results obtained were worst in term of both noise and BER. For the URFL configuration, a typical symmetrical, quasi-lossless, cavity-based set-up is used, with pumps at 1366 nm and a set of identical FBGs at 1450 nm on the extremes to feed the amplifying Stokes wave back into the cavity.

In each circulation, for both configurations, the signal is spectrally filtered and dispersion is compensated. The signal is passed through a band-pass filter designed to remove part of the ASE noise outside the signal region. The bandwidth of the filter is 13 nm and the losses in all channels are

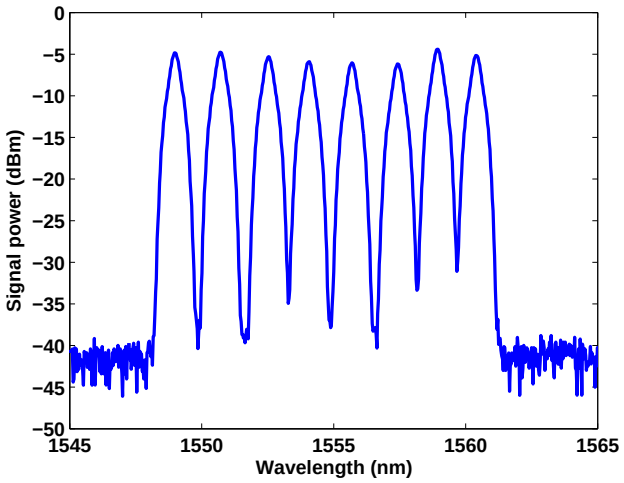

Figure 4.3: Initial spectrum of the 8 channels signal.

identical. Dispersion, on the other hand, is compensated by a DCM (dispersion compensation module) that consists on a small span of dispersion-compensating fiber whose total dispersion and slope is matched to that of the transmission fiber, to cancel out the dispersion accumulated by the signal over the transmission span. Hence, this DCM fully compensates dispersion in all the channels. Finally, an auxiliary EDFA compensates the extra losses generated in the AOMs, the DCM and the filter. It is important that the signal power will be equal at the outputs of the two AOMs.

On the receiver side, a tuneable filter selects the channel of our interest. The bandwidth of the filter is set to 1.5 nm. The OSA can be situated before the filter or after the filter to control the spectrum of all the channels or only one channel. Signal detection is performed by means of a APD (avalanche photodiode). For the demodulation, a clock recovery and a delayer are also necessary. The demodulated information is analyzed in a scope to observe the eye diagram and by a BER analyzer that compares the initial sequence and the recovered sequence and counts the number of errors. The maximum

sensitivity of our device is equal to 10^{-11}, which means 1 error per 10^{11} bits.

4.2.3 Results

In this experiment, our interest is mainly on two parameters: noise and number of errors.

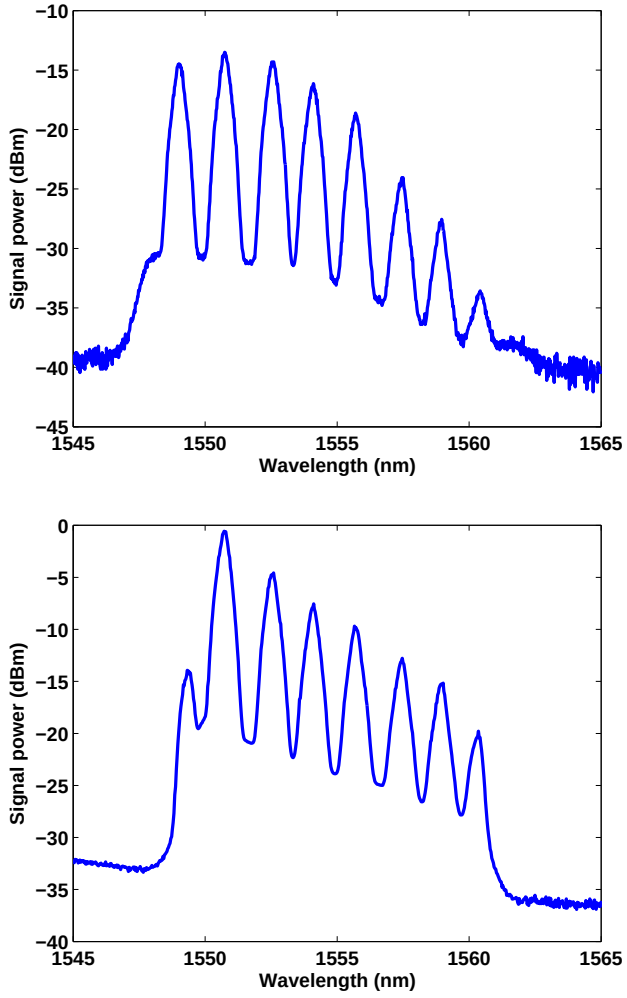

Figure 4.4: Spectrum of the 8 channels signal after 800 km for the URFL configuration (up) and EDFA amplification (down).

In terms of noise, the best results are obtained by means of the URFL set-up. The spectra after 10 recirculations (800 km) for both configurations

can be seen in figure 4.4. As much EDFA as URFL spectrum are not flat enough with an excursion between channels up to 20 dB. However URFL shows a small bandwidth (6nm) where the channels are almost equalized. To improve this performance, a flat-top tunable filter can be used. In figure 4.5, all the channels in transmission with Raman amplification have been equalized by the use of this filter. The main disadvantage of using these filters is that they increase optical losses. For this reason, the rest of the results shown in this section have been obtained without equalization.

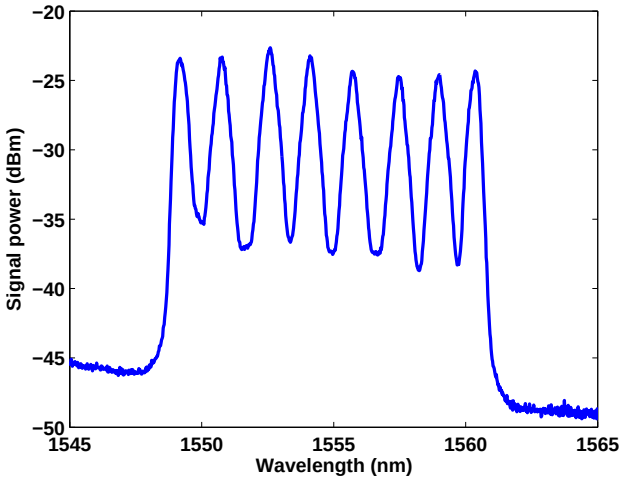

Figure 4.5: Spectrum of the 8 channels signal after 800 km for the URFL configuration using a tunable filter.

The evolution of the OSNR along transmission has been studied for the 4^{th} channel. This channel is centered at 1554.7 nm and, as it is one of the central channels, is expected to suffer more from channel cross-talk, showing higher signal distortion and worse performance than outer ones. A direct comparison between the EDFA and URFL cases can be seen in figure 4.6 up to 22 recirculations, which is equivalent to 1760 km transmission length. The difference in OSNR degradation is practically not visible for transmission distances shorter than 700 km, but becomes obvious at longer

distances. At 1760 km, the OSNR is 13.2 dB for URFL and 10 dB for the lumped amplification scheme. As expected, this result is similar to those obtained for transmission of non-modulated signals and transmission using ASK modulation.

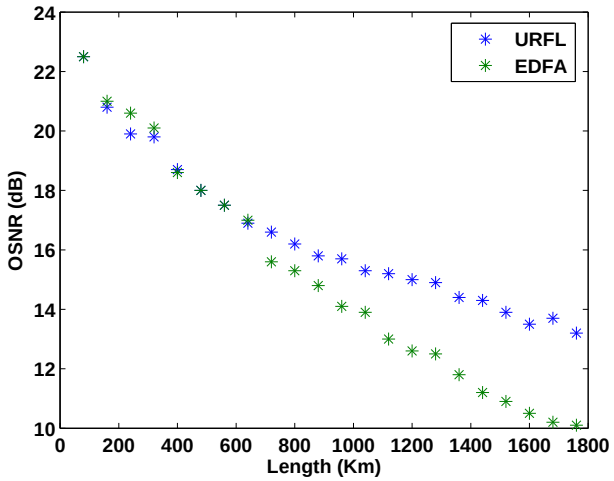

Figure 4.6: Evolution of the OSNR in the 4^{th} channel for 1760 km transmission.

The second part of the experiments consisted on measuring the number of errors. Typically, the decimal logarithm of the BER has been used for this analysis. Here, the measurements are also taken for the 4^{th} channel. The power launched at the beginning of the SMF has been modified to obtain the best results. The optimization has been made after 800 km. For the case of EDFA amplification, this point is obtained when the total signal power is 10 dBm. For the URFL, the optimal signal power is 3 dBm, meaning that the optimal balance between nonlinear affects and noise is reached at much lower input powers in the distributedly amplified scheme.

For very short distances, less than 400 km, the number of errors is higher for EDFA configuration. The hypothesis is that errors are produced by nonlinear effects due to the launched power being much higher. For longer

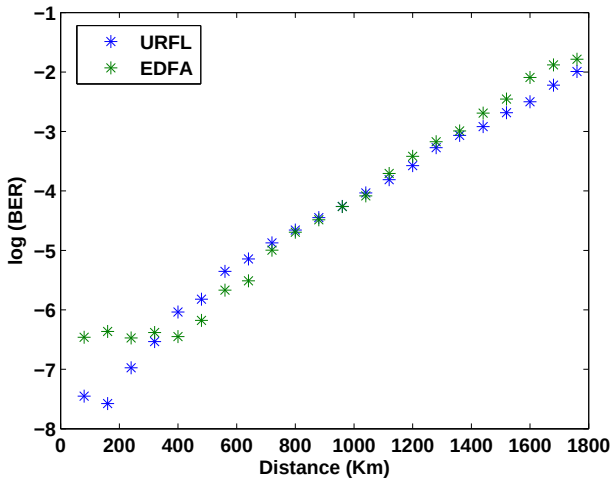

Figure 4.7: Evolution of the log(BER) in the 4^{th} channel for 1760 km transmission.

distances, the noise is the limiting factor and the BER results are similar in both cases. The evolution of the BER can be observed in figure 4.7. Note that, using phase modulation schemes, the transmission is more robust against the noise that using ASK modulation. Finally, as already seen in ASK modulated systems, it can be concluded that RIN noise acts as the limiting factor keeping URFL schemes from performing notably better than lumped amplification ones, which showcases the need for using low-noise Raman pumps in order to extract the maximum performance from this kind of quasi-lossless transmission setups.

4.2.4 Conclusion

A comparative study of the transmission of DPSK signal with either lumped EDFA amplification and distributed amplification based on URFL has been made. The spectra out of the URFL-amplified system is slightly more flat without the use of equalization filters. Considering a central channel, the OSNR after 1760 km is approximately 3 dB better in the URFL-amplified

system. However, this improvement does not translate directly into a considerable reduction of the number of errors. The main advantage is that this performance is reached for only 3 dBm signal power whereas the best performance is reached for 10 dBm using EDFAs, suggesting a clear advantage of URFL-amplified schemes in situations in which nonlinear distortion becomes the primary cause of error.

4.3 BOTDA

4.3.1 Introduction

Brillouin Optical Time Domain Analysis (BOTDA) [98, 99] has established itself as the preferred option for distributed sensing of strain and temperature applied to the real-time monitoring of large structures and transport networks. The basis for this technology is the local dependence of the characteristic Brillouin frequency shift in optical fibers with both temperature and fiber strain, which can be retrieved with a given spatial resolution through time domain analysis.

In recent years, different techniques have been proposed to improve resolution, measurement range and precision in this kind of sensors, among them distributed Raman amplification [100, 101], which has been shown to allow measurement distances in excess of 100 km with resolutions of 2 m. A potential drawback of this technique in some situations is the need to address issues such as RIN transfer from the Raman pumps to the sensing signals, as well as signal broadening from Kerr nonlinearity. Here, we study the performance differences and specific design constraints for each of the two studied amplification approaches: cavity URFLs and RDFLs. The use of these approaches in BOTDA has already been suggested and experimentally

demonstrated [25].

4.3.2 Basic theory

In a typical BOTDA temperature or strain sensor, the light sources are two lasers, one emitting a pulsed light and the other emitting a continuous wave, situated at both ends of the fiber. Generally, the pulsed light is stronger and acts as the pump that generates a Brillouin gain in the fiber. The maximum energy transfer to the continuous ligth is obtained when the difference between its frequency and the pump frequency is equal to the Brillouin frequency shift. As this shift is dependent on the temperature and the strain of the fiber, the frequency of the pump is varied in order to measure temperature or strain variations. Moreover, distributed measurements of temperature or strain along the fiber with a spatial resolution that is dictated by the pulse duration.

The performance of these sensors is determined by the measurement range and the spatial resolution. The first one is limited by the attenuation, that increases the measurement uncertainty toward the end of the fiber, whereas the second one is dependent on the pulse duration. Nevertheless, the use of shorter pulses reduces the effective distance and increases the measurement uncertainty because of the spectral broadening. Therefore, a balance between the resolution and the measurement range should be found. The use of Raman amplification has been proven as a solution to enhance the measurement range without compromising the resolution.

In this section, we are going to numerically simulate the broadening due to SPM and RIN in second order Raman assisted BOTDA. The schemes of the two configuration are in figure 4.8. Both schemes are similar with the only difference of the use of FBGs. The typical RDFL configuration,

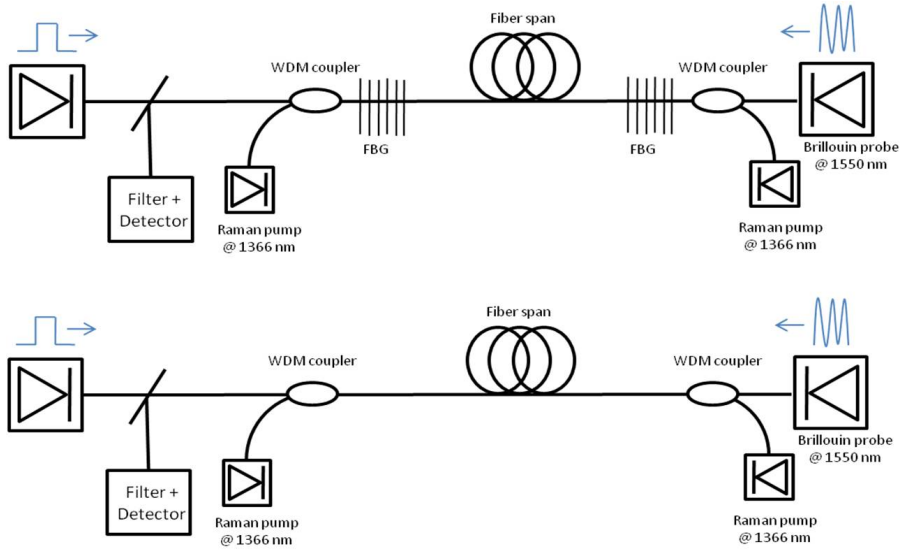

Figure 4.8: Schematic depictions of the two kinds of amplification setups used for extended the range of a BOTDA system. The top scheme corresponds to a standard cavity ultra-long Raman fiber laser with high-reflectivity gratings, whereas the reflector-free bottom one relies on Random distributed feedback lasing.

centrally pumped has not been simulated because of its difficult implementation.

For our numerical simulations, we have considered different Brillouin pump pulse peak powers, as well as different degrees of amplification, over measuring lengths ranging from 20 to 200 km, for input pulses of 20 ns duration (e.g. a spatial resolution of 2 m), close to the current operational limit at long distances. The evolution of the average power of the different spectral components in the system can be accurately modelled using the well known system of steady-state equations for URFL. The impact of SPM on the Brillouin pulsed probe is inferred through direct split-step Fourier method simulations of the nonlinear Schrödinger equation governing the propagation of the Brillouin pump pulse, using the effective gain-loss coefficient calculated from the system of steady state equations for the corre-

λ (nm)	α (dB/km)	g/A_{eff} ($W^{-1}km^{-1}$)	ϵ (km^{-1})
1366	0.38	0.51	1.0×10^{-4}
1455	0.27	0.42	6.0×10^{-5}
1550	0.19	N/A	4.3×10^{-5}

Table 4.1: Characteristics of the SSMF optical fiber used in the simulations.

sponding ultralong laser, and assuming a supergaussian time profile for the pulse. Finally, the calculated broadening of the pulse is used to calculate the z-dependent SPM-induced reduction of the Brillouin gain coefficient along the fiber, and the gain traces obtained by taking into account such variation on the Brillouin gain coefficient between Brillouin pump and probe. At all times, the fiber spans in both amplification setups are assumed to be comprised of identical ITU G.652 standard single-mode fiber (SSMF), with characteristics summarized on table 4.1, where α represents fiber attenuation, ϵ is the Rayleigh backscattering coefficient, g/A_{eff} is the Raman gain coefficient and V_g the corresponding group velocity at the specified wavelength. The initial Brillouin gain coefficient for the unbroadened 20 ns pulse was assumed to be 0.155 $W^{-1}m^{-1}$ after experimental measurements, and scales inversely with the bandwidth of the Brillouin probe pulse.

4.3.3 Results

As an example of our results, figure 4.9 displays the required pump power vs. measurement range for each of the two set-ups, in the case of Brillouin square-like pump pulses of 10 mW and a period T = 20 ns (spatial resolution of 2 m), as well as a counter-propagating continuous probe of 0.2 mW. Operation was set in this case in the condition of transparency (overall zero gain-loss for the Brillouin pump over the complete transmission length) and symmetric Raman pumping. It is worth noting that such conditions may be far from ideal, and depending on the specific sensing scheme, we

might indeed be interested in undercompensating the fiber losses or using an asymmetric scheme to minimize system impairments nonlinear broadening [25]. Nevertheless, such optimization can be made with independence of the specific amplification setup, and setting identical conditions for both URFL and RDFL allows for a fair comparison of the impact of the different impairments on each case.

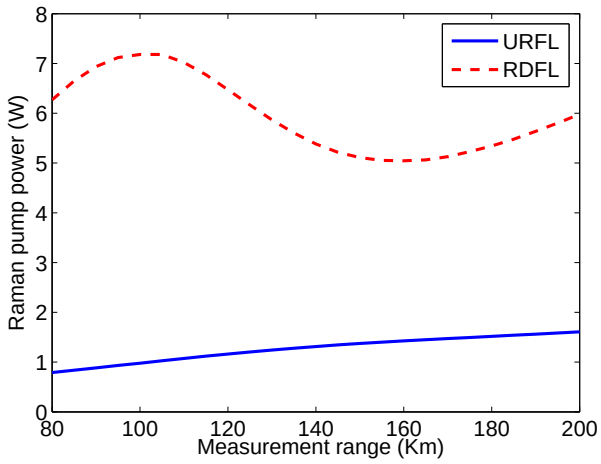

Figure 4.9: Required Raman pump power at each side for the ultra-long and the random laser to compensate the attenuation as function of the fiber length.

As can be seen, the lack of cavity feedback leads to a much lower efficiency, i.e. a higher (up to 6 times) required Raman pump power in the case of the RDFL, which makes RDFL-based systems more prone to maintenance issues, even if their non-reliance on a grating reflectors keeps them from displaying power leakage due to nonlinear spectral broadening [94]. It is also interesting to point out that, unlike in the URFL case, in which the longer the sensing fiber length, the more pump power is required, the RDFL shows a drop in the required pump power after 100 km and up to approximately 160 km, where Rayleigh backscattering-based feedback saturates, af-

ter which point the required pump power grows again with distance. Given the higher pump powers required for RDFLs, local gain is in most cases higher near both ends of the fiber, with gain distribution being smoother in cavity URFLs. Away from the extremes, the evolution of the signal is similar in both configurations, and relatively similar total power excursions (differences between maximum and minimum Brillouin pump power along the fiber) are obtained in both cases, particularly at longer lengths.

As mentioned in the introduction, a potential source of impairment in amplified BOTDAs is the impact of SPM broadening in the pump pulse. This translates into a reduction of the sensor contrast due to the lowering the Brillouin gain coefficient, as well as an increase in the uncertainty in the frequency shift detection, reducing the effective temperature/strain resolution.

Figure 4.10 shows the effect of the SPM for each configuration as a function of the fiber length and initial Brillouin pump power. The broadening is higher for RDFL and directly dependent on both fiber length and, mainly, pump power. For pump pulses below 5 mW the impact is notably reduced in both configurations, with broadenings at the end of 160 km is only a 70% or an 86% for URFL and RDFL respectively. At higher peak powers, on the other hand, broadening becomes more important, and the width of a 25 mW pulse is tripled over only 130 km and 100 km respectively over the URFL and the RDFL schemes.

The evolution of the Brillouin pump signal and its broadening due to SPM affect the recovered Brillouin sensor gain traces for a homogeneous temperature fibre. Figure 4.11 shows the maximum and minimum gain for each configuration. In a cavity URFL assisted BOTDA shorter than 100 km, the gain is almost constant along the fiber but the difference between

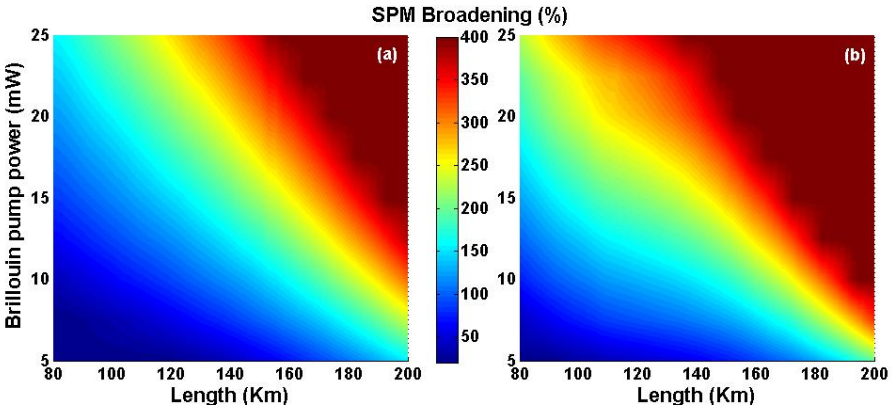

Figure 4.10: Percentage (%) of SPM broadening as function of the fiber length and the initial pump power for URFL (a) and RDFL (b).

the maximum gain and the minimum is increasing as fiber length goes up.

In RDFLs, the difference between the maximum and the minimum power (signal excursion) is higher for short distances but reduces as the measurement range goes up. The minimum difference point is reached at approximately 135 km for a 10 mW pulse pump. Increasing the Brillouin pump power, the measurement range at which the positions of lowest maximum and highest minimum gain for RDFLs are reached evolve as detailed on the inset of figure 4.11. As can also be seen, the range at which the maximum gain in cavity URFLs becomes higher than in RDFLs remains constant.

Gain traces produced by a 10 mW pump pulse over three different fiber lengths are displayed on figure 4.12. Here we can see that even though power excursion goes from being much larger to slightly smaller in the RDFL amplification scheme as length increases, the contrast in the far end of the fiber is always lower in the RDFL case due to the excess nonlinear broadening.

Finally it is particularly relevant to study the issue of noise performance. While ASE noise is similar in both schemes and rarely critical, RIN is indeed a serious source of impairment in Raman-assisted BOTDA sensing, making it convenient to rely on low-RIN Raman pump sources in general,and even

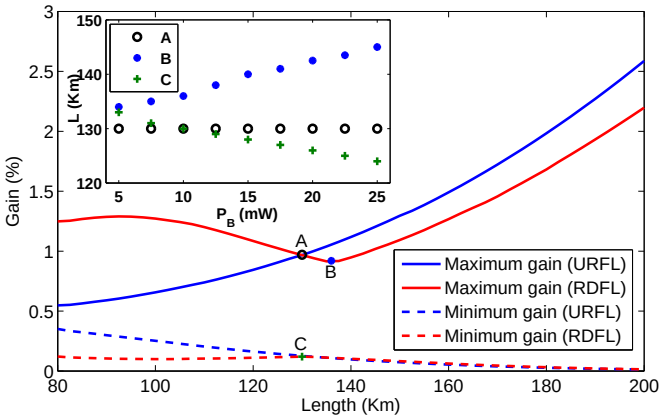

Figure 4.11: Maximum and Minimum Brillouin gain as function of the measurement range for RDFL and URFL for a 10 mW pump power. On the inset, vs. Brillouin pulse peak power: A - Measurement range at which the crossing point when maximum RDFL gain becomes lower than maximum cavity URFL gain, B - position of the lowest maximum RDFL gain, C - Position of the highest minimum gain for RDFL.

more so for the co-propagating direction. A complete analysis of the RIN transfer has been done in the previous chapter. The conclusion was that the configuration of RDFL used here minimize the impact of low-frequency RIN transfer but the high-frequency RIN transfer can exceed the zero-frequency transfer, specially for short distances.

4.3.4 Conclusions

We have presented a complete numerical comparison of two configurations of Raman assisted ultra-long BOTDAs, using cavity URFLs and RDFLs. BOTDAs longer than 140km presented a similar power excursions for the pulsed Brillouin pumps power and, consequently, similar Brillouin gain traces, but worse performance in terms of contrast and sensitivity on the extremes of the fiber. URFLs required in all cases lower Raman pump powers and led to reduced SPM broadening, which explained the observed advantages in

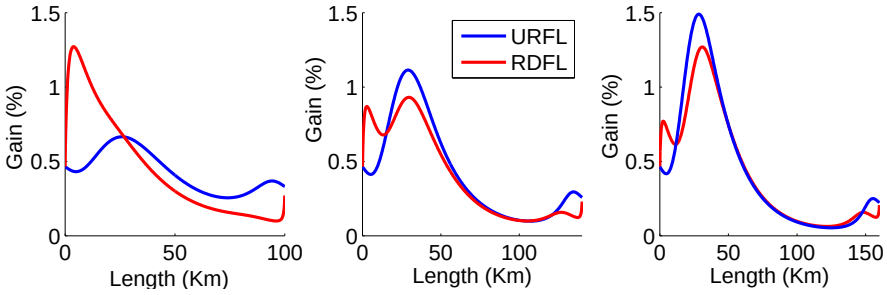

Figure 4.12: Evolution of the Brillouin gain for both kinds of amplification schemes along three different fiber lengths (100 km, 140 km and 160 km) for a 10 mW Brillouin pump power.

the Brillouin traces. The only potential advantage of RDFLs appears when considering RIN transfer from the Raman pump to the Brillouin pump and probe with long measurement distances, which is lower than in the case of cavity URFLs. Still, the much lower Raman conversion efficiency of the RDFL scheme imposes the requirement of extremely high pump powers for the RDFL configurations (up to 6 times higher than for URFLs) that renders their use impractical for most situations.

4.4 Sagnac sensors

4.4.1 Introduction

Over the past two decades, fiber Sagnac interferometers have been steadily replacing more traditional setups in rotation sensing and gyroscopic applications [102], because of their high precision, robustness, simplicity and reduced cost. Sagnac sensitivity depends directly on spool length and radius, meaning that highly-demanding applications such as the measurement of rotational seismic waves [103, 104, 105], require kilometric-length fiber Sagnac loops. The length of such kilometric loops (typically based upon low-cost standard single-mode fiber) and consequently their sensitivity, is

limited by fiber attenuation [106]. The use of amplification in the loop has been suggested as a potential method for extending loop length, enhancing detection sensitivity [106], but amplification in the interferometer would lead to non-reciprocity in the Sagnac loop, with small variations in gain causing nonlinear phase differences between the interfering beams. In this regard, the use of a distributed Raman amplification scheme seems particularly promising, thanks to the improved noise performance offered by distributed amplification in comparison to lumped amplifier solutions, which would allow the use of relatively low signal powers [107] and the minimization of the potential impact of nonlinear phase differences. The possibility of using Raman amplification to improve the sensitivity of a fiber-optic gyroscope (FOG) was first proposed in 1988 by Desurvire et al. [108], who showed that distributed gain could be used to increase the number of signal recirculations in a relatively short (1200 m), polarization maintaining loop. Over the years, other possibilities have also been considered, such as the use of erbium-doped fiber amplification within the reentrant path [109, 110], leading to a 6.56-fold increase in rotation response factor in a 200 m gyroscope. All of these solutions have been always considered in the context of relatively short gyroscopic sensors, possibly under the assumption that the amount of gain required to compensate losses in a much longer setup would bring with it a larger signal nonlinearities and non-reciprocity in the loop. As we will see, many of such expectable difficulties can be undercut by the use of advanced distributed amplification schemes, including those based on ultra long and Random distributed feedback fiber lasers.

Very recently, the intriguing idea of using conventional communication networks as giant gyroscopic sensors has been proposed [111], although such undertaking would no doubt have to face plenty of technical challenges of its

own. Here we elaborate on the idea of amplified FOGs and its possibilities. Please note that although the ultimate sensitivity of any particular device will be conditioned by the specific performance of the electronics used as well as quantum noise limitations, the analysis of specific examples with a fixed hardware is beyond the scope of our study. Our interest is, rather, on maximizing the applicability of our results, and hence we will focus on the differences, in terms of potential advantages and limitations, that would appear between traditional, non-amplified FOGs and different realisations of distributedly amplified FOGs. We will assume, when necessary for numerical illustration, lower limits for the performance of the electronics, basing those assumptions on those of readily available commercial equipment in order to ensure that our conclusions are as general as possible.

4.4.2 Fundaments of interferometric sensors

Fiber optic interferometers can be categorized into four types: Fabry-Perot, Mach-Zehnder, Michelson, and Sagnac [102]. Prior to the analysis of Raman assisted Sagnac sensors, a brief description of the other three types is presented and I also explain the reason why the idea of other kilometric fiber optic interferometers has been dismissed.

The most general idea of the fiber optic Fabry-Perot interferometers (FPIs) is a span fiber inside a cavity formed by two parallel reflecting surfaces. The magnitude to be measured (temperature, strain, pressure...) is relative with variation of the round-trip propagation phase shift, (ϕ) defined as,

$$\phi = \frac{4\pi n}{\lambda} L \tag{4.1}$$

where λ is the wavelength of the free-space optical energy (the wavelength of the optical beams), L is the cavity length and n is relative index

of the fiber. The variation of the phase shift is due to a variation of either the length or the relative index. Therefore, increasing the fiber length, the sensitivity of the sensor is improved.

A Mach-Zehnder interferometer uses two couplers to split and recombine the optical beams. Each beam goes through a different path and, after the recombination, the phase shift of the interference has information of the difference between path lengths. Michelson interferometer is similar but it only uses one coupler to split and recombine the beams at the same point. The signals go back to this point by means of two mirrors or FBGs situated at the end of the optical paths.

As has been said above, for either Fabry-Perot or Mach-Zehnder or Michelson, the measured phase depends on the fiber length. And, if we are interested on measuring temperature changes, the relative variation of the phase can be expressed as,

$$\frac{\Delta L}{L} = \alpha_{th} \Delta T \tag{4.2}$$

where the coefficient of thermal expansion α_{th} is $5.5 \times 10^{-7}\ ^{\circ}C^{-1}$ [112]. Thank to this value, a small variation of temperature is easily measured by kilometric interferometers. However, this great sensitivity is impractical and the atmospheric conditions are difficult to stabilize. This is the main reason why our interest is on Sagnac interferometers. These devices are insensible to small variation of the fiber length caused by temperature or strain changes since optical signals travel by the same optical paths.

4.4.3 Basic theory

The physical phenomenon that explains the operation of an optical gyroscope was first presented by Georges Sagnac [113, 114]. We consider a ring interferometer where two light beams are propagating in opposite directions. The path lengths are equal for both light beams whenever the ring is in a stationary position. On the other hand, if a rotation is introduced, a difference appears between the optical path [115].

As an example and without loss of generality, let us consider a rotation with an angular velocity Ω in the clockwise direction. The path lengths for the clockwise (L_{cw}) and the counterclockwise beam (L_{ccw}) are respectively $L_{cw} = 2\pi R + R\Omega t_{cw} = ct_{cw}$ and $L_{ccw} = 2\pi R - R\Omega t_{ccw} = ct_{ccw}$, where R is the ring radius and c is the free-space speed of the ligth. From here, the time difference in the interference is,

$$\delta t = t_{cw} - t_{ccw} = 2\pi R/(c - R\Omega) - 2\pi R/(c + R\Omega) \approx (4\pi R^2/c^2)\Omega \quad (4.3)$$

with the assumption that $c^2 >> R^2\Omega^2$. Consequently, considering a fiber-optic gyroscope with N fiber loops, there is a phase difference between the two signal beams equal to,

$$\delta\phi_s = (2\pi c/\lambda)\delta t = (8\pi^2 NR^2/\lambda c)\Omega = (4\pi LR/\lambda c)\Omega \quad (4.4)$$

where λ is the wavelength of the free-space optical energy (the wavelength of the optical beams), L is the fiber loop length and c is the speed of light in the vacuum. Therefore, the two obvious ways to increase detection sensitivity are either extending the fiber length, which would bring an increase in the loop losses, or enlarging the loop radius, which increases the risk of non-reciprocity between the two optical paths by making local fiber

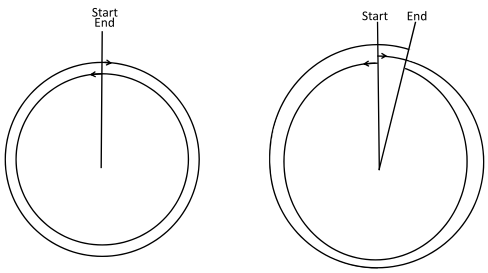

Figure 4.13: Schematic explanation of the Sagnac effect. The first coil (left) is not rotating and the optical paths are equal. The second coil (right) is rotating and, consequently the optical paths are different.

conditions less controllable. In our case, we chose to increase the fiber length and to use Raman amplification to compensate the fiber losses.

4.4.4 Proposed designs of amplified FOGs

The most commonly used configuration for a FOG is the open-loop biasing scheme [116]. In this scheme, a polarizer is used to prevent the arrival of the signals to the detector in different polarizations. Then, the intensity in the CW and CCW waves is equalized to ensure that the output phases of both beams are, in the absence of rotation, identical. Typically, this configuration includes a piezoelectric transducer (PZT) that acts as a phase modulator. A phase modulation allows for the gyroscope to be biased to its maximum sensitivity point. The typical photodetector response to a phase change has a cosine form. Hence, the sensor is less sensitive for small variations, as well as being incapable of detecting the direction of the rotation. For this reason, a nonreciprocal phase shift bias is usually introduced to improve sensitivity. The basic open-loop biasing scheme is described in figure 4.14. Our scheme is based on this configuration, also used for rotational seismometers [103, 104].

The proposed configurations are summarized in the scheme depicted in figure 4.15. We consider the used lock-in amplifier has similar specifications

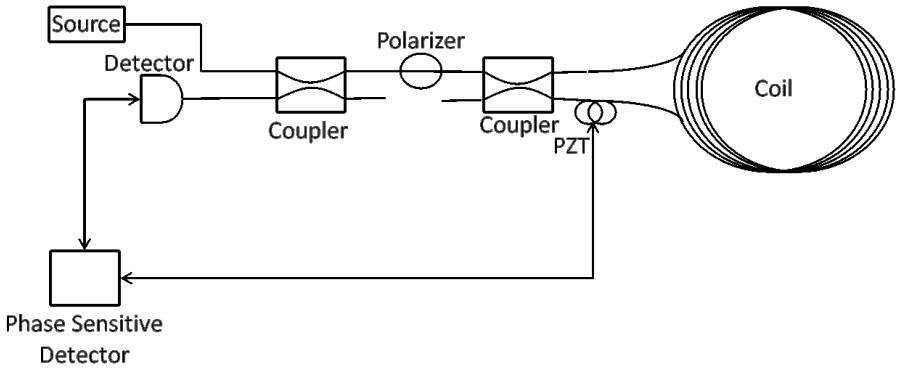

Figure 4.14: Schematic of FOG with the open-loop biasing scheme

than mid-range commercial lock-in amplifiers, able to detect variations of the order of 0.001 ° ($\approx 1.8 \times 10^{-5}$ rad). We will use this typical value as a limit for the acceptable nonlinear phase differences in the system. Considering the extreme length of the loop, the system is assumed to operate on depolarized light [117], which can be guaranteed with the use of depolarizers at the source output and in the sensor loop [104]. We will consider operation in the optical C-Band (1530 to 1565 nm) in order to take advantage of the reduced fiber attenuation and the availability of high-grade commercial components designed for telecommunication.

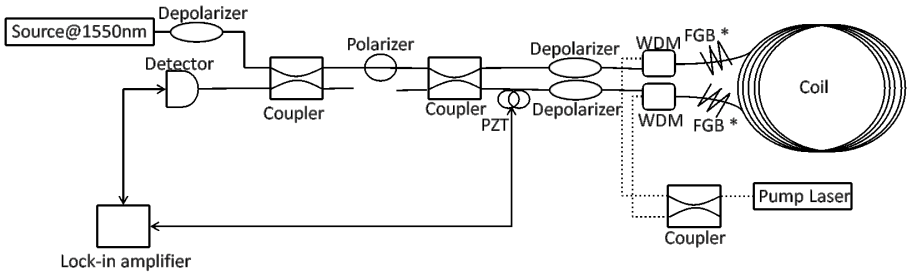

Figure 4.15: General schematic depiction of our proposed configurations. Pump power is 1455nm in the first order configuration and 1366nm in the second one. Two fiber Bragg grating reflectors (FBG) centered at 1455nm are included only in the ultra-long Raman laser configuration. The signal is centered at 1550 nm.

Without amplification considerations, the minimal rotation speed of Ω_{min} measured detectable by an interferometric FOG in the shot noise limit can be expressed [118] as

$$\Omega_{min} = \frac{\lambda c}{4\pi RL} \cdot \sqrt{\frac{Bhc}{\eta \lambda P_{PD}}} \tag{4.5}$$

where η is the photodetector efficiency, B is the sensor bandwidth, h is the Planck constant, c is the speed of light in a vacuum and P_{PD} is the power at the photodetector. To enhance gyro accuracy it is thus necessary to increase the product $RL\sqrt{P_{PD}}$. P_{PD}, though, is dependent on the loop length through the fiber attenuation coefficient:

$$P_{PD} = P_0 \exp\left(-\alpha L + \sigma\right) \tag{4.6}$$

where P_0 represents input power, α represents fiber attenuation at frequency λ and σ accounts for the rest of the optical losses in the system (splices, connectors, depolarizers...). Hence, in a non-amplified system, an increase of L leads to either a lower power at the photodiode or to the use of higher input signal powers. Too high an input power will lead to enhanced Kerr nonlinearity induced nonlinear phase differences, which might affect resolution and take us away from the shot-noise limited case. Increasing coil radius R, on the other hand, makes the gyroscope less manageable and more vulnerable to environmental factors. Lumped optical amplification before the photodiode could increase P_{PD} without an increase of input signal power, but once again at the cost of increased optical noise.

Distributed amplification, on the other hand, has been shown [107] to offer the best trade-off between induced nonlinearities and accumulated noise, and could allow the use of increased loop lengths without having to stray

from the shot-noise limited case. For this application, we propose three alternative amplification schemes and study their potential performances. In all the cases the system has been devised to compensate for the whole attenuation generated in the fiber, effectively making P_{PD} independent from the loop length L.

These alternatives proposed here are:

- A fist-order distributed amplification scheme, using a single 1455 nm pump injected into the fiber loop just before the last coupler, resulting in bi-directional amplification at wavelengths in the vicinities of 1550 nm.

- A cascaded second-order distributed amplification scheme, based on URFL configuration. The injection point for this 1366 nm pump is once again just before the last coupler, but two fiber Bragg grating reflectors are added at both ends of the coil, tuned at 1455 nm. As in the previous configuration, the 1455 nm component provides distributed Raman amplification in the C-Band.

- A similarly cascaded second-order scheme, this time without grating reflectors, in which the feedback is provided by randomly distributed Rayleigh scattering, i.e.: a RDFL.

In order to provide an accurate analysis of the behaviour of the optical section, all relevant sources of impairment need to be considered. While fiber birefringence can be considered a problem in non-depolarized FOGs, its effect on a depolarized CW-based sensing scheme such as ours can be neglected. Variations on local environmental conditions across the coil, which could give rise to the Shupe effect[119], are similarly controllable through appropriate winding and can be considered independent on the amplification

scheme[120], and fiber temperature variations due to the high powers of the Raman pumps are symmetrical for both propagation directions. Noise, on the other hand, both arising from amplified spontaneous emission and from interference with single and from Rayleigh backscattered radiation, as well as differences in nonlinear phase shift due to the Kerr effect, might become particularly relevant in an amplified system such as the proposed ones, and their impact needs to be carefully gauged. Additional optical sources of noise, such as relative-intensity noise (RIN) transfer from the pumps can be effectively minimized at the pump power levels considered in this study through the use of laser diode pumps, and will not be considered in our analysis.

We numerically model the behaviour of the amplification system through a set of steady state ordinary differential equations (ODEs) for the proposed schemes, obtaining the power distribution of the different spectral components along the coil length, or equivalently the effective gain-loss coefficient, as well as the evolution of the optical signal-to-noise ratio. This approach, commonly used in the context of fiber communications, allows for the calculation of accumulated nonlinear phase shift, as well as an accurate evaluation of the impact of noise, taking into account not only amplified spontaneous emission noise generation within the fiber coil, but also Rayleigh backscattering noise, which might cause multi-path interference and in an amplified system such as ours has the potential to be the most important source of optical noise. The effect of pump depletion on power evolution is also taken into account.

The clockwise (counter-clockwise) - propagating signal beam will accu-

mulate a nonlinear phase shift that can be expressed by the equation:

$$\phi_{NL} = \int_0^L \gamma(P_a + 2P_b)dz \tag{4.7}$$

where P_a and P_b are the clockwise (counter-clockwise) and counter-clockwise (clockwise) - propagated signals, respectively, γ is the nonlinear coefficient, L represents the propagation distance, and the phase shift produced by the presence of the pumps has been deliberately left out, as it adds a constant term identical for both propagation directions. Please note that although both pump and signal are bi-directionally injected into the loop, their clockwise and counter-clockwise components for each of them are generated from a single laser diode (signal) or pump laser (Raman pump). That is, the output of a single depolarized Raman pump is split in two and injected into the loop, just as the sensing signal is split at the coupler. By design, any intensity oscillations on the loop are symmetrical in the clockwise and counter-clockwise directions, and hence can be safely removed from the equation.

It is convenient to create a figure of merit that quantifies the reduction of non linear effect when amplification is included. This created figure, (κ) is defined by the equation

$$\kappa = \frac{\phi_2}{\phi_1} \tag{4.8}$$

where ϕ_2 is the accumulated non linear phase when amplification is present, and ϕ_1, the same with no amplification, for the same output power. κ is represented in figure 4.16 as function of the fiber length. Obviously, κ decreases when the fiber length is increased and nonlinear phase shift becomes reduced to a 50% when the length is approximately 28km. URFL and RDFL configurations offer a similar performance than the first-order case

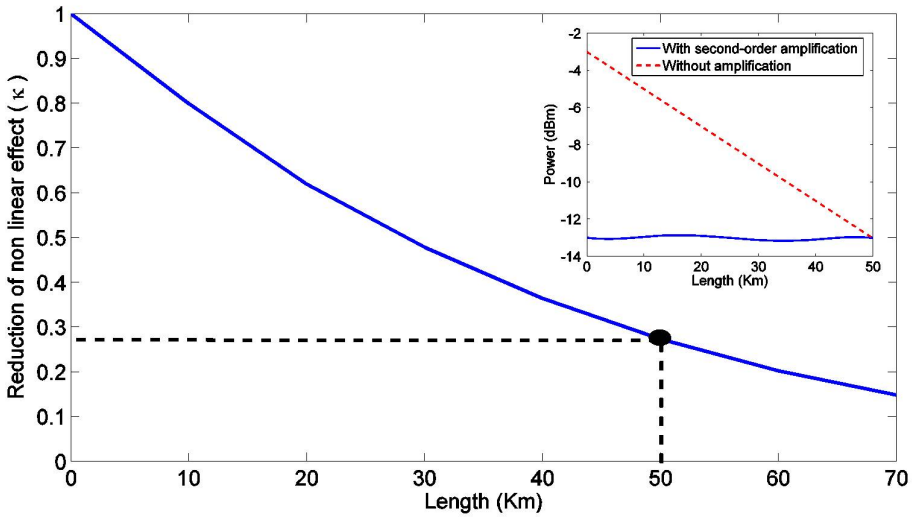

Figure 4.16: Relative improvement in terms of reduced nonlinearities obtained when the fiber loop is pumped to amplify the signal, as defined by the figure of merit κ. Inset: Signal power evolution for the specific case of a 50 km loop, for identical output powers, in the cases of no amplification and second order amplification.

shown in the figure in terms of total accumulated nonlinear phase shift.

4.4.5 Results and discussion

In order for the signal to be properly detected, we have to ensure that amplification noise does not grow to the point of becoming a problem in detection. For this reason, optical signal-to-noise ratio (OSNR) levels, defined as the ratio of the optical signal output power to the integrated noise power over a given bandwidth, are calculated for all the studied configurations. The lower limit for the input signal OSNR, calculated over a 1 nm bandwidth, is assumed to be a very conservative 33 dB, perfectly achievable for most commercially available sources. Under this conditions we observe that the lowest OSNR is about 22 dB for the case of the RDFL considered up to a 70 km spool length. For illustration, figure 4.17 shows the evolution of the OSNR vs. distance for the two limit signal powers considered, 100 μW

and 20 μW and the second order amplification case. Interestingly, the main source of noise on both cases, and hence for all intermediate ones, is Rayleigh backscattering at the signal wavelength. This is not surprising, given that a FOG is by design a bidirectional system, in which single back reflections from one of the two propagating beams couple into the other. This noise is, as expected, enhanced by the presence of bidirectional distributed amplification, but not to a point in which it constitutes a problem. For all the spool lengths and powers considered the combined ASE and Rayleigh backscattering noise are low enough for their effect to be considered negligible in the detection process.

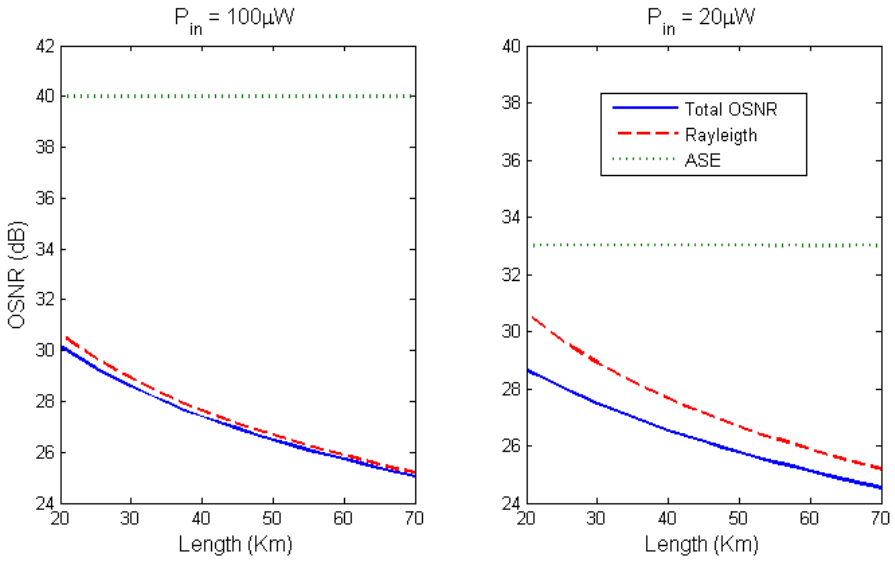

Figure 4.17: Evolution of OSNR vs. distance and the contribution of ASE and Rayleigh in the case of ultra-long Raman laser configuration for:(a) Input power = 100 μW (b) Input power = 20 μW

Nonlinear phase differences are generated when the counter-propagating beams experience different intensities along their optical path, depending on their clockwise or counter-clockwise rotation, and can also limit the minimum rotation speed detectable by the FOG. They may be caused by a

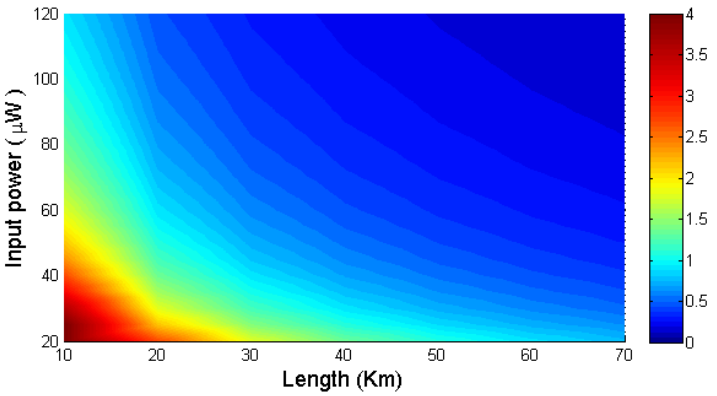

Figure 4.18: Maximum variations in signal power (in %) acceptable for a second order amplification scheme with gratings (ultralong laser.

non-optimal splitting of the signal beam, environmental variations of the local loss in the fiber or, to a much larger extent, to variations on the amplification, experienced by the optical beams due to oscillations in pump power, whether due to a non-ideal pump split or to a temporal variation of the splitter response when continuously operating at high powers. As mentioned above, the use of a distributed amplification scheme helps keeping signal excursion low, hence reducing nonlinear phase differences. This effect becomes more obvious the flatter the gain distribution becomes, so it is to be expected that the second-order amplification schemes will be more resilient to nonlinear phase induced impairments. In practice, though, signal excursion is very small in all cases, and the improvement offered by the more complex scheme is only noticeable at coil lengths over 40 km. Still, the main immediately noticeable handicap for the mirrorless random distributed feedback laser is its requirement of much higher pump powers than the rest of the configurations, as we will see below.

Figure 4.18, shows the maximum variation in input signal power accepted by the system, assuming perfectly symmetric pumping. The figure

has been obtained by finding the power variation that leads to a nonlinear phase equal to 1.8×10^{-5} rad (the sensitivity of a typical commercial detector). Logically, this threshold for acceptable variation will be reduced for increasing input signal power and length. The length limit for the coil, conditioned by the system's signal power variation, will be thus the one for which the nonlinear phase difference reaches the sensitivity of our lock-in amplifier. The values in the figure correspond to the second order amplification scheme, however there is not big difference with the other two cases.

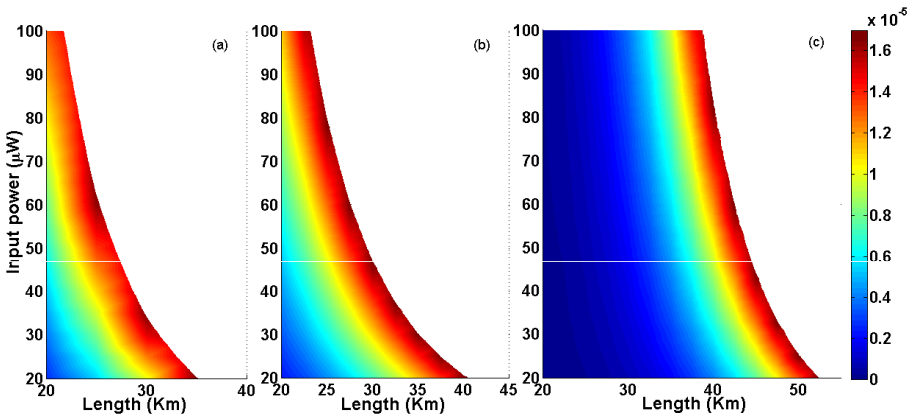

Figure 4.19: Nonlinear phase shift vs. fiber length and input power when the pump power is not balanced (49% is launched in one direction and 51% in the opposite one) for the mirrorless second-order amplification scheme (a) the first-order one (b) and the ultra-long Raman laser (c). When the shift is higher than the stablished limit of 1.8×10^{-5}, the contour plot is filled in white so the operative boundary is easily observed.

The effect of pump asymmetry is summarized on figure 4.19, where the maximum spool length, for which the nonlinear phase difference reaches the limits of the detector sensitivity, is plotted against input signal power and pump power split. As can be observed from the figures, the improvement provided by the URFL scheme is apparent in this case, allowing the use of

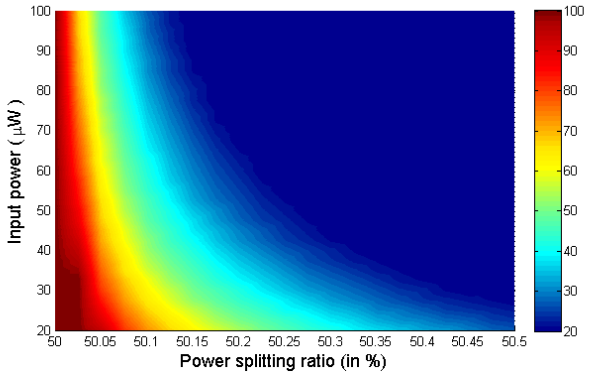

Figure 4.20: Fiber length that produces a nonlinear phase shift equivalent to the minimal phase detectable for a commercial device when the coupler/splitter is not balanced (affecting the signal power and pump power).

much longer spool lengths for similar input signal powers. Assuming a 51% split and using the mirrorless second-order configuration, an input power of 100 μW, nonlinear phase would limit interferometer length to just 22 km. Operating at a lower power of 20 μ W, on the other hand, leads to a much higher limit length of 35 km. If we use a first order or URFL scheme for the same power, spool length could be incremented to reach 40 km and 52 km respectively. This is, for example and to the extent of our knowledge, about 5 times longer than the longest non-amplified implementation to date in the context of seismic detection [104], and could subsequently allow a five-fold increase in the detector sensitivity. Please note that the presence of distributed amplification in the line does not offer any inherent protection against the uncertainty introduced by the variability of the coupling coefficients for each port, but does keep overall variation of the transmitted power within the transmission line low, which contributes to improving the performance.

Finally, we analyze the combined effect that the simultaneous and coordinated asymmetry of pump and signal beams, which could in principle

be expected to be the worst-case scenario, would have on the accumulation of nonlinear phase difference. Whereas in the previous cases, asymmetries arose at only one wavelength (signals or pumps), now both components are affected by the deviation of the split ratio. This is summarized on figure 4.20, which represents the maximum spool length vs. split ratio and input signal power, for the URFL scheme. As can be seen, even though such situation imposes higher restrictions on system reliability, spool length could still be increased to between 30 km for a 20 μ W signal as long as the split ratio is maintained within a $\pm$ 0.5 % accuracy.

The combined effect of an asymmetry of pump and signal beams could produce a compensation of both contributions to the nonlinear phase asymmetry. Nevertheless, using the configurations of first-order amplification and a URFL, this compensation can take place only when the asymmetry in the splitting of pump powers is of opposite sign to the asymmetry in the signal powers, which is not a realistic situation, considering they both traverse the same splitter. However, and quite surprisingly, this compensation happens to be possible with same-sign asymmetries in the mirrorless second-order configuration based on RDFL amplification. In figure 4.21, we observe how this compensation is produced for two different span lengths. For a 61 km length coil, the nonlinear phase differences between signals are totally compensated when the asymmetries are identical for both pumps and signal. This ideal length is only dependent on the Rayleigh coefficient and, consequently, is not easy to predict and control at the design stage. Although the effect is indeed very interesting and can be used to reduce nonlinear impairments with a careful choice of splitter in a given configuration, it is not particularly useful in the general case, as we must take into account that the use of a RDFL setup at the long lengths required for the effect to

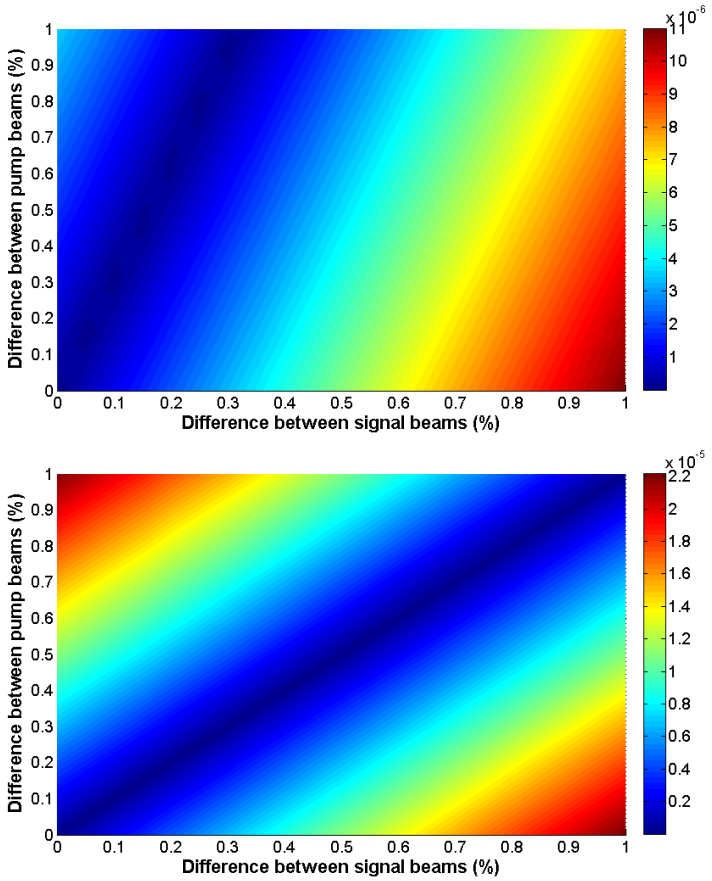

Figure 4.21: Nonlinear phase shift vs. pump and signal asymmetries for 20 μW input signal powers and (up) 33Km fiber length and (down) 61Km fiber length.

be observed would impose the use of very high pump powers, increase cost, reduce system durability and induce a more pronounced fiber temperature gradient in the vicinities of the pump injection points, as well as suffer from higher relative intensity noise transfer from the pumps to the signal. From our simulations we calculate the required pump power in the mirrorless configuration to be between seven and ten times higher than in the URFL case. Specifically, for a 61 km length FOG, 0.55 W pump power is launched in each direction in the URFL scheme whereas the pump power required for the mirrorless case is approximately 4.32 W.

4.4.6 Conclusions

We have performed a study of the limitations imposed by noise and nonlinear phase shift in distributedly amplified fiber optic gyroscopes. Our results show that distributed Raman amplification, whether provided through first or second order configurations relying on traditional configurations as well as URFL and RDFL designs, can allow a meaningful increase of the spool length, even under rather conservative assumptions about the reliability of other system components. We have shown that in most of the meaningful cases the effect of optical ASE noise can be considered negligible, which makes nonlinear phase shift accumulation the main deleterious effect. In this regard we have demonstrated that nonlinear phase shift differences can be kept under control as long as some system design constraints over split ratio and input power variability are exerted. This constraints allow loop length to be increased without having to decrease the received power at the photodiode, bringing with it a direct increase of the FOG sensitivity. In particular, and assuming realistic performance limits for the sources and detectors, the use of an URFL architecture has been shown to be able to produce a nearly 5-fold increase in sensitivity to systems that currently see their performance limited by fiber attenuation. This improvement could be applied to the design of highly sensitive fiber-based rotational seismometers. As an example, a 50km FOG with a similar configuration as that of ref. [104], but operating in the C-Band, could see its performance improved from 4.27×10^{-8} rad/s (for a 11.13 km loop) to $\approx 1.14 \times 10^{-8}$ rad/s for a 52 km loop with a signal in the vicinities of 1550 nm. A similar improvement could be applied more recent implementations of seismic detectors, such as the one shown in [105].

Chapter 5

Raman polarizers

The main subject of this chapter is the all-optical control over the state of polarization (SOP) of light, understood as the control over the SOP of a signal beam through manipulation of the SOP of a pump beam. In this study, a new mathematical model for the evolution of the SOP of two beams in random birefringence fiber (standard fibers) is obtained. Our vectorial model considers the interaction between pump and signal through Raman and Kerr effects and is valid as well for fibers with low PMD. The result is computer friendly and it can be used to explain virtually all practically relevant situations, including the interaction between co and counter-propagating beams, under the undepleted regime as well as the depleted regime of Raman polarizers.

5.1 Introduction

In the past few years, motivated by the recent developments of transmission protocols based on polarization multiplexing [121], there has been an increasing interest in developing nonlinear devices for achieving all optical and ultrafast polarization control. Although linear polarizers are the most

popular and robust optical element used to exercise control over the polarization state of a light beam, its use is limited due to two important problems. Firstly, a linear polarizer transforms input beams with an essentially random distribution of polarizations into beams with a well-defined deterministic state of polarization (SOP) by wasting the orthogonal component. The overall 50% loss of energy inherent to this method can, in principle, be accepted in practical applications. A much more serious problem is that, in the presence of signal polarization fluctuations and as a result of polarization dependent loss, outgoing beams acquire large intensity fluctuations. Thus, the interconnection with optical devices that postprocess these strongly fluctuating signals becomes problematic, especially if these devices are nonlinear. Polarizers based on Kerr effect [122, 123], Brillouin scattering [124] or Raman [125] have been studied in recent times. Here, my interest is on the last kind: Raman polarizers.

As it was previously mentioned, the process of stimulated Raman scattering (SRS) in silica fibers is highly polarization-dependent: the gain coefficient reaches its maximum value whenever the state of polarization (SOP) of the signal is parallel to the pump SOP, whereas the amplifier gain is reduced by two orders of magnitude if the two SOPs are orthogonal (see figure 5.1).

In a real fiber network the fiber birefringence changes stochastically along the fiber span. The net effect of this stochastically varying birefringence is to greatly reduce the polarization dependence of Raman gain. As a result, the effective Raman gain reduces to its span-averaged value, which is equal to approximately half of its maximum value. Such averaging of the gain between two orthogonal SOPs is a favorable feature for Raman amplifiers (as signals are equally amplified independent on its initial SOP) but not for Raman polarizers. The first important difference between those devices

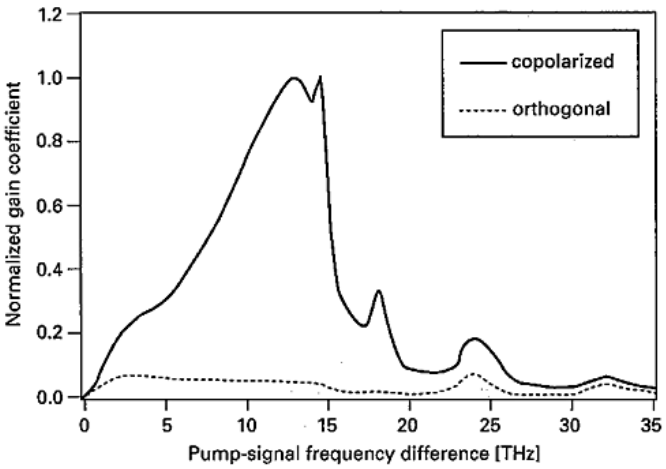

Figure 5.1: Normalized Raman gain coefficient for copolarized and orthogonally polarized pump and signal beams. [126]

is that Raman amplifiers operate with relatively high values of the PMD coefficient, whereas Raman polarizers use low PMD fibers to reduce the averaging.

Many analyses of the Raman effect in optical fibers assume a scalar model, which is only valid for high-PMD fibers or depolarized pumps and signal. For the case of polarizers, the analysis should be based on the vector theory of SRS, presented in previous studies [127, 128, 129, 130]. Although an analytical insight into the problem was presented in [128, 129], its applicability was limited to the regime in which the beat length of the fiber is substantially smaller than the birefringence correlation length. The model presented in [130] is most general and accurate, however it is resource-consuming in terms of computational time and since it is not formulated in terms of deterministic differential equations, it is rather difficult to extract from it physically transparent information about the role of the different processes ruling the overall polarization dynamics. For this reasons, we set out to develop a complete, physically insightful model that could also be

used for the efficient computation of Raman polarization dependent gain and its associated effects.

5.2 Mathematical model

Our theory is essentially the generalization of the one-beam theory in [43] to the case of two beams interacting not only via the Kerr but also via the Raman effect. Only two assumptions are considered in that analysis. The first one is that the minimum between the fiber length and the nonlinear length is longer than the correlation length of the fiber: $\min(L_{NL}, L) >> L_C$. This inequality holds true for almost all practically relevant situations. Secondly, the fixed modulus model is considered for the random variation of the birefringences, that is, the birefringence tensor is characterized by,

$$\triangle \mathbf{B}(\omega) = \triangle\beta(\omega)(\cos\theta\boldsymbol{\sigma_3} + \sin\theta\boldsymbol{\sigma_1}) \tag{5.1}$$

where $\triangle\beta(\omega)$ is constant and θ is the stochastic variable. The analysis considering both parameters stochastic variables produces identical results [42]. And σ_i are the typical Pauli matrices defined as,

$$\sigma_1 = \begin{pmatrix} 0 & 1 \\ 1 & 0 \end{pmatrix}; \sigma_2 = \begin{pmatrix} 0 & -i \\ i & 0 \end{pmatrix}; \sigma_3 = \begin{pmatrix} 1 & 0 \\ 0 & -1 \end{pmatrix} \tag{5.2}$$

In the most basic model of interaction of two fields within a Kerr- and Raman-active medium, the equation of motion of the pump beam is formulated in the form,

$$\pm i\frac{\partial \mathbf{U}_p}{\partial z} + i\beta'(\omega_p)\frac{\partial \mathbf{U}_p}{\partial t} = -\triangle\mathbf{B}(\omega_p)\mathbf{U}_p - \gamma_{pp}\frac{1}{3}[2(U_p^* \cdot \mathbf{U}_p)\mathbf{U}_p + (\mathbf{U}_p \cdot \mathbf{U}_p)U_p^*] - \frac{2}{3}\gamma_{ps}[(U_s^* \cdot \mathbf{U}_s)\mathbf{U}_p + (\mathbf{U}_s \cdot \mathbf{U}_p)U_s^*$$

$$+(\mathbf{U}_p \cdot U_s^*)\mathbf{U}_s] + i\epsilon_p g_0[(\mathbf{U}_p \cdot U_s^*)\mathbf{U}_s] \tag{5.3}$$

A similar equation (with indices s and p interchanged) arises for the signal beam. Here U_p is the pump field, written for the two-component field vector $U_p = (u_{px}, u_{py})^T$, where u_{px} and u_{py} are the amplitudes of the normal polarization modes of the fiber. $\beta(\omega_p)$ is the propagation constant and $\beta'(\omega_p)$ is its frequency derivative. The upper sign ("+") describes the configuration when the signal and pump beams propagate in the fiber in the same direction (co-propagating geometry), while the lower sign ("-") is related to the situation when they propagate in opposite directions (counter-propagating geometry). The self-phase modulation (SPM) and the cross-phase modulation (XPM) coefficients are denoted by γ_{pp} and γ_{ps}, g_0 is the Raman gain coefficient and $\epsilon_p = -\omega_p/\omega_s$ whereas $\epsilon_s = 1$.

The first step consists of transforming equation 5.3 to the local axes of birefringence by performing the rotation of the field vectors as,

$$\overline{U}_j = \begin{pmatrix} \cos\frac{\theta}{2} & \sin\frac{\theta}{2} \\ -\sin\frac{\theta}{2} & \cos\frac{\theta}{2} \end{pmatrix} U_j \tag{5.4}$$

where j = p, s. This transformation only produces a change in the form of the birefringence tensors, which now become

$$\overline{\triangle B}(\omega_p) = \begin{pmatrix} \triangle\beta(\omega_p) & \mp\frac{i\theta_z}{2} \\ \pm\frac{i\theta_z}{2} & -\triangle\beta(\omega_p) \end{pmatrix}; \overline{\triangle B}(\omega_s) = \begin{pmatrix} \triangle\beta(\omega_s) & -\frac{i\theta_z}{2} \\ \frac{i\theta_z}{2} & -\triangle\beta(\omega_s) \end{pmatrix} \tag{5.5}$$

where θ_z is the derivative of θ with respect to z. It is different from zero owing to the random changes of orientation of the birefringence axes. Namely, the change of θ is driven by the white noise process with zero means and $\langle\theta_z(z)\theta_z(z')\rangle = 2L_c^{-1}\delta(z-z')$, where L_c characterizes the typical

distance at which θ changes randomly.

Thank to the assumption that $\min(L_{NL}, L) >> L_C$, it is possible to separate the fast motion related to the rapid changes of θ with the slow motion that occurs on the scale of the nonlinear length. The transformations are

$$V_p = T_p \overline{U}_p = \begin{pmatrix} a_1 & a_2 \\ -a_2^* & a_1^* \end{pmatrix} \overline{U}_p; \quad V_s = T_s \overline{U}_s = \begin{pmatrix} b_1 & b_2 \\ -b_2^* & b_1^* \end{pmatrix} \overline{U}_p \tag{5.6}$$

Matrices T_p and T_s has been chosen to eliminate the birefringence terms in the motion equation. Consequently, they obey

$$\pm i \frac{\partial T_p}{\partial z} + \overline{\triangle B}(\omega_p) T_p = 0; \quad i \frac{\partial T_s}{\partial z} + \overline{\triangle B}(\omega_s) T_s = 0 \tag{5.7}$$

The result brings about a vast number of cubic terms composed of different combinations of V_{p1}, V_{p2}, V_{s1}, V_{s2} and their complex conjugates, multiplied by some terms that they are products of two coefficients of the form $u_m u_n$, $u_m^* u_n^*$ or $u_m^* u_n$ with n, m = 1,...,14. Products with $m = n$, we shall call self-products, whilst products with $m \neq n$ are called cross-products. Terms $u_{1,...,6}$ correspond with the SPM and they are related to a_1 and a_2 as

$$\begin{array}{ccc} u_1 = |a_1|^2 - |a_2|^2 & u_2 = -(a_1 a_2 + a_1^* a_2^*) & u_3 = i(a_1 a_2 - a_1^* a_2^*) \\ u_4 = 2 a_1 a_2^* & u_5 = a_1^2 - a_2^{*2} & u_6 = -i(a_1^2 + a_2^{*2}) \end{array} \tag{5.8}$$

whereas terms $u_{7,...,14}$ correspond to the XPM or Raman gain and they are defined as

$$\begin{array}{ccc} u_7 = a_1^* b_1 - a_2 b_2^* & u_8 = -(b_1 a_2 + b_2^* a_1^*) & u_9 = i(b_1 a_2 - a_1^* b_2^*) \\ u_{10} = -i(a_1^* b_1 + a_2 b_2^*) & u_{11} = a_1 b_2^* + b_1 a_2^* & u_{12} = a_1 b_1 - a_2^* b_2^* \\ u_{13} = -i(a_1 b_1 + a_2^* b_2^*) & u_{14} = i(a_1 b_2^* - a_2^* b_1) & \end{array} \tag{5.9}$$

At this point, the equations of motion for V_p and V_s are simplified by averaging and writing $\langle u_m u_n \rangle$ instead of $u_m u_n$. This is true due to the previous assumption that $\min(L_{NL}, L) >> L_C$. The ergodic theorem is also useful

$$\langle f(z) \rangle = \lim_{z \to \infty} \frac{1}{z} \int_0^z f(z') \partial z' \tag{5.10}$$

Before obtaining the equation to calculate $\langle u_m u_n \rangle$, the equations of motion for V_p and V_s are rewritten in the Stokes space ($\mathbf{S}^{(\mathrm{j})} = (S_1^{(j)}, S_2^{(j)}, S_3^{(j)})$) for j = s, p. And the power of the beams is described by $S_0^{(j)}$.

$$\begin{aligned} \pm \frac{\partial S^{(p)}}{\partial z} + \beta'(\omega_p) \frac{\partial S^{(p)}}{\partial t} &= \gamma(\omega_p)(S^{(p)} \times J_S^{(p)} S^{(p)} \\ + S^{(p)} \times J_x S^{(s)}) &+ \epsilon_p g_0 [s_0^{(s)} J_{R0} S^{(p)} + s_0^{(p)} J_R S^{(s)}] \end{aligned} \tag{5.11}$$

$$\begin{aligned} \frac{\partial S^{(s)}}{\partial z} + \beta'(\omega_s) \frac{\partial S^{(s)}}{\partial t} &= \gamma(\omega_s)(S^{(s)} \times J_S^{(s)} S^{(s)} \\ + S^{(s)} \times J_x S^{(p)}) &+ g_0 [s_0^{(p)} J_{R0} S^{(s)} + s_0^{(s)} J_R S^{(p)}] \end{aligned} \tag{5.12}$$

$$\begin{aligned} \pm \frac{\partial S_0^{(p)}}{\partial z} + \beta'(\omega_p) \frac{\partial S_0^{(p)}}{\partial t} &= \epsilon_p g_0 [J_{R0} S_0^{(s)} S_0^{(p)} \\ + J_{R1} S_1^{(s)} S_1^{(p)} + J_{R2} S_2^{(s)} S_2^{(p)} &+ J_{R3} S_3^{(s)} S_3^{(p)}] \end{aligned} \tag{5.13}$$

$$\begin{aligned} \frac{\partial S_0^{(s)}}{\partial z} + \beta'(\omega_s) \frac{\partial S_0^{(s)}}{\partial t} &= g_0 [J_{R0} S_0^{(s)} S_0^{(p)} \\ + J_{R1} S_1^{(s)} S_1^{(p)} + J_{R2} S_2^{(s)} S_2^{(p)} &+ J_{R3} S_3^{(s)} S_3^{(p)}] \end{aligned} \tag{5.14}$$

Where $J_S^{(j)}$, J_x, J_R are diagonal matrices that represents the contribution of SPM, XPM and Raman, respectively, with elements $J_S^{(j)} = \mathrm{diag}(J_{S1}^{(j)}, J_{S2}^{(j)}, J_{S3}^{(j)})$, $J_x = \mathrm{diag}(J_{x1}, J_{x2}, J_{x3})$, $J_R = \mathrm{diag}(J_{R1}, J_{R2}, J_{R3})$. These elements are different for the counter-propagating and the co-propagating interaction geometries and they are depended of the averages of the self-products and

cross-products. However, all the cross-products that are of interest to us turn out to be equal to zero. Similarly, terms of the form $Re(u_n)Im(u_n)$ also vanish. The values of the elements of $J_S^{(j)}$, J_x, J_R are

$$J_{S1}^{(j)} = \tfrac{1}{3}\langle Re(u_6^2)\rangle; \quad J_{S2}^{(j)} = -\tfrac{1}{3}\langle Re(u_6^2)\rangle; \quad J_{S3}^{(j)} = \tfrac{1}{3}[3\langle u_3^2\rangle - 1] \tag{5.15}$$

$$J_{x1} = \tfrac{2}{3}\langle Re(u_{10}^2 + u_{13}^2 - u_9^2 - u_{14}^2)\rangle; \quad J_{x2} = \tfrac{2}{3}\langle Re(u_{10}^2 + u_{14}^2 - u_9^2 - u_{13}^2)\rangle$$

$$J_{x3} = \tfrac{2}{3}\langle |u_9|^2 + |u_{14}|^2 - |u_{10}|^2 - |u_{13}|^2\rangle \tag{5.16}$$

$$J_{R1} = \langle Re(u_{14}^2 - u_{10}^2)\rangle; \quad J_{R2} = -\langle Re(u_{14}^2 + u_{10}^2)\rangle$$

$$J_{R3} = -\langle |u_{14}|^2 - |u_{10}|^2\rangle \tag{5.17}$$

$$J_{R0} = \langle |u_{14}|^2 + |u_{10}|^2\rangle \tag{5.18}$$

Basing on equations 5.7, the equations of motion of u_n consist on a set of linear equation and it is necessary to construct a generator to find the ensemble average of any function of these coefficients. A complete explanation of this process is found in [43, 131]. For the self-phase terms, the sets of linear equation take the form of

$$\frac{\partial}{\partial z}\begin{pmatrix} S_1 \\ S_2 \\ S_3 \\ \theta \end{pmatrix} = \begin{pmatrix} S_2 \\ -S_1 \\ 0 \\ 1 \end{pmatrix} g_\theta + \begin{pmatrix} 0 \\ \mp 2\triangle\beta(\omega_p)S_3 \\ \pm 2\triangle\beta(\omega_p)S_2 \\ 0 \end{pmatrix} \tag{5.19}$$

where g_θ is the white noise source and the group $\{S_1,\ S_2,\ S_3\}$ can be substituted by $\{u_1, u_2, u_3\}$, $\{Re(u_4), Re(u_5), Re(u_6)\}$ and $\{Im(u_4), Im(u_5), Im(u_6)\}$. The generator $(G(\psi))$ for any function $\psi(S_1, S_2, S_3, \theta)$ is

$$\frac{\partial < \psi(S_1, S_2, S_3, \theta) >}{\partial z} =< G(\psi) > \forall\psi(S_1, S_2, S_3, \theta) \tag{5.20}$$

where

$$G = L_c^{-1} \times \{S_2^2 \frac{\partial^2}{\partial S_1^2} + S_1^2 \frac{\partial^2}{\partial S_2^2} + \frac{\partial^2}{\partial \theta^2} - 2S_2 S_1 \frac{\partial^2}{\partial S_1 \partial S_2} + 2S_2 \frac{\partial^2}{\partial \theta \partial S_1} - 2S_1 \frac{\partial^2}{\partial \theta \partial S_2} - S_1 \frac{\partial}{\partial S_1} - S_2 \frac{\partial}{\partial S_2}\} \mp 2\triangle\beta(\omega_p) S_3 \frac{\partial}{\partial S_2} \pm 2\triangle\beta(\omega_p) S_2 \frac{\partial}{\partial S_3} \quad (5.21)$$

Our interest is on the groups $\{\langle u_1^2\rangle,\ \langle u_2^2\rangle,\ \langle u_3^2\rangle,\ \langle u_2 u_3\rangle\}$, $\{\langle Re^2(u_4)\rangle, \langle Re^2(u_5)\rangle, \langle Re^2(u_6)\rangle, \langle Re(u_5)Re(u_6)\rangle\}$ and $\{\langle Im^2(u_4)\rangle, \langle Im^2(u_5)\rangle, \langle Im^2(u_6)\rangle, \langle Im(u_5)Im(u_6)\rangle\}$, that are associated with $\{G_1,\ G_2,\ G_3,\ G_4\}$ with initial conditions given as (1, 0, 0, 0), (0, 1, 0, 0), and (0, 0, 1, 0), respectively. The differential equation are

$$\frac{\partial G_1}{\partial z} = -2L_c^{-1}(G_1 - G_2);\quad \frac{\partial G_2}{\partial z} = 2L_c^{-1}(G_1 - G_2) \mp 4\Delta\beta(\omega_p) G_4;$$
$$\frac{\partial G_3}{\partial z} = \pm 4\Delta\beta(\omega_p) G_4;\quad \frac{\partial G_4}{\partial z} = -L_c^{-1}(G_4) \pm 2\Delta\beta(\omega_p)(G_2 - G_3) \quad (5.22)$$

Similarly, for the term included in the cross-phase and Raman matrices, the sets of linear equation for $\{S_1,\ S_2,\ S_3,\ S_4\}$ equal to $\{Re(u_7),\ Re(u_8),\ Re(u_9),\ Re(u_{10})\}$, $\{Im(u_7),\ Im(u_8),\ Im(u_9),\ Im(u_{10})\}$, $\{Re(u_{11}),\ Re(u_{12}),\ Re(u_{13}),\ Re(u_{14})\}$ and $\{Im(u_{11}),\ Im(u_{12}),\ Im(u_{13}),\ Im(u_{14})\}$ take the form of

$$\frac{\partial}{\partial z}\begin{pmatrix} S_1 \\ S_2 \\ S_3 \\ S_4 \\ \theta \end{pmatrix} = \begin{pmatrix} S_2 \\ -S_1 \\ 0 \\ 0 \\ 1 \end{pmatrix} g_\theta + \begin{pmatrix} \triangle_\pm S_4 \\ \triangle_\mp S_3 \\ -\triangle_\mp S_2 \\ -\triangle_\pm S_1 \\ 0 \end{pmatrix} \quad (5.23)$$

Here $\triangle_{\pm} = (\pm\triangle\beta(\omega_p) - \triangle\beta(\omega_s))$. Consequently,

$$\frac{\partial < \psi(S_1, S_2, S_3, S_4, \theta) >}{\partial z} =< G(\psi) > \forall\psi(S_1, S_2, S_3, S_4, \theta) \tag{5.24}$$

where

$$\begin{aligned} G = L_c^{-1} \times \{S_2^2\frac{\partial^2}{\partial S_1^2} + S_1^2\frac{\partial^2}{\partial S_2^2} + \frac{\partial^2}{\partial\theta^2} - 2S_2S_1\frac{\partial^2}{\partial S_1\partial S_2} \\ +2S_2\frac{\partial^2}{\partial\theta\partial S_1} - 2S_1\frac{\partial^2}{\partial\theta\partial S_2} - S_1\frac{\partial}{\partial S_1} - S_2\frac{\partial}{\partial S_2}\} \\ -\triangle_{\pm}S_1\frac{\partial}{\partial S_4} + \triangle_{\pm}S_4\frac{\partial}{\partial S_1} + \triangle_{\mp}S_3\frac{\partial}{\partial S_2} - \triangle_{\mp}S_2\frac{\partial}{\partial S_3} \end{aligned} \tag{5.25}$$

We generate the necessary equations for the groups

$$\begin{aligned} \frac{\partial G_1}{\partial z} &= -2L_c^{-1}(G_1 - G_2) + 2\triangle_{\pm}G_6 \\ \frac{\partial G_2}{\partial z} &= 2L_c^{-1}(G_1 - G_2) + 2\triangle_{\mp}G_5 \\ \frac{\partial G_3}{\partial z} &= -2\triangle_{\mp}G_5 \\ \frac{\partial G_4}{\partial z} &= -2\triangle_{\pm}G_6 \\ \frac{\partial G_5}{\partial z} &= -\triangle_{\mp}(G_2 - G_3) - L_c^{-1}G_5 \\ \frac{\partial G_6}{\partial z} &= \triangle_{\pm}(G_4 - G_1) - L_c^{-1}G_6 \end{aligned} \tag{5.26}$$

where we associate $\{G_1, G_2, G_3, G_4, G_5, G_6\}$ with $\{\langle Re^2(u_7)\rangle, \langle Re^2(u_8)\rangle, \langle Re^2(u_9)\rangle, \langle Re^2(u_{10})\rangle, \langle Re(u_8)Re(u_9)\rangle, \langle Re(u_7)Re(u_{10})\rangle\}$, $\{\langle Im^2(u_7)\rangle, \langle Im^2(u_8)\rangle, \langle Im^2(u_9)\rangle, \langle Im^2(u_{10})\rangle, \langle Im(u_8)Im(u_9)\rangle, \langle Im(u_7)Im(u_{10})\rangle\}$, $\{\langle Re^2(u_{11})\rangle, \langle Re^2(u_{12})\rangle, \langle Re^2(u_{13})\rangle, \langle Re^2(u_{14})\rangle, \langle Re(u_{12})Re(u_{13})\rangle, \langle Re(u_{11})Re(u_{14})\rangle\}$ and $\{\langle Im^2(u_{11})\rangle, \langle Im^2(u_{12})\rangle, \langle Im^2(u_{13})\rangle, \langle Im^2(u_{14})\rangle, \langle Im(u_{12})Im(u_{13})\rangle, \langle Im(u_{11})Im(u_{14})\rangle\}$ with initial conditions as (1, 0, 0, 0, 0, 0), (0, 1, 0, 0, 0, 0), (0, 0, 1, 0, 0, 0) and (0, 0,

0, 1, 0, 0), respectively.

5.3 Co-propagating Raman polarizers

Hear, our goal is to explain the performance of Raman polarizers by the use of the mathematical model introduced above. A scheme of a co-propagating Raman polarizer is depicted in figure 5.2. This device is characterized by a low-PMD fiber, a polarized high-power Raman pump and a unpolarized input signal at the corresponding first-Stokes wavelength.

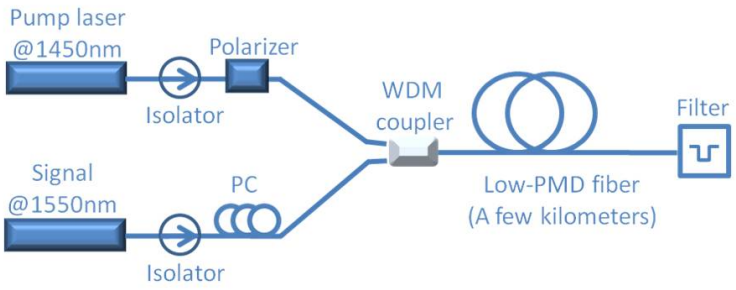

Figure 5.2: Scheme of a co-propagating Raman polarizer.

Equations 5.11-5.14 can be easily solved numerically, in particular in the copropagating configuration and undepleted pump regime, which is of interest to us here. Firstly, the value of J_s, J_x and J_R are calculated. We found that both SPM and XPM effects have virtually no impact on the performance of Raman polarizers operating in the undepleted pump regime. In contrast, the form of the Raman matrix is of paramount importance. The larger the coefficients on the diagonal, the stronger the PDG. For moderate values of the polarization-mode dispersion (PMD) coefficient, Raman diagonal terms take only appreciable values near the fiber input, as illustrated in figure 5.3. Therefore, the power of the pump beam is to be high, in order to provide significant amplification over the first few hundreds meters of the

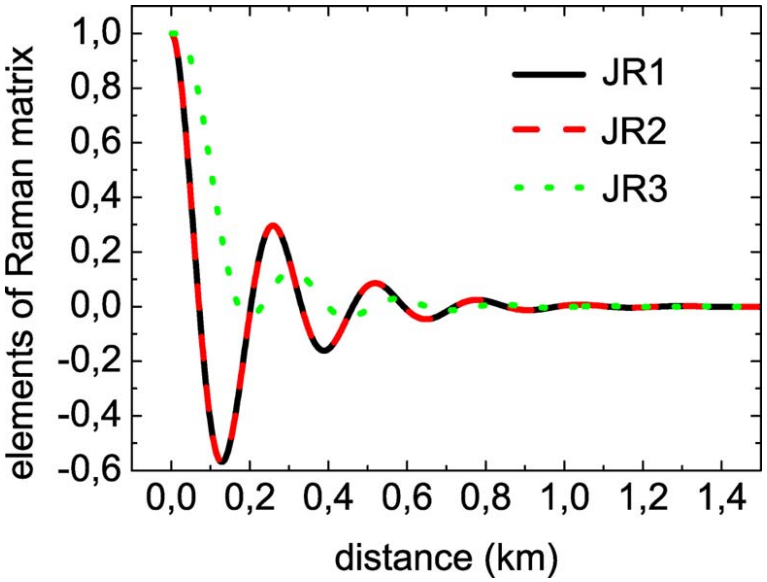

Figure 5.3: Elements of the Raman matrix as a function of distance in the fiber for $L_B(\omega_p) = 0.016$ km and $L_c = 0.05$ km.

fiber.

For analyzing the performance of Raman polarizers, there are three important parameters. The first one is the degree of polarization (DOP) of the outcoming signal, which is defined as

$$DOP = \frac{\sqrt{\langle S_1^{(s)}\rangle^2 + \langle S_2^{(s)}\rangle^2 + \langle S_3^{(s)}\rangle^2}}{S_0^{(s)}} \tag{5.27}$$

As such, the DOP is the average length of the output Stokes vector over the N realizations of the signal SOP (labeled by index) which are imposed at the input. We shall be dealing with scrambled beams, that is, with a set of N fully polarized beams, whose SOPs are uniformly (or randomly) distributed over the Poincaré sphere. Given that the average DOP of the scrambled signal is zero initially, we say that our goal is reached if the DOP of the output beam is close to unity. In this case, we shall refer to such Raman amplifiers as ideal Raman polarizers.

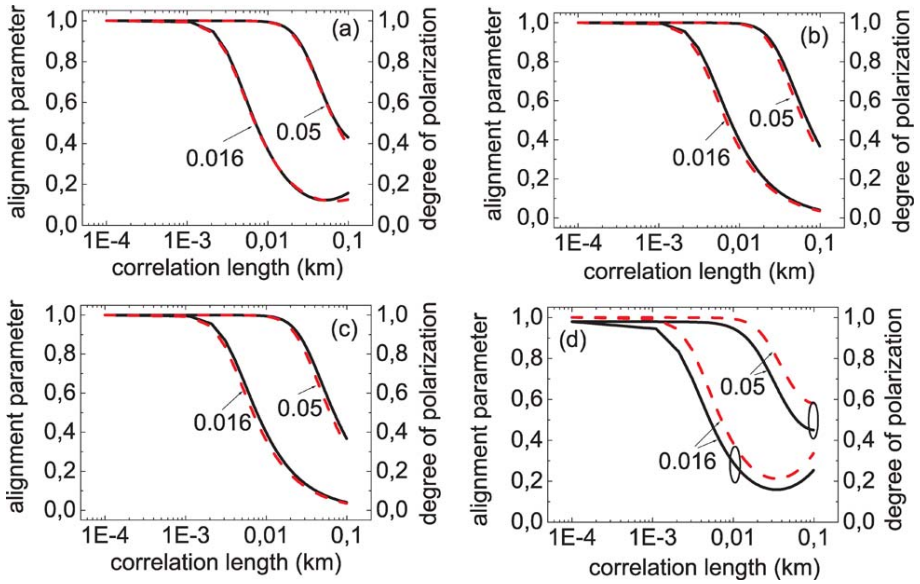

Figure 5.4: DOP of the signal beam (black, solid curve) and alignment parameter $A_{\uparrow\uparrow}$ (red, dashed curve) as a function of correlation length L_c for the four SOPs of the pump beam: (a) $(1/\sqrt{3})(1, 1, 1)$ (b) (1, 0, 0) (c) (0, 1, 0) (d) (0, 0, 1). The value of the birefringence length $L_B(\omega_p)$ is indicated on the plots in km. The two ellipses on plot (d) indicate one (of infinitely many) pair of points with equal PMD coefficients. Here and in figs. 5.5 and 5.6, the input signal power is 1 μW; input pump power, 8 W; $g_0 = 0.6$ $(W \cdot km)^{-1}$; $\gamma = 1(W \cdot km)^{-1}$; $\alpha = 0.2$ dB/km; and L =1.5 km.

The second issue is provided by the output signal SOP; namely, its relation to the pump SOP. We use the alignment parameter that measures the relative difference between these two SOPs. It is defined as

$$A_{\uparrow\uparrow} = \frac{\langle S_1^{(s)} S_1^{(p)} + S_2^{(s)} S_2^{(p)} + S_3^{(s)} S_3^{(p)} \rangle}{S_0^{(s)} S_0^{(p)}} \tag{5.28}$$

which is the cosine of the angle between the pump and the signal Stokes vectors, averaged over the ensemble of beams with random SOPs, which models the unpolarized signal beam. The third important quantity is the value of gain of the Raman polarizer.

We performed extensive simulations in a configuration where the pump

and signal beams co-propagate through a 1.5 km long fiber, and the pump power is set to 8 W and the input power of the signal beam is set to be equal to 1 μW. The DOP and alignment parameter are illustrated in figure 5.4 as function of the correlation length and the beat length. All four plots demonstrate that small correlation lengths and large beat lengths favor the efficiency of Raman polarizers. An important practical issue is the selection of fibers for Raman polarizers. The main parameter in this selection is the value of the PMD coefficient. In this respect, we found that for obtaining a signal DOP close to unity, the PMD coefficient should be less than 0.0145 $ps/\sqrt{(km)}$ for, say, 8 W of pump power. Nevertheless, we found that the PMD coefficient does not always provide full information about the fiber. For example, in figure 5.4(d), we can see that two fibers with equal PMD coefficients exhibit a different performance as Raman polarizers. In one case, the DOP is 0.25; in the other it is 0.45. For this reason, it is preferable to consider the beat and correlation lengths separately, rather than combining them into the single PMD coefficient, which for our model is expressed as $D_p = 2\sqrt{(2)}\pi\sqrt{(L_c)}/(L_B\omega_s)$.

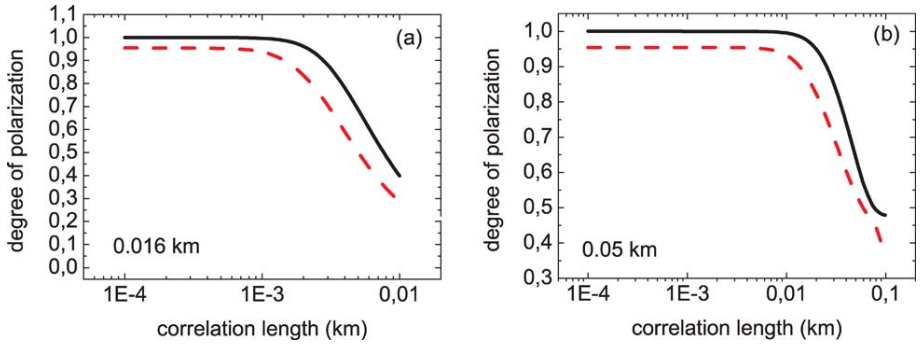

Figure 5.5: Maximum and minimum DOP of the signal beam. For each value of L_c, we perform a separate search for the pump SOPs that either maximize or minimize the DOP. The beat length is indicated on the plots in kilometers.

As for the alignment parameter, the hypothesis is that signal SOP is

always attracted to the pump SOP, this is true for the model of isotropic fibers, in which $J_{R1} = J_{R2} = J_{R2} = 1$. However, in randomly birefringent fibers, the equality, and even positivity, of the three elements is not always the case, as exemplified in the plot of figure 5.3. In these cases, it is remarkable that the signal SOP is attracted to an SOP that is different from that of the pump. In spite of this observation, we found that for ideal Raman polarizers the signal SOP, on average, is attracted to the pump SOP. Moreover, the performance of Raman polarizers (namely, DOP) sensitively depends on the pump SOP, as demonstrated in figure 5.5.

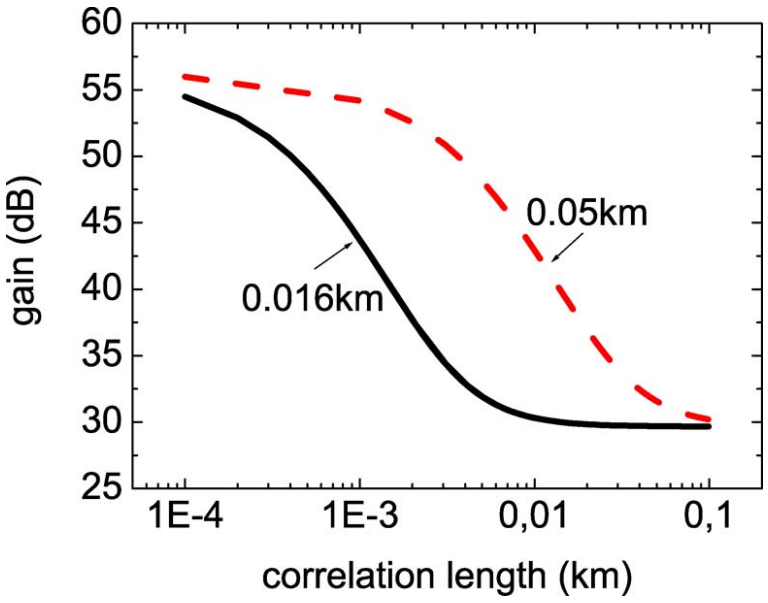

Figure 5.6: Average Raman polarizer gain as a function of the correlation length. The pump SOP is (1,0,0), and the signal beam is initially unpolarized.

The result of the third characteristic of Raman polarizers, Raman gain are depicted in figure 5.6. Even for a 1.5-km-long fiber with 8 W of pump power we may have an enormous 55 dB gain that is almost twice the gain of the same Raman amplifier but with a high value of the PMD coefficient. This means that Raman polarizers are simultaneously very efficient Raman

amplifiers. Such values of gain are obtained in the undepleted regime, i.e., for input signal powers in the microwatt range. For the miliwatt range, which is typical of telecom applications, the analysis necessarily enters the depleted pump regime, to which our theory can also be readily applied.

5.4 Counter-propagating Raman polarizers

In this section, we consider the case of counter-propagating Raman polarizers, where signal and pump are propagating in opposite directions. Now, the simulation parameters are pump power equal to 8 W, signal power of 0.1 mW and total length equal to 2 km. Again, the effect of SPM and XPM is firsly studied. The results for the XPM and the SPM vector are similar to the results in the previous example. The nonlinear polarization rotation which is due to the XPM interaction is very weak, and it has virtually no effect on the performance of Raman polarizers operating in the undepleted regime. The SPM effect for the signal beam has also no impact on the performance of Raman polarizers. First, this is because the diagonal elements of the SPM matrix vanish on first 100 m of the fiber for the practically relevant range of beat lengths and correlation lengths. Second, because the signal beam is too weak to experience a significant nonlinear self-interaction, especially near its input end. In contrast, the SPM effect can in principle be sizable for the pump beam. Given that the pump power is relatively high (8 W in our simulations), even the first 100 m are enough to perturb the pump SOP. However, these perturbations remain relatively small (of the order of 0.1%) for a pump power as high as 8 W.

Although in general the signal SOP is not attracted to the pump SOP, the analysis of the co-propagating configuration shows that in the regime when Raman amplifiers act as ideal Raman polarizers the output signal

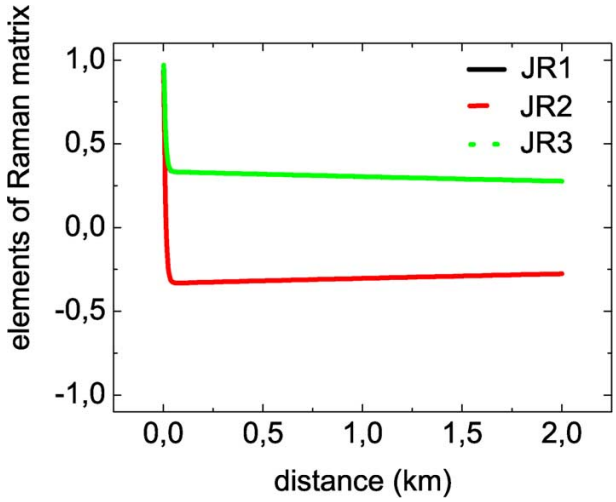

Figure 5.7: Elements of the Raman matrix as a function of distance in the fiber for $L_B(\omega_p) = 50$ m and $L_c = 1$ m. Note that $J_{R1} = J_{R2}$.

SOP is always almost perfectly aligned with the pump SOP. In the counter-propagating geometry the situation is totally different. In the regime when Raman amplifiers act as ideal Raman polarizers, the typical relation between the diagonal elements of the Raman matrix is as shown in figure 5.7. Thus, the first and the third components of the signal Stokes vector are attracted to the corresponding components of the pump Stokes vector, while the second components are repelled from each other. Therefore, whenever the pump SOP contains an appreciable admixture of the circular polarization, the signal SOP is never attracted to the pump SOP. For this reason the way to define the alignment parameter in this configuration is slightly different

$$A_{\uparrow\downarrow} = \frac{\langle S_1^{(s)} S_1^{(p)} - S_2^{(s)} S_2^{(p)} + S_3^{(s)} S_3^{(p)} \rangle}{S_0^{(s)} S_0^{(p)}} \tag{5.29}$$

The corresponding values of DOP and alignment parameter are shown in the four panels of figure 5.8. The results are sligthly worst than in co-propagating case. Altough a 2 km length polarizer has been simulated,

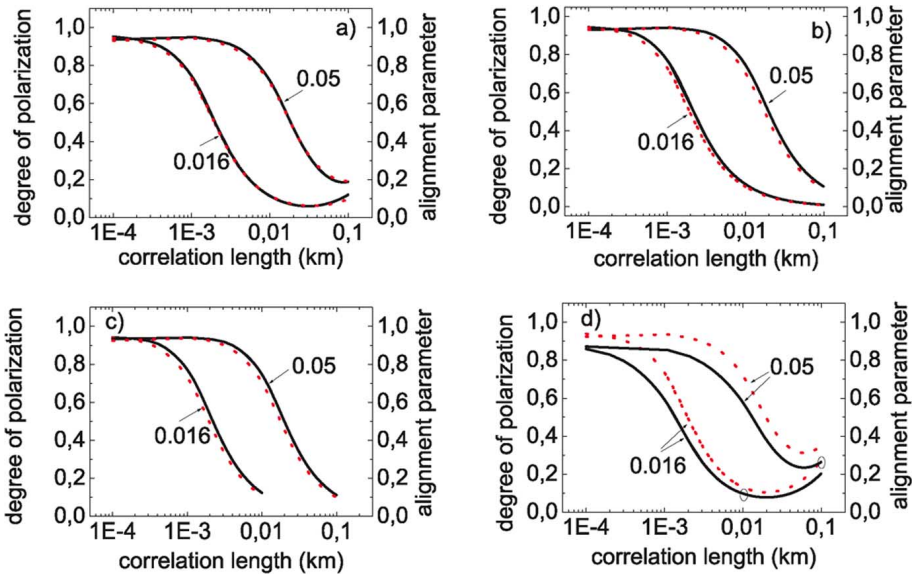

Figure 5.8: DOP of the signal beam (black, solid curve) and alignment parameter $A_{\uparrow\downarrow}$ (red, dashed curve) as a function of correlation length L_c for the four SOPs of the pump beam: (a) $(1/\sqrt{3})(1,\ 1,\ 1)$ (b) (1, 0, 0) (c) (0, 1, 0) (d) (0, 0, 1). The value of the birefringence length $L_B(\omega_p)$ is indicated on the plots in km. The two circles on plot (d) indicate one (of infinitely many) pair of points with equal PMD coefficients. Here and in figs. 5.9 and 5.11, the input signal power is 0.1 μW; input pump power, 8 W; $g_0 = 0.6(W\dot{k}m)^{-1}$; $\gamma = 1(W\dot{k}m)^{-1}$; $\alpha = 0.2$ dB/km; and L =2 km.

a signal DOP close to 1 is never obtained and, moreover, a lower PMD is required to keep this value above 0.9. Finally, the signal DOP is also dependent on the choice of the pump SOP. How sensitive is this dependence is demonstrated by figure 5.9.

A more detailed information on the signal SOP is available when basing ourselves on the following definitions of the alignment factors

$$A^{(i)}_{\uparrow\downarrow} = \langle \frac{S^{(s)}_i}{S^{(s)}_0} - \frac{S^{(p)}_i}{S^{(p)}_0} \rangle \tag{5.30}$$

where i=1,2,3. These expressions quantify the pairwise proximity of the components of the signal and pump Stokes vectors. In figure 5.10, the

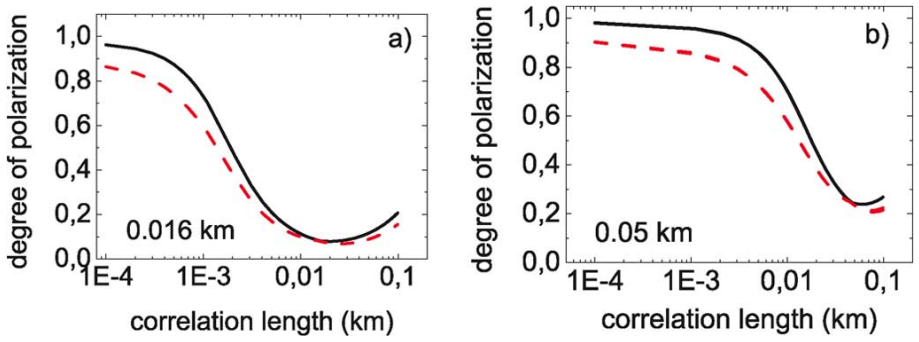

Figure 5.9: Maximum and minimum DOP of the signal beam. For each value of L_c, we perform a separate search for the pump SOPs that either maximize or minimize the DOP. The beat length is indicated on the plots in kilometers.

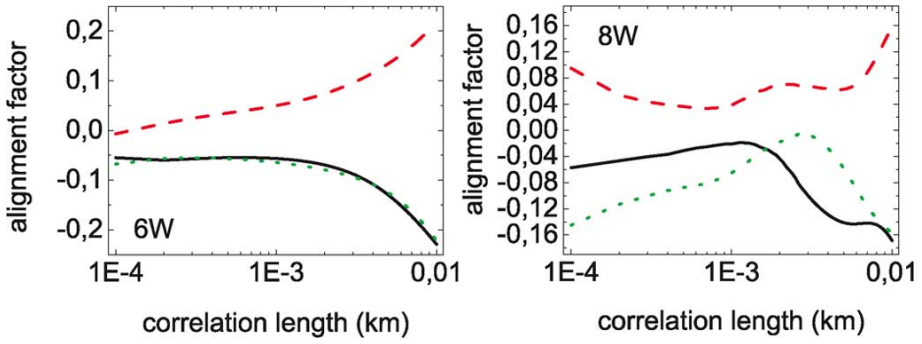

Figure 5.10: Alignment factors defined in equation 5.30: $A^{(1)}_{\uparrow\downarrow}$ (black solid), $A^{(2)}_{\uparrow\downarrow}$ (red dashed), $A^{(3)}_{\uparrow\downarrow}$(green dotted) as function of the correlation length for $L_B = 0.05$ km and for two values of the pump power: (a) 6 W; (b) 8 W.

values of this parameters are depicted for two different pump power. One may observe that the output signal SOP depends on the pump power.

Finally, let us consider the gain characteristics of Raman polarizers. Owing to their strong polarization-dependent gain, the gain of a Raman polarizer is sizably larger than that of typical polarization insensitive Raman amplifiers (i.e., with high PMD values or that use polarization scrambled pump beams), see figure 5.11. This result is similar to the co-propagating case and it means that Raman polarizers are simultaneously very efficient amplifiers.

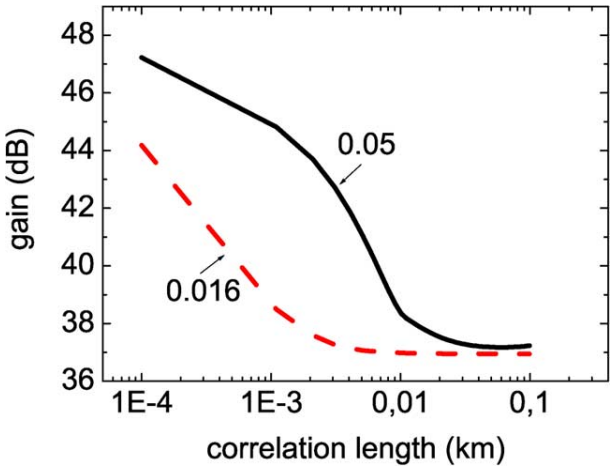

Figure 5.11: Average Raman polarizer gain as a function of the correlation length. The pump SOP is (1,0,0), and the signal beam is initially unpolarized. The value of the birefringence length $L_B(\omega_p)$ is indicated on the plots in km. Other parameters are the same as in figure 5.8, except that the input signal power is 1 μW.

5.5 Analytical simplification

The model presented previously can be numerical solved and it is also possible to write an exact analytical expression by mean of the Laplace transform. However, a very simple approximate analytical solutions for the copropagating Raman polarizers is presented here.

Elements of the SPolM tensor drop very fast and already vanish within the first 10 m of the fiber (see figure 5.12). Given that the length of the Raman devices exceeds 1 km, we can safely set

$$J_S = \mathrm{diag}(0, 0, 0) \tag{5.31}$$

The elements of the other two tensors also deceases with distance, how-

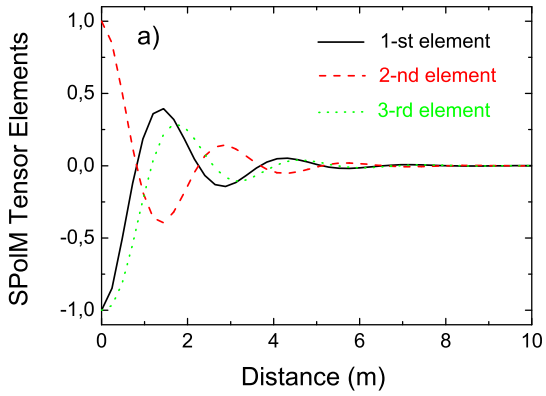

Figure 5.12: SPolM (J_{s1}, J_{s2}, J_{s3}). Parameters are: $L_c = 1$ m, $L_B(\omega_s) = 20$ m, $\omega_p - \omega_s = 13.2$ THz.

ever much slowly, for the co-propagating case namely as

$$J_X = -\frac{8}{9}\mathrm{diag}(1,1,1)\exp(-z/L_d) \tag{5.32}$$

$$J_R = \mathrm{diag}(1,1,1)\exp(-z/L_d) \tag{5.33}$$

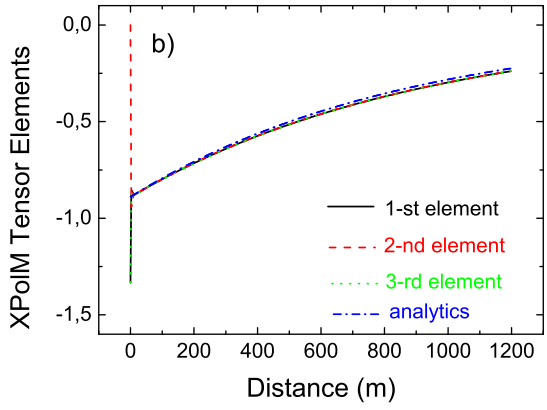

Figure 5.13: XPolM (J_{X1}, J_{X2}, J_{X3}). Same parameters.

where L_d is called the PMD diffusion length and it is defined from L_c and L_B: $L_d^{-1} = \frac{1}{3}(D_p\Delta\omega)^2$. Figures 5.13 and 5.14 show how well these

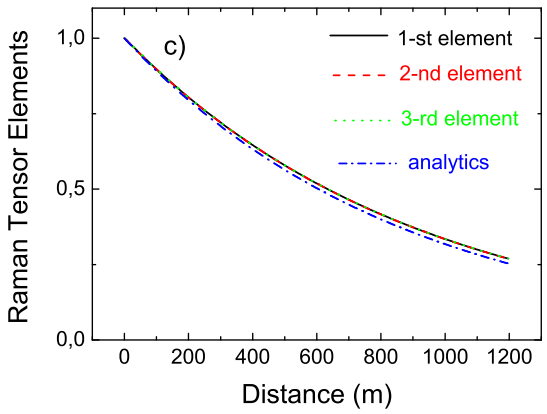

Figure 5.14: Raman tensors (J_{R1}, J_{R2}, J_{R3}). Same parameters.

analytical solutions reproduce the exact situation.

Thanks to this approximation in the limit when the polarizers operate $(L_d \to \infty)$, equation 5.12 is simplified to

$$\frac{\partial S^{(s)}}{\partial z} = -\bar{\gamma}(S^{(s)} \times S^{(p)}) + g_0/2[s_0^{(p)} S^{(s)} + s_0^{(s)} S^{(p)}] \tag{5.34}$$

with $\bar{\gamma} = \frac{8}{9}\gamma$. This equation includes two contributions. The XPolM contribution is a cross-phase modulation (XPM) part of the Manakov equation, in which the factor of $\frac{8}{9}$ appears as the result of averaging of fast stochastic polarization dynamics of each Stokes vector. Quite to the contrary, the Raman contribution appears exactly as in the case of isotropic fibers (i.e. in absence of the birefringence, and its stochasticity), because the mutual polarization scrambling of the relative orientations of the pump and Stokes vectors is very inefficient when the PMD diffusion length L_d is long. In other words, Raman amplification is insensitive to the absolute orientation of the individual SOPs of the signal and pump beams in the laboratory frame. It is however sensitive to their *mutual* orientation. In the case of standard

Raman amplifiers, the signal Stokes vector rotates rapidly around the pump Stokes vector, and therefore on average "feels" no polarization dependence. In the case of Raman polarizers, still the two vectors stochastically rotate in the laboratory frame, but they do it now in unison, so that their mutual orientation is almost "frozen".

To illustrate the performance of Raman polarizers, the pump Stokes vector is chosen to be aligned along its first component (without loss of generality): $\mathbf{S}^{(p)} = S_0^{(p)}(1,\,0,\,0)$. Then, we may write for the signal first Stokes component:

$$\partial_z S_1^{(s)} = (g_0/2) S_0^{(p)} \left[S_0^{(s)} + S_1^{(s)} \right] \tag{5.35}$$

If initially the signal Stokes vector is also aligned with its first component, then the signal amplification coefficient is g_0. This value should be contrasted to the value of $g_0/2$, which is characteristic to standard Raman amplifiers. The other two components of the signal Stokes vector are amplified less efficiently than the first component. Indeed, their equations of motion are:

$$\begin{aligned} \partial_z S_2^{(s)} &= -\bar{\gamma} S_0^{(p)} S_3^{(s)} + (g_0/2) S_0^{(p)} S_2^{(s)} \\ \partial_z S_3^{(s)} &= \bar{\gamma} S_0^{(p)} S_2^{(s)} + (g_0/2) S_0^{(p)} S_3^{(s)} \end{aligned} \tag{5.36}$$

Here, the gain is only $g_0/2$. These equations are solved analytically for the undepleted regime where $P \equiv S_0^{(p)}(z) =$const,

$$\begin{aligned} S_0^{(s)}(z) &= \frac{1}{2}\left[S_0^{(s)}(0) - S_1^{(s)}(0) \right] + \frac{1}{2}\left[S_0^{(s)}(0) + S_1^{(s)}(0) \right] \mathrm{e}^{g_0 P z} \\ S_1^{(s)}(z) &= -\frac{1}{2}\left[S_0^{(s)}(0) - S_1^{(s)}(0) \right] + \frac{1}{2}\left[S_0^{(s)}(0) + S_1^{(s)}(0) \right] \mathrm{e}^{g_0 P z} \end{aligned}$$

$$S_2^{(s)}(z) = \left[S_2^{(s)}(0)\cos(\bar{\gamma}Pz) - S_3^{(s)}(0)\sin(\bar{\gamma}Pz)\right]\mathrm{e}^{\frac{1}{2}g_0Pz} \tag{5.37}$$
$$S_3^{(s)}(z) = \left[S_2^{(s)}(0)\sin(\bar{\gamma}Pz) + S_3^{(s)}(0)\cos(\bar{\gamma}Pz)\right]\mathrm{e}^{\frac{1}{2}g_0Pz}$$

In order to calculate the DOP and alignment parameter, we shall calculate the mean quantities. We assume that the signal is initially unpolarized, so that $\langle S_1^{(s)}(0)\rangle = \langle S_2^{(s)}(0)\rangle = \langle S_3^{(s)}(0)\rangle = 0$. Then, at $z = L$, we get

$$\begin{aligned}
\langle S_0^{(s)}(L)\rangle &= \frac{1}{2}S_0^{(s)}(0)\left[1+\exp(g_0PL)\right] \\
\langle S_1^{(s)}(L)\rangle &= \frac{1}{2}S_0^{(s)}(0)\left[-1+\exp(g_0PL)\right] \\
\langle S_2^{(s)}(L)\rangle &= 0 \\
\langle S_3^{(s)}(L)\rangle &= 0
\end{aligned} \tag{5.38}$$

So, the signal SOP at the output is aligned with the pump SOP. The degree of polarization is,

$$\mathrm{DOP} = 1 - G^{-1} \tag{5.39}$$

where G has been defined as $G = \langle S_0^{(s)}(L)\rangle / S_0^{(s)}(0) = \frac{1}{2}\left[1+\exp(g_0PL)\right]$. The higher the gain, the larger the DOP. Already 20 dB gain is enough to get a DOP as high as 0.99.

The other important quantity which characterizes a Raman polarizer is the alignment parameter $A_{\uparrow\uparrow}$, defined as the cosine of the angle between the output signal SOP and the output pump SOP. The closer the alignment parameter to unity, the better the alignment of the output signal and pump Stokes vectors. In our simplification, we get

$$A_{\uparrow\uparrow} = \frac{\langle S_1^{(s)}(L)\rangle}{\langle S_0^{(s)}\rangle} = 1 - G^{-1} \tag{5.40}$$

Although this value coincides with the value of DOP, these two quantities

have different physical meanings as it is mentioned in other sections.

Finally, the measure of the polarization-dependent gain (PDG) is analyzed. Different SOPs of the signal beam experience different amplifications. The signal beam with a SOP parallel to the pump Stokes vector is amplified most efficiently, while the orthogonal polarization experiences no gain. Indeed, as it follows from the solution in equation 5.37, $G_{\max} = \exp(g_0 PL)$ and $G_{\min} = 1$. We introduce the PDG parameter Δ as $\Delta = G_{\max} - G_{\min}$, and get for the ideal Raman polarizer $\Delta = 2(G-1)$. The PDG parameter acquires high values for a high-gain Raman polarizer. Note that for an "ideal Raman amplifier" $\Delta = 0$.

The high value of the PDG parameter points out that along with the desirable property of strong re-polarization of the signal beam, this device is characterized by a high level of unwanted relative intensity noise (RIN). By varying the signal SOP at the input we get pronounced variations of the intensity at the output, even if the incoming beam had a steady intensity in time. In order to characterize the output power fluctuations, let us calculate the variance

$$\sigma_s^2 = \frac{\langle S_0^2(L)\rangle}{\langle S_0(L)\rangle^2} - 1 = (1 - G^{-1})^2/3 \tag{5.41}$$

For large G, $\sigma_s \approx 3^{-1/2} \approx 58\%$.This level of RIN may be detrimental for some optical devices, particularly nonlinear ones. The price to be paid is the totally stochastic signal SOP at the output fiber end.

A reasonable question to ask is whether it is possible for a Raman polarizer to keep the useful property of re-polarization and at the same time to suppress RIN down to an acceptable level. One solution are proposed in the next section.

Now, we focus on the counter-propagating case. As regarding the theory, one can repeat derivations with the opposite sign of z-derivative in the equa-

tion governing evolution of the pump beam. As shown in section 5.4, this reversing of the sign brings some changes in the components of the XPolM and Raman tensors. They become

$$J_X = -\frac{8}{9}\mathrm{diag}(1,-1,1)\exp(-z/L_d) \tag{5.42}$$

$$J_R = \frac{1}{3}\mathrm{diag}(1,-1,1)\exp(-z/L_d) \tag{5.43}$$

The presence of the factor $\frac{1}{3}$ in front of the Raman tensor immediately leads us to the conclusion that the counter-propagating Raman polarizer is significantly less effective in re-polarization than its co-propagating analog. In order to get similar performances we need either to increase the pump power or lengthen the fiber, or both. Let us evaluate the performance of this device.

First of all, we start with the solving the equation of motion in the undepleted-pump regime. We get

$$\begin{aligned}
S_0^{(s)}(z) &= \tfrac{1}{2}\left[S_0^{(s)}(0) - S_1^{(s)}(0)\right]\mathrm{e}^{\frac{1}{3}g_0Pz} + \tfrac{1}{2}\left[S_0^{(s)}(0) + S_1^{(s)}(0)\right]\mathrm{e}^{\frac{2}{3}g_0Pz} \\
S_1^{(s)}(z) &= -\tfrac{1}{2}\left[S_0^{(s)}(0) - S_1^{(s)}(0)\right]\mathrm{e}^{\frac{1}{3}g_0Pz} + \tfrac{1}{2}\left[S_0^{(s)}(0) + S_1^{(s)}(0)\right]\mathrm{e}^{\frac{2}{3}g_0Pz} \\
S_2^{(s)}(z) &= \left[S_2^{(s)}(0)\cos(\bar{\gamma}Pz) - S_3^{(s)}(0)\sin(\bar{\gamma}Pz)\right]\mathrm{e}^{\frac{1}{2}g_0Pz} \\
S_3^{(s)}(z) &= \left[S_2^{(s)}(0)\sin(\bar{\gamma}Pz) + S_3^{(s)}(0)\cos(\bar{\gamma}Pz)\right]\mathrm{e}^{\frac{1}{2}g_0Pz}
\end{aligned} \tag{5.44}$$

We immediately observe that the difference in amplification coefficients of the first Stokes component and the second (and third) Stokes component is given by $\frac{2}{3}g_0 - \frac{1}{2}g_0$. The contrast is much weaker than for the co-propagating case, where we had $g_0 - \frac{1}{2}g_0$. The average gain of the counter-propagating Raman polarizer is

$$G = \frac{1}{2}\left(\mathrm{e}^{\frac{2}{3}g_0PL} + \mathrm{e}^{\frac{1}{3}g_0PL}\right) \tag{5.45}$$

which is significantly smaller than for a Raman polarizer operating in the co-propagating configuration, although it is still larger than for an ideal Raman amplifier. For the same value of the product PL, the DOP for the counter-propagating configuration is also smaller:

$$\mathrm{DOP} = 1 - 2\left(\mathrm{e}^{\frac{1}{3}g_0 PL} + 1\right)^{-1} \approx 1 - \sqrt{2}G^{-1/2} \tag{5.46}$$

For $G = 20$ dB in the co-propagating case the DOP was as high as 99%, while in the counter-propagating configuration it is only 86%. For input unpolarized light, the alignment parameter coincides with the DOP.

The PDG parameter $\Delta = G_{\max} - G_{\min}$ is easily calculated, resulting in

$$\Delta = \frac{1}{2}\left(\mathrm{e}^{\frac{2}{3}gPL} - \mathrm{e}^{\frac{1}{3}gPL}\right) = \frac{1}{2}\left(1 + 2G - \sqrt{1+8G}\right) \tag{5.47}$$

Its value is considerably less in the co-propagating configuration, particularly for moderate values of gain. This observation again points to the relatively poorer performances of the counter-propagating Raman polarizer. At the same time, the RIN is expected to have a lower level. In order to demonstrate this, let us evaluate the variance of the signal intensity,

$$\sigma_s^2 = \frac{1}{3}\left[1 - 2\left(\mathrm{e}^{\frac{1}{3}gPL} + 1\right)^{-1}\right]^2 \tag{5.48}$$

5.6 Suppression of RIN for WDM transmission lines

At the output of the Raman polarizers, the beam acquires a high level of RIN, even if the initial unpolarized light had steady in time intensity. This RIN is directly caused by PDG, and should not be mistaken for other forms

of RIN arising, for example, from amplitude noise in the pump beam. The situation here is similar to the propagation of unpolarized light through a conventional passive polarizer, in which the output signal intensity will be dependent on the relation between the random state of polarization of the arriving signal and the polarization angle set in the polarizer.

One possible way to suppress this RIN is to operate the Raman polarizer in the depleted regime, as suggested in [132]. However, this method has some limitations when applied to telecom systems: (i) the method becomes ineffective for a pulse stream with low extinction ratio, because "zeros" are amplified in the undepleted regime and therefore experience stronger gain than "ones" which are amplified in the depleted regime, finally resulting in a severe degradation of the extinction ratio; (ii) while working perfectly for one channel, the method is not scalable to multi-channel (wavelength-division multiplexed (WDM)) operation, when the competition for gain of temporally overlapping pulses from different channels introduces its own RIN into each channel; (iii) the RIN ratio R defined as $R = \max(I)/\min(I)$ (where I is the output intensity of the "one" bit) and which characterizes the gap between the maximally and the minimally amplified "one", is very high, thereby pointing to the inevitable (though maybe rare) failure in device performance. Other alternatives used in the single-channel case include a more complex configuration with two-section fiber [133, 134].

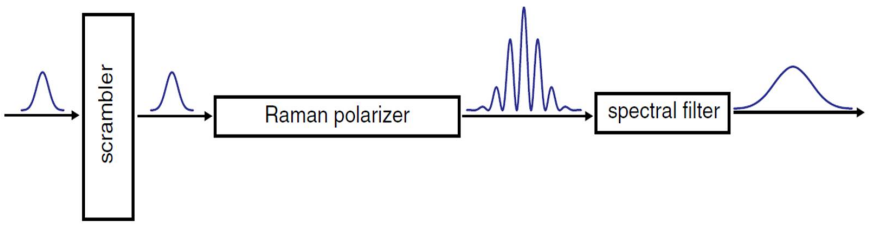

Figure 5.15: A sketch of the setup and the evolution of a pulse.

In the proposed configuration, the main idea here is to scramble the SOP of each bit prior to launching it into the Raman polarizer, as shown in the scheme of figure 5.15. We may bring each pulse from the sequence into a highly unpolarized state. At first sight it might seem counterintuitive that, in order to get a fully polarized light out of the device, we first need to depolarize it as strongly as possible. However, we are going to demonstrate shortly that such a polarization prescrambling indeed leads to a significant PDG-induced RIN suppression even for WDM signals. We shall consider the model of an ideal copropagating multichannel Raman polarizer. In this situation, the randomly birefringent telecom fiber turns into a perfectly isotropic fiber. The equations of motion for the signal and pump beams read as

$$(\partial_z - v_i^{(s)}\partial_t)\mathbf{S}_i^{(s)} = \bar{\gamma}\mathbf{S}_i^{(s)} \times \left(\mathbf{S}^{(p)} + \sum_{j=1,\neq i}^{N} \mathbf{S}_j^{(s)}\right) + (g_0/2) \left(S_0^{(p)}\mathbf{S}_i^{(s)} + S_{0i}^{(s)}\mathbf{S}^{(p)}\right) - \alpha_i \mathbf{S}_i^{(s)} \tag{5.49}$$

$$(\partial_z - v^{(p)}\partial_t)\mathbf{S}^{(p)} = \bar{\gamma}\mathbf{S}^{(p)} \times \sum_{j=1}^{N} \mathbf{S}_j^{(s)} + (g_0/2)\sum_{j=1}^{N} \epsilon_j^{(p)} \left(S_0^{(p)}\mathbf{S}_j^{(s)} + \mathbf{S}^{(p)}S_{0j}^{(s)}\right) - \alpha \mathbf{S}^{(p)} \tag{5.50}$$

where i, j label the channel number in the N-channels Raman polarizer. For quantifying the level of RIN, we introduce two quantities – the RIN ratio R_i and the normalized root-mean-square deviation (RMSD) of peak intensities. For the i-th channel, one has $\mathrm{CV(RMSD)}_i = \langle I\rangle^{-1}\sqrt{\langle (I - \langle I\rangle)^2\rangle}$ where $I_j = \max_j[S_0^{(s)}(L)]$ is the peak intensity of a pulse in the j-th "one" bit, and the average $\langle I\rangle \equiv M^{-1}\sum_{j=1}^{M} I_j$ is taken over all "one" bits in the sequence. In our numerical example we use a random sequence of 512 bits, therefore $M = 256$ on average. The smaller the CV(RMSD), the less pronounced the intensity fluctuations, and the better the performance of the

Raman polarizer. Nevertheless CV(RMSD) only characterizes the statistical properties of the device, as it tells us nothing about the occurrence of rare events. In this respect the RIN ratio R is more helpful. For evaluating this quantity we need to scan over *all* possible transmitted bits and take the absolute maximum and absolute minimum of the peak intensity of the "one" bits. As an estimate, we can say that when R is as high as E^{-1}, where E is the extinction ratio, then some events happen in which the output intensity of the "one" bit becomes comparable to the average output intensity of a "zero" bit, and a failure occurs, because of the indistinguishability of this "one" from a "zero". Overall, it is desirable to get R as close to unity as possible.

The input (at $z = 0$) SOP of an "one" bit of the signal beam in the Stokes space is defined as

$$S_1^{(s)} = S_0^{(s)}(t,\, 0)\sin[\phi_1 + \omega(t)]\cos[\phi_2 + \omega(t)] \tag{5.51}$$

$$S_2^{(s)} = S_0^{(s)}(t,\, 0)\sin[\phi_1 + \omega(t)]\sin[\phi_2 + \omega(t)] \tag{5.52}$$

$$S_3^{(s)} = S_0^{(s)}(t,\, 0)\cos[\phi_1 + \omega(t)] \tag{5.53}$$

The shape of $S_0^{(s)}(t,\, 0)$ is a Gaussian. The input phases ϕ_1 and ϕ_2 are constant across each bit slot, but differ from slot to slot. The modulation $\omega(t)$ describes the action of the polarization scrambler. We choose $\omega(t) = 8\pi t/T$, where T is the bit duration. We vary ϕ_1 and ϕ_2 from bit to bit in such a way that the overall degree of polarization (DOP) of our 512-bit long sequence at the input is as small as 0.02 even in the absence of the scrambler, thus representing a case of unpolarized light. At the output of the Raman polarizer, whose parameters are listed in the caption to figure 5.16, the DOP becomes as large as 0.997 in all simulation runs presented here.

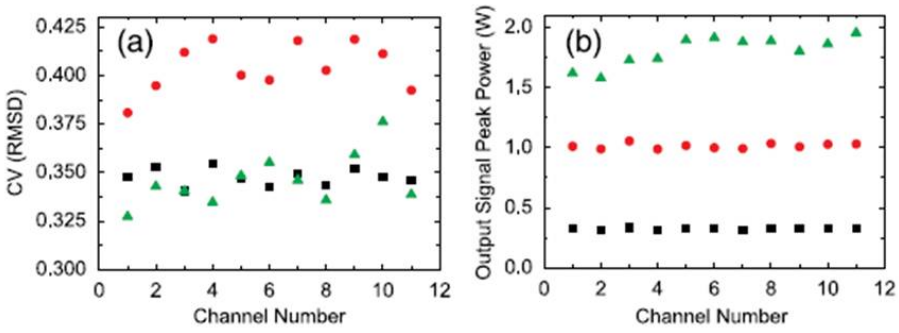

Figure 5.16: For an 11-channel Raman polarizer: a) CV(RMSD) and b) average output signal peak power of "one" bits. The result are in three regime: undepleted regime with no walk-off (black squares); depleted regime with no walk-off (red circles); depleted regime with walk-off (green triangles). Parameters are $\gamma = 1$ (W·km)$^{-1}$; $g = 0.6$ (W·km)$^{-1}$; linear losses 0.2 dB/km; input pump power $P = 8$ W; input signal power: 1 mW (10 mW) in the undepleted (depleted) regime; fiber length $L = 1.5$ km; $N = 11$; $\lambda^{(s)} = 1.55$ μm; $\lambda^{(p)} = 1.45$ μm; the pulse shape is Gaussian with FWHM= 8.33 ps; duty cycle 0.33; bit slot 25 ps; $[v^{(s)}]_j^{-1} = [v^{(p)}]^{-1} + \Delta\beta j$, $j = 1, \ldots, 11$, with $\Delta\beta = 0$ for no walk-off regime, $\Delta\beta = 2.4$ ps/km for regime with walk-off. The spectral filter is modeled as $\exp[(-1/2)\omega^2 T_f^2]$ with $T_f = 2.1$ ps.

This observation indicates that the Raman polarizer perfectly performs its main function – the re-polarization of light.

Let us solve equation 5.49-5.50 in the regime of undepleted pump, in the absence of linear losses, and neglecting nonlinear cross-polarization modulation effects (i.e. setting $\bar{\gamma} = 0$). In this regime all channels are equivalent and for each channel we can write $S_1^{(s)}(L) = \frac{1}{2}(G+1)S_1^{(s)}(0) + \frac{1}{2}S_0^{(s)}(0)(G-1)$ where $G = \exp(gPL)$ with $P = S_0^{(p)}(0)$ as the pump power. Note that we write down only the solution for $S_1^{(s)}$, as it is this component of the signal Stokes vector which largely dominates at the output (the other two components are not of interest to us because they grow much slower, i.e., $\propto \exp(gPL/2)$).

In the absence of pre-scrambling, the SOP does not change across the bit

and it is easy to find both maximum and minimum for $|S_1^{(s)}(L)| \approx S_0^{(s)}(L)$: $\max[S_1^{(s)}(L)] = GS_0^{(s)}(0)$, and $\min[S_1^{(s)}(L)] = -S_0^{(s)}(0)$. So, $R = G$. The maximum is realized when the input signal SOP is aligned with the pump SOP, while the minimum occurs when these two SOPs are orthogonal.

In presence of pre-scrambling, the SOP evaluation becomes involved. Moreover, the value of R starts to depend on the width of the spectral filter and on the specific way how the scrambling is implemented. For our choice of parameters we numerically scanned over all ϕ_1 and ϕ_2 and obtained $\max[S_1^{(s)}(L)] \approx 0.6GS_0^{(s)}(0)$ and $\min[S_1^{(s)}(L)] \approx 0.2GS_0^{(s)}(0)$ for $G \gg 1$, resulting in $R = 3$. This result means that the peak intensity of the output signal never drops below 50% and never jumps above 50 % with respect to its average level.

More information about the statistical characteristics of the Raman polarizer can be obtained via simulation of the average peak intensity and the CV(RMSD). The results are shown in figure 5.16. As a reference, we may note that the CV(RMSD)= 0.456 (average over all channels) for the undepleted pump regime without pre-scrambling. When the pre-scrambling is introduced, the CV(RMSD) drops down to 0.341, see figure 5.16(a). Therefore intensity fluctuations are significantly suppressed by the bit-synchronous polarization scrambler. This leads to a corresponding decrease of the bit-error-rate (BER) of a pseudo-random-bit-sequence after the Raman polarizer when pre-scrambling is used. Consider for example the signal in the first channel out of an 11-channel WDM comb with an optical-signal-to-noise ratio of 20 dB. By feeding our signal into a direct detection receiver using the Chi2 estimation method with inter-symbol interference correction, we numerically estimated that the BER at the Raman polarizer output decreases from 7.2×10^{-4} down to 2.6×10^{-5} when pre-scrambling is applied.

In the depleted pump regime the amount of the walk-off (understood here as the dependence of the group velocity on the channel number/wavelength) which is present in the system as a result of group velocity dispersion starts to play an important role. This occurs on two different scales: on the one hand the signals in different channels move at slightly different speeds, which means that ones in different channels are not depleting the pump simultaneously; on the other, the pump moves faster than the signal as a whole, which reduces the depletion by allowing the signal to be amplified by an undepleted section of the pump beam. In the example shown in figure 5.16 the average peak power almost doubles in the presence of walk-off when compared to the case of no walk-off, see figure 5.16(b). The walk-off suppression of the competition of channels for the gain is reflected in the CV(RMSD), which remains at the minimum level [0.346, obtained by averaging the CV(RMSD) over all channels], see figure 5.16(a). This observation should be compared to the performance of the same Raman polarizer, but without pre-scrambling. In this case in the depleted regime CV(RMSD)= 0.443 with walk-off and 0.488 with no walk-off, where both values are obtained by averaging over all channels.

5.7 Conclusions

In this chapter, a general theory for describing the interaction of two optical beams in randomly birefringent fibers via Kerr and Raman effects has been developed. This theory is valid for almost all practically relevant situations and it consumes less resource in terms of computational time than similar theories. The only assumption is that nonlinear length and total length is much longer than the correlation length, that it is true for both Raman amplifiers and Raman polarizers. It has been applied to analyze

the performance of Raman polarizers in the undepleted regime, although it is also applicable to the depleted regime. Three main characteristics has been identified: the DOP of the outcoming signal beam, the relationship between its SOP and the pump SOP and the amplifier gain. A comparison between different configurations shows the conterpropagating case is more demanding, as it requires a 2 km length fiber whose D_p below 0.008 ps/$\sqrt{(km)}$ for getting DOP above 0.9. Whereas DOPs as high as 0.99 are obtained for a as large as 0.014 ps/$\sqrt{(km)}$ with only a 1.5 km long fiber using the co-propagating case. This theory can be simplified in order to obtain an analytical model that is able to predict the main parameters including the variance of the RIN noise produced by PDG. In the last section, we have suggested a method to suppress this RIN. It consists on the use of a bit-synchronous polarization scrambler before the raman polarizer and a spectral filter after it.

Chapter 6

Conclusions and future works

6.1 Conclusions

This thesis has been devoted to the study of different aspects and applications of the Raman effect in optical fiber. We have divided our results into three clearly differentiated sections:

In the first results section we have studied from a theoretical standpoint the mechanisms of RIN transfer from pump laser to amplified signals in different URFL architectures, including random distributed fiber lasers. We have developed a precise model for the prediction of the RIN transfer function and studied the conditions under which this problem can be controlled and minimised, so it does not impede the application of ultralong lasers to long haul communications and long span sensors. We have performed a comparison of between the potential performances of cavity URFLs and RDFLs, showcasing their differences, and reached the conclusion that in quasi-lossless transmission applications, RIN transfer is generally lower in cavity URFLs than in their reflectorless counterparts.

In the second results section, three different applications of Raman am-

plification in optical fiber in the areas of telecommunication and sensing have been studied. Our main conclusions from this section can be summarized as:

- We have experimentally confirmed that, as predicted by theoretical models, the use of distributed amplification using URFL in telecommunication reduces the accumulation of ASE noise in comparison with lumped amplification schemes based on EDFA. This improvement is particularly relevant for transmission distances longer than 600 Km. Using DPSK coding schemes and 8 transmission channels, this improvement in ASE noise performance does not bring with it a clear improvement in terms of BER, due to the presence of RIN noise from the Raman pumps to the signal. This results showcases the need for low-RIN pumps in order to obtain the maximum possible performance of URFLs. However, the reduced ASE in the URFL configuration translates into a lower average signal power requirement and reduced power excursion when compared to an EDFA scheme with the same BER performance. This suggests that URFL configurations should have the edge in systems in which nonlinearities are the main source of impairment.

- We have numerically studied the performance of BOTDA assisted by Raman amplification using both cavity URFL and RDFL configurations. The very high pump power requirements of RDFLs represents a very serious disadvantage for their application. In addition, cavity URFLs also produce less broadening due to SPM, and display better RIN performance except for very long spans. From our results we can conclude that in most of the practical situations, the use of RDFL in

BOTDA applications can not be recommended.

- Finally, the use of Raman amplification for the extension of loop length and increase of sensitivity in Sagnac fiber optic gyroscopes has been proposed. Here, first-order bidirectional amplification, cavity URFLs and RDFLs were considered as possible configurations for the amplification scheme. The introduction of ASE noise due to the presence of amplification has been shown to be negligible, whereas the nonlinear phase shift due to non-reciprocities between optical paths has been detected as the main impairment associated to this kind of sensors. Numerical simulation allows for an estimate of these non-reciprocities, leading to the conclusion that a loop extension of the order of 5 times could be possible for a Raman-assisted Sagnac gyroscope, with an equivalent increase of sensitivity.

Finally, the third section focuses on the study of PMD in Raman amplifiers and the development of the first theoretical model for the recently demonstrated nonlinear Raman polarizer. We have presented a mathematical model able to predict the evolution of the state of polarization of an optical signal which for the first time includes all relevant nonlinear effects, i.e. SPM, XPM and Raman scattering. Furthermore, the model can be successfully simplified into an analytical version that is applicable to most situations of practical interest.

6.2 Future works

Although there are multiple possibilities for continuing and extending the work detailed in this thesis, two of them stand out, that are currently in progress. The experimental development of an amplified Sagnac interferom-

eter and a spun-finer Raman polarizer.

Prior to the implementation of a Raman-assisted FOG, a 5km length Sagnac sensor has been built. The device was used to measure the velocity of rotation of the earth in order to calibrate it. Variations of the phase of the interference were detected by means of a oscilloscope and a lock-in amplifier. However the work is still in progress due to unexpected delays in the arrival of the equipment necessary for the experiments to be carried out. Important issues to take into account in order to maximize the sensitivity will be the reduction of non-reciprocities due to the Shupe effect and external vibrations, as well as the efficient depolarization of the signal.

Regarding the work on fiber polarizers, our group has recently acquired 2km of custom-designed spun fiber. In this kind of fibers, birefringence is made very low by means of spinning the fiber preform during drawing. Our models predict that this kind of fiber can provide an ideal medium for Raman polarization attraction and experiments are on the works.

Bibliography

[1] G. P. Agrawal, *Fiber-optic communications systems*. John Wiley and Sons, Inc., third ed., 2002.

[2] G. P. Agrawal, *Nonlinear fiber optics*. Academic Press, third ed., 2001.

[3] D. Koenig, "Telegraphs and telegrams in revolutionary France," *Scientific Monthly*, p. 431, 1944.

[4] T. Maiman, "Stimulated optical radiation in ruby," *Nature*, vol. 187, no. 4736, pp. 493–494, 1960.

[5] K. C. Kao and G. A. Hockham, "Dielectric-fibre surface waveguides for optical frequencies," *Proceedings of the IEEE*, vol. 113, no. 7, pp. 1151–1158, 1966.

[6] F. Kapron, D. Keck, and R. Maurer, "Radiation losses in glass optical waveguides," *Applied Physics Letters*, vol. 17, no. 10, pp. 423–425, 1970.

[7] I. Hayashi, M. B. Panish, P. Foy, and S. Sumski, "Junction lasers which operate continuously at room temperature," *Applied Physics Letters*, vol. 17, no. 3, pp. 109–111, 1970.

[8] E. Desurvire, J. Simpson, and P. Becker, "High-gain erbium-doped traveling-wave fiber amplifier," *Optics Letters*, vol. 12, no. 11, pp. 888–890, 1987.

[9] C. Menadier, C. Kissenger, and H. Adkins, "The fotonic sensor," *Instruments and Control Systems*, vol. 40, p. 114, 1967.

[10] J. A. Bucaro, H. D. Dardy, and E. F. Carome, "Fibre optic hydrophone," *J. Acoust. Soc. Amer.*, vol. 52, no. 5, p. 1302, 1977.

[11] E. Snitzer, "Apparatus for controlling the propagation characteristics of coherent light within an optical fiber," *U.S. Patent 3 625 589*, 1971.

[12] V. Vali and R. W. Shorthill, "Fibre ring interferometer," *Applied Optics*, vol. 15, no. 5, pp. 1099–1100, 1976.

[13] A. J. Rogers, "P-OTDR: A technique for the measurement of field distributions," *Applied Optics*, vol. 20, no. 6, pp. 1060–1074, 1981.

[14] A. Smekal, "Zur quantentheorie der dispersion," *Naturwissenschaften*, vol. 11, no. 43, pp. 873–875, 1923.

[15] C. V. Raman and K. Krishnan, "A new type of secondary radiation," *Nature*, vol. 121, pp. 501–502, 1928.

[16] G. Landsberg and L. Mandelstam, "Uber die lichtzerstreuung in kristallen," *Zeitschrift für Physike*, vol. 50, no. 11, pp. 769–780, 1928.

[17] R. H. Stolen, "Nonlinearity in fiber transmission," *Proceedings of the IEEE*, vol. 68, no. 10, pp. 489–524, 1980.

[18] J. Bouteiller, K. Brar, and C. Headley, "Quasi-constant signal power transmission," *Proceedings of European Conference on Optical Communications (ECOC 2002)*, no. S03.04, 2002.

[19] T. Okuno, T. Tsuzaki, and M. Nishimura, "Novel optical hybrid line configuration for quasi-lossless transmission by distributed Raman amplification," *IEEE Photonics Technology Letters*, vol. 13, no. 8, pp. 806–808, 2001.

[20] J. D. Ania-Castañón, "Quasi-lossless transmission using second-order Raman amplification and fibre bragg gratings," *Optics Express*, vol. 12, no. 18, pp. 4372–4377, 2004.

[21] J. D. Ania-Castañón, T. J. Ellingham, R. Ibbotson, X. Chen, L. Zhang, and S. K. Turitsyn, "Ultralong Raman fiber lasers as virtually lossless optical media," *Physical Review Letters*, vol. 96, no. 2, p. 23902, 2006.

[22] T. Ellingham, J. D. Ania-Castañón, R. Ibbotson, X. Chen, L. Zhang, and S. Turitsyn, "Quasi-lossless optical links for broad-band transmission and data processing," *IEEE Photonics Technology Letters*, vol. 18, no. 11, pp. 268–270, 2006.

[23] V. Karalekas, J. D. Ania-Castañón, P. Harper, and S. Turitsyn, "Ultra-long Raman fibre laser transmission links," *11th International Conference on Transparent Optical Networks (ICTON '09)*, pp. 1–4, 2009.

[24] L. Barker, A. El-Taher, M. Alcon-Camas, J. D. Ania-Castañón, and P. Harper, "Extended bandwidth for long haul DWDM transmission using ultra-long Raman fiber lasers," *Proceedings of European Conference on Optical Communications (ECOC 2010)*, no. P04.14, 2010.

[25] S. Martín-López, M. Alcon-Camas, F. Rodríguez, P. Corredera, J. D. Ania-Castañón, L. Thévenaz, and M. González-Herráez, "Brillouin

optical time-domain analysis assisted by second-order Raman amplification," *Optics Express*, vol. 18, no. 18, pp. 18769–18778, 2010.

[26] S. K. Turitsyn, S. A. Babin, A. E. El-Taher, P. Harper, D. V. Churkin, S. I. Kablukov, J. D. Ania-Castañón, V. Karalekas, and E. V. Podivilov, "Random distributed feedback fibre laser," *Nature Photonics*, vol. 4, pp. 231–235, 2010.

[27] H. Martins, M. B. Marques, and O. Frazao, "300 km-ultralong Raman fiber lasers using a distributed mirror for sensing applications," *Optics Express*, vol. 19, no. 19, pp. 18149–18154, 2011.

[28] J. D. Colladon, "Sur les réflexions dún rayon de lumière à lìntérieur dúne veine liquide parabolique," *Comptes Rendus*, vol. 15, pp. 800–802, 1842.

[29] J.Tyndall, "Notes of a course of nine lectures on light delivered at the royal institution of great britain," 1870.

[30] J. Wells, "Hair light guide," *Nature*, vol. 338, p. 23, 1989.

[31] A. Ghatak and K. Thyagarajan, *An introduction to fiber optics*. Cambridge University Press, first ed., 1998.

[32] G. Keiser, *Optical fiber communications*. McGraw Hill, third ed., 2007.

[33] J. Senior., *Optical fibre communication: principle and practice*. Prentice Hall, first ed., 2007.

[34] P. Russell, "Photonics crystal fibers," *Science*, vol. 299, pp. 358–362, 2003.

[35] "G.651.1: Characteristics of a 50/125 μm multimode graded index optical fibre cable for the optical access network," *http://www.itu.int/rec/T-REC-G.651.1-200707-I/*, 2007.

[36] "G.652: Characteristics of a single-mode optical fibre and cable," *http://www.itu.int/rec/T-REC-G.652-200911-I*, 2009.

[37] T. Miya, Y. Terunuma, T. Hosaka, and T. Miyoshita, "Ultimate low-loss single-mode fibre at 1.55 μm," *Electronics Letters*, vol. 15, pp. 106–108, 1979.

[38] P. Diament, *Wave transmission and fiber optics.* Macmillan, first ed., 1990.

[39] A. Snyder and J. D. Love, *Optical waveguide theory.* Chapman and Hall, first ed., 1983.

[40] A. Galtarossa and C. R. Menyuk, *Polarization mode dispersion.* Springer, first ed., 2004.

[41] I. P. Kaminow, "Polarization in optical fibers," *IEEE Journal of Quantum Electronics*, vol. 17, pp. 15–22, 1981.

[42] P. K. A.Wai and C. R. Menyuk, "Polarization decorrelation in optical fibers with randomly varying birefringence," *Optics Letters*, vol. 19, pp. 1517–1519, 1994.

[43] P. K. A.Wai and C. R. Menyuk, "Polarization mode dispersion, decorrelation and diffusion in optical fibers with randomly varying birefringence," *Journal of Lightwave Technology*, vol. 14, pp. 148–157, 1996.

[44] M. Born and R. Oppenheimer, "Zur quantentheorie der molekeln," *Annalen der Physik*, vol. 389, pp. 457–484, 1927.

[45] D. A. Kleinman, "Nonlinear dielectric polarisation in optical media," *Physical Review*, vol. 162, pp. 1977–1979, 1962.

[46] P. V. Mamyshev and S. V. Chernikov, "Ultrashort-pulse propagation in optical fibers," *Optics Letters*, vol. 15, no. 19, pp. 1076–1078.

[47] J. Subias, J. Pelayo, R. Alonso, F. Villuendas, and C. Heras, "Electrostriction-free n2 measurement in single-mode optical fibers based on nonlinear polarization evolution," *Journal of the Optical Society of America B*, vol. 19, pp. 390–394, 2002.

[48] R. H. Stolen and C. Lin, "Self-phase-modulation in silica optical fibers," *Physical Review A*, vol. 17, pp. 1448–1453, 1978.

[49] A. Hasegawa and F. Tappert, "Transmission of stationary nonlinear optical pulses in dispersive dielectric fibers. I. Anomalous dispersion," *Applied Physics Letters*, vol. 23, pp. 142–144, 1973.

[50] L. F. Mollenauer, R. H. Stolen, and J. P. Gordon, "Experimental observation of picosecond pulse narrowing and solitons in optical fibers," *Physical Review Letters*, vol. 45, pp. 1095–1098, 1980.

[51] M. Shtaif, "Analytical description of cross-phase modulation in dispersive optical fibers," *Optics Letters*, vol. 23, pp. 1191–1193, 1998.

[52] G. P. Agrawal, P. L. Baldeck, and R. R. Alfano, "Analytical description of cross-phase modulation in dispersive optical fibers," *Physical Review A*, vol. 40, pp. 5063–5072, 1989.

[53] J. A. Armstrong, N. Bloembergen, J. Ducuing, and P. S. Pershan, "Interactions between light waves in a nonlinear dielectric," *Physical Review*, vol. 127, p. 1918.

[54] R. W. Boyd, *Nonlinear optics*. Academic Press, first ed., 1992.

[55] J. Hansryd, P. Andrekson, M. Westlund, J. Li, and P. Hedekvist, "Fiber-based optical parametric amplifiers and their applications," *Selected Topics in Quantum Electronics*, vol. 8, p. 506.

[56] R. Stolen and J. E. Bjorkholm, "Parametric amplification and frequency conversion in optical fibers," *IEEE Journal of Quantum Electronics*, vol. 18, p. 1062.

[57] G. Cappellini and S. Trillo, "Third-order three-wave mixing in single-mode fibers: exact solutions and spatial instability effects," *Journal of the Optical Society of America B*, vol. 8, p. 824.

[58] P. Hansen, L. Eskildsen, A. Stentz, T. Strasser, J. Judkins, J. DeMarco, R. Pedrazzani, and D. DiGiovanni, "Rayleigh scattering limitations in distributed Raman pre-amplifiers," *IEEE Photonics Technology Letters*, vol. 10, pp. 159–161, 1998.

[59] S. A. E. Lewis, S. V. Chernikov, and J. R. Taylor, "Characterization of double Rayleigh scatter noise in Raman amplifiers," *IEEE Photonics Technology Letters*, vol. 23, pp. 528–530, 2000.

[60] E. Woodbury and W. Ng, "Ruby laser operation in the near IR," *Proc. IRE.*, vol. 50, p. 2347.

[61] R. Y. Chiao, C. H. Townes, and B. P. Stoicheff, "Stimulated Brillouin scattering and coherent generation of intense hypersonic waves," *Physical Review Letters*, vol. 12, p. 592.

[62] R. H. Stolen, E. P. Ippen, and A. R. Tynes, "Raman oscillation in glass optical waveguide," *Applied Physics Letters*, vol. 20, pp. 62–64, 1972.

[63] R. Shuker and R. Gammon, "Raman scattering selection rule breaking and the density of states in amorphous materials," *Physical Review Letters*, vol. 25, p. 222.

[64] E. P. Ippen and R. H. Stolen, "Stimulated Brillouin scattering in optical fibers," *Applied Physics Letters*, vol. 21, pp. 539–541, 1972.

[65] R. G. Smith, "Optical power handling capacity of low loss optical fibers as determined by stimulated Raman and Brillouin scattering," *Applied Optics*, vol. 11, pp. 2489–2494, 1972.

[66] R. A. Fisher, *Optical phase conjugation.* Academic Press, first ed., 1983.

[67] J. C. Simon, "Semiconductor laser amplifier for single mode optical fiber communications," *Journal of Optical Communications*, vol. 4, p. 51.

[68] M. J. Connelly, *Semiconductor optical amplifiers.* Kluwer academic publishers, first ed., 2002.

[69] E. Desurvire, *Erbium-doped fiber amplifiers (Wiley series in telecommunications and signal processing).* John Wiley and Sons, Inc, second ed., 2002.

[70] M. Shimizu, M. Yamada, H. Horiguchi, T. Takeshita, and M. Okayasu, "Erbium-doped fibre amplifiers with an extremely high gain coefficient of 11.0 dB/mW," *Electronics Letters*, vol. 26, pp. 1641–1643, 1990.

[71] S. Bottacchi, *Noise and signal interference in optical fiber transmission systems: an optimum design approach.* Wiley, first ed., 2009.

[72] C. R. Giles and E. Desurvire, "Modeling erbium-doped fiber amplifiers," *Journal of Lightwave Technology*, vol. 9, pp. 271–283, 1991.

[73] H. Takara, J. Kanagawa, H. Masuda, K. Mori, K. Sato, Y. Inoue, T. Ohara, A. Mori, M. Kohtoku, Y. Miyamoto, T. Morioka, and S. Kawanishi, "Ultra-wideband tellurite/silica fiber Raman amplifier and supercontinuum lightwave source for 124-nm seamless bandwidth DWDM transmission," *Optical Fiber Communication Conference and Exhibit, 2002. OFC 2002.*

[74] J. D. Ania-Castañón, A. A. Pustovskikh, S. M. Kobtsev, and S. Turitsyn, "Simple design method for gain-flattened three-pump Raman amplifiers," *Optical and Quantum Electronics*, vol. 39, pp. 213–220, 2007.

[75] J. AuYeung and A. Yariv, "Spontaneous and stimulated Raman scattering in long low loss fibers," *IEEE Journal of Quantum Electronics*, vol. 14, pp. 347–352, 1978.

[76] S. Lewis, S. Chernikov, and J. Taylor, "Characterization of double Rayleigh scatter noise in Raman amplifiers," *IEEE Photonics Technology Letters*, vol. 12, p. 528.

[77] C. R. S. Fludger, V. Handerek, and R. J. Mears, "Pump to signal RIN transfer in Raman fiber amplifiers," *Journal of Lightwave Technology*, vol. 19, no. 8, pp. 1140–1148, 2001.

[78] K. Rottwitt, A. Stentz, T. Nielson, P. Hansen, K. Feder, and K. Walker, "Transparent 80km bi-directionally pumped distributed Raman amplifier with second order pumping," *Proceedings of Euro-*

pean Conference on Optical Communications (ECOC 99), no. II-144, 1999.

[79] J. D. Ania-Castañón, V. Karalekas, P. Harper, and S. K. Turitsyn, "Simultaneous spatial and spectral transparency in ultralong fiber lasers," *Physical Review Letters*, vol. 101, p. 123903, 2008.

[80] L. Barker, A. El-Taher, M. Alcon-Camas, J. D. Ania-Castañón, and P. Harper, "42.6Gb/s RZ-ASK transmission over 2500 km using quasi-lossless transmission spans," *Lasers and Electro-Optics 2009 and the European Quantum Electronics Conference. CLEO Europe - EQEC 2009*, p. 1, 2010.

[81] M. Alcon-Camas, A. E. El-Taher, H. Wang, P. Harper, V. Karalekas, J. Harrison, and J. D. Ania-Castañón, "Long-distance soliton transmission through ultralong fiber lasers," *Optics Letters*, vol. 34, pp. 3104–3106, 2009.

[82] A. E. El-Taher, J. D. Ania-Castañón, V. Karalekas, and P. Harper, "High efficiency supercontinuum generation using ultra-long Raman fiber cavities," *Optics Express*, vol. 17, pp. 17909–17915, 2009.

[83] V. Zakharov, V. Lvov, and G. Falkovich, *Kolmogorov spectra of turbulence: wave turbulence*. Springer, first ed., 1992.

[84] S. A. Babin, V. Karalekas, E. V. Podivilov, V. K. Mezentsev, P. Harper, J. D. Ania-Castañón, and S. K. Turitsyn, "Turbulent broadening of optical spectra in ultralong Raman fiber lasers," *Physical Review A*, vol. 77, p. 033803, 2008.

[85] S. K. Turitsyn, J. D. Ania-Castañón, S. A. Babin, V. Karalekas, P. Harper, D. V. Churkin, S. I. Kablukov, A. E. El-Taher, E. V. Po-

divilov, and V. K. Mezentsev, "270-km ultralong Raman fiber laser," *Physical Review Letters*, vol. 103, p. 133901, 2009.

[86] O. Frazao, C. Correia, J. L. Santos, and J. M. Baptista, "Raman fibre Bragg-grating laser sensor with cooperative Rayleigh scattering for strain-temperature measurement," *Measurement Science and Technology*, vol. 20, p. 045203, 2009.

[87] X.-H. Jia, Y.-J. Rao, F. Peng, Z.-N. Wang, W.-L. Zhang, H.-J. Wu, and Y. Jiang, "Random-lasing-based distributed fiber-optic amplification," *Optics Express*, vol. 21, p. 6572.

[88] S. A. Babin, A. E. El-Taher, P. Harper, E. V. Podivilov, D. V. Churkin, and S. K. Turitsyn, "Effect of Rayleigh-scattering distributed feedback in multi-wavelength and tunable Raman fibre lasers," *37th European Conference on Optical Communication and Exhibition, ECOC 2011*, p. 6065918, 2011.

[89] M. Krause, S. Cierullies, H. Renner, and E. Brinkmeyer, "Pump-to-stokes RIN transfer in Raman fiber lasers and its impact on the performance of co-pumped Raman amplifiers," *Optics Communications*, vol. 260, pp. 656–661, 2006.

[90] M. Alcon-Camas and J. D. Ania-Castañón, "RIN transfer in 2nd-order distributed amplification with ultralong fiber lasers," *Optics Express*, vol. 18, no. 23, pp. 23569–23575, 2010.

[91] M. Mermelstein, C. Headley, and J.-C. Bouteiller, "RIN transfer analysis in pump depletion regime for Raman fibre amplifiers," *Electronic Letters*, vol. 38, no. 9, pp. 403–405, 2002.

[92] B. Bristiel, S. Jiang, P. Gallion, and E. Pincemin, "New model of noise figure and RIN transfer in fiber Raman amplifiers," *IEEE Photonics Technology Letters*, vol. 18, no. 8, pp. 980–982, 2006.

[93] D. V. Churkin, S. A. Babin, A. E. El-Taher, P. Harper, S. I. Kablukov, V. Karalekas, J. D. Ania-Castañón, E. V. Podivilov, and S. K. Turitsyn, "Raman fiber lasers with a random distributed feedback based on Rayleigh scattering," *Physical Review A*, vol. 82, p. 033828, 2010.

[94] V. Karalekas, J. D. Ania-Castañón, P. Harper, S. A. Babin, E. V. Podivilov, and S. K. Turitsyn, "Impact of nonlinear spectral broadening in ultra-long Raman fibre lasers," *Optics Express*, vol. 15, pp. 16690–16695, 2007.

[95] V. Karalekas, J. D. Ania-Castañón, J. Pérez-González, X. Chen, L. Zhang, and P. Harper, "Performance optimization of ultra-long Raman laser cavities for quasi-lossless transmission links," *Optics Communications*, vol. 1, pp. 214–218, 2007.

[96] R. Hui and M. O'Sullivan, *Fiber optic measurement techniques*. Academic Press, first ed., 2008.

[97] B. E. A. Saleh and M. C. Teich, *Fundamentals of photonics*. John Wiley and Sons, Inc., first ed., 1991.

[98] T. Horiguchi and M. Tateda, "BOTDA-nondestructive measurement of single-mode optical fiber attenuation characteristics using Brillouin interaction: Theory," *Journal of Lightwave Technology*, vol. 7, pp. 1170–1176, 1989.

[99] T. Kurashima, T. Horiguchi, and M. Tateda, "Distributed-temperature sensing using stimulated Brillouin scattering in optical silica fibers," *Optics Letters*, vol. 15, pp. 1038–1040, 1990.

[100] F. Rodríguez-Barrios, S. Martín-López, A. Carrasco-Sanz, P. Corredera, J. D. Ania-Castañón, L. Thévenaz, and M. González-Herráez, "Distributed Brillouin fiber sensor assisted by first-order Raman amplification," *Journal of Lightwave Technology*, vol. 28, pp. 2162–2172, 2010.

[101] X. Angulo-Vinuesa, S. Martín-López, J. Nuño, P. Corredera, J. D. Ania-Castañón, L. Thévenaz, and M. González-Herráez, "Raman-assisted Brillouin distributed temperature sensor over 100 km featuring 2 m resolution and 1.2 °C uncertainty," *Journal of Lightwave Technology*, vol. 30, pp. 1170–1176, 2012.

[102] S. Yin, P. B. Ruffin, and F. T. Yu, *Fiber optic sensors*. CRC Press, second ed., 2008.

[103] L. R. Jaroszewicz, Z. Krajewski, and R. Świllo, "Application of fiber-optic Sagnac interferometer for detection of rotational seismic events," *Molecular and Quantum Acoustics*, vol. 22, pp. 133–144, 2001.

[104] L. R. Jaroszewicz, Z. Krajewski, S. Solarz, and R. Teisseyern, "Application of the fibre-optic Sagnac interferometer in the investigation of seismic rotational waves," *Measurement Science and Technology*, vol. 17, pp. 1186–1193, 2006.

[105] L. Jaroszewicz, Z. Krajewski, H. Kowalski, G. Mazur, P. Zinowko, and J. Kowalski, "Autonomous fibre-optic rotational seismograph: Design and application," *Acta Geophysica*, vol. 59, pp. 578–596, 2011.

[106] B. Culshaw, "The optical fibre Sagnac interferometer: an overview of its principles and applications," *Measurement Science and Technology*, vol. 17, pp. R1–R16, 2006.

[107] V. Perlin and H. Winful, "On trade-off between noise and nonlinearity in WDM systems with distributed Raman amplification," *Optical Fiber Communication Conference and Exhibit*, vol. 70, p. WB1, 2002.

[108] K. F. E. Desurvire, B. Y. Kim and H. J. Shaw, "Reentrant fiber Raman gyroscope," *Journal of Lightwave Technology*, vol. 6, pp. 481–491, 1988.

[109] Y. Z. Chin-Yi Liaw and Y.-L. Laml, "Characterization of an open-loop interferometric fiber-optic gyroscope with the Sagnac coil closed by an erbium-doped fiber amplifier," *Journal of Lightwave Technology*, vol. 16, pp. 2385–2392, 1998.

[110] Y. Z. Chin-Yi Liaw and Y.-L. Lam, "Theory of an amplified closed-Sagnac-loop interferometric fiber-optic gyroscope," *Journal of Quantum Electronics*, vol. 35, pp. 1777–1785, 1999.

[111] S. Schiller, "Feasibility of giant fiber-optic gyroscopes," *Physical Review A*, vol. 87, p. 033823, 2013.

[112] C. K. Kirkendall and A. Dandridge, "Overview of high performance fibre-optic sensing," *Journal of Physics D: Applied Physics*, vol. 37, pp. R197–R216, 2004.

[113] G. Sagnac, "L'éther lumineux démontré par l'eff et du vent relatif d'éther dans un interférométre en rotation uniforme," *Comptes Rendus*, vol. 157, pp. 708–710, 1913.

[114] G. Sagnac, "Sur la preuve de la réalité de l'éth er lumineux par l'expérience de l'interférographe tournant," *Comptes Rendus*, vol. 157, pp. 1410–1413, 1913.

[115] H. C. Lefèvre, "Fundamentals of the interferometric fiber-optic gyroscope," *Optical Review*, vol. 4, pp. A20–A27, 1997.

[116] K. Bohm and K. Petermann, "Signal processing schemes for the fiber-optic gyroscope," *Proceedings of the SPIE*, vol. 719, pp. 36–44, 1986.

[117] R. Urlich, "Polarization and birefringence effects," *Optical Fiber Rotation Sensing, ed W K Burns*, pp. 31–79, 1994.

[118] M. Armenise, C. Ciminelli, F. Dell'Olio, and V. Passaro, *Advances in gyroscope technologies*. Springer-Verlag Berling Heidelber, first ed., 2010.

[119] D. M. Shupe, "Thermally induced nonreciprocity in the fiber-optic interferometer," *Applied Optics*, vol. 19, pp. 654–655, 1980.

[120] N. J. Frigo, "Compensation of linear sources of non-reciprocity in Sagnac interferometers," *Fiber Optic Laser Sensors I, Proceeding of the SPIE*, vol. 412, pp. 268–271, 1983.

[121] A. H. Gnauck, G. Charlet, P. Tran, P. J. Winzer, C. R. Doerr, J. C. Centanni, E. C. Burrows, T. Kawanishi, T. Sakamoto, and K. Higuma, "25.6-Tb/s WDM transmission of polarization-multiplexed RZ-DQPSK signals," *Journal of Lightwave Technology*, vol. 26, pp. 79–84, 2008.

[122] V. V. Kozlov, J. Nuño, and S. Wabnitz, "Theory of lossless polarization attraction in telecommunication fibers," *Journal of the Optical Society of America B*, vol. 28, pp. 100–108, 2011.

[123] J. Fatome, S. Pitois, P. Morin, and G. Millot, "Observation of light-by-light polarization control and stabilization in optical fibre for telecommunication applications," *Optics Express*, vol. 18, pp. 15311–15317, 2010.

[124] A. Zadok, E. Zilka, A. Eyal, L. Thévenaz, and M. Tur, "Vector analysis of stimulated Brillouin scattering amplification in standard single-mode fibers," *Optics Express*, vol. 16, pp. 21692–21707, 2008.

[125] M. Martinelli, M. Cirigliano, M. Ferrario, L. Marazzi, and P. Martelli, "Observation of light-by-light polarization control and stabilization in optical fibre for telecommunication applications," *Optics Express*, vol. 17, pp. 947–955, 2009.

[126] R. H. Stolen and E. P. Ippen, "Raman gain in glass optical waveguides," *Applied Physics Letters*, vol. 22, pp. 276–278, 1973.

[127] Q. Lin and G. P. Agrawal, "Polarization mode dispersion induced fluctuations during Raman amplifications in optical fibers," *Optics Letters*, vol. 27, pp. 2194–2196, 2002.

[128] Q. Lin and G. P. Agrawal, "Vector theory of stimulated Raman scattering and its applications to fiber-based Raman amplifiers," *Journal of the Optical Society of America B*, vol. 20, pp. 1616–1631, 2003.

[129] S. V. Sergeyev, S. Y. Popov, and A. T. Friberg, "Modeling polarization-dependent gain in fiber Raman amplifiers with randomly varying birefringence," *Optics Communications*, vol. 262, pp. 114–119, 2006.

[130] A. Galtarossa, L. Palmieri, M. Santagiustina, and L. Ursini, "Polarized backward Raman amplification in randomly birefringent fibers," *Journal of Lightwave Technology*, vol. 24, pp. 4055–4063, 2006.

[131] L. Arnold, *Stochastic differential equations: theory and applications*. Wiley, first ed., 1974.

[132] V. V. Kozlov and S. Wabnitz, "Suppression of relative intensity noise in fiber-optic Raman polarizers," *IEEE Photonics Technology Letters*, vol. 23, pp. 1088–1090, 2011.

[133] S. V. Sergeyev, S. Y. Popov, and A. T. Friberg, "Spun fiber Raman amplifiers with reduced polarization impairments," *Optics Express*, vol. 16, pp. 14380–14389, 2008.

[134] S. V. Sergeyev and S. Y. Popov, "Two-section fiber optic Raman polarizer," *IEEE Journal of Quantum Electronics*, vol. 48, pp. 56–60, 2012.